



# **The impact of chloride homeostasis on the development of LSO and LOC neurons**

Von der Fakultät für Medizin und Gesundheitswissenschaften der

Carl von Ossietzky Universität Oldenburg

zur Erlangung des Grades und Titels einer

Doktorin der Naturwissenschaften

(Dr. rer. nat.)

angenommene Dissertation

von Frau Jin-Rong He

geboren am 15.12.1987 in China

Gutachter: Prof. Dr. Ivan Milenkovic

Weitere Gutachterin: Prof. Dr. Conny Kopp-Scheinflug

Tag der Disputation: 22.06.2026

## Table of Contents

Summary.....	1
Zusammenfassung .....	2
1 Introduction .....	2
1.1 Neuronal development .....	4
1.1.1 The role of depolarizing inhibition in neuronal development.....	4
1.2 Functional organization of LSO and LOC circuits .....	7
1.2.1 Development of LSO and LOC neurons .....	8
1.3 KCC2 and depolarizing inhibition – the LSO as a model system .....	9
1.4 The KCC2 <sup>AD/AD</sup> mouse model .....	12
1.4.1 Phospho-mimetic mutation enhances KCC2 transport activity.....	12
1.4.2 Enhanced KCC2 activity curtails the depolarizing phase .....	13
1.5 Hypothesis and aims .....	14
2 Material and methods .....	16
2.1 Animals.....	16
2.2 Acute brain slice preparation .....	16
2.3 Whole-cell patch-clamp recordings .....	16
2.3.1 Current clamp recording .....	17
2.3.2 Voltage clamp recording .....	17
2.4 Electroporation .....	18
2.5 Post-hoc morphological identification of LSO and LOC .....	18
2.6 Immunohistochemistry .....	19
2.7 Statistics .....	19
3 Results .....	20
3.1 Differentiation of LSO and LOC neurons.....	20
3.1.1 Morphology and intrinsic membrane properties.....	20
3.1.2 Synaptic kinetics .....	22
3.2 Effects of the curtailed depolarizing phase on LSO neurons .....	24
3.2.1 Intrinsic excitability or AP properties are unaffected .....	24
3.2.2 Synaptic properties of LSO neurons.....	28

3.3 Effects of enhanced KCC2 activity on LOC neurons.....	39
3.3.1 Intrinsic membrane properties of LOC neurons are preserved.....	39
3.3.2 Synaptic properties of LOC neurons.....	42
4 Discussion.....	48
4.1 Rationale for using the KCC2 <sup>AD/AD</sup> mouse model.....	48
4.2 Preserved intrinsic excitability versus altered synaptic properties .....	49
4.2.1 Intrinsic properties develop independently of depolarizing inhibition.....	49
4.2.2 Synaptic properties exhibit cell-type-specific alterations .....	50
4.2.3 Cell-type-specific engagement of pre- and postsynaptic mechanisms.....	52
4.3 Cellular mechanisms linking depolarizing inhibition to synapse maturation.....	53
4.3.1 Calcium signaling as a key regulatory process.....	53
4.3.2 NMDA receptor signaling .....	54
4.3.3 BDNF signaling.....	54
4.3.4 Cell-type-specific differences in calcium handling .....	55
4.4 Limitations and technical considerations.....	55
4.5 Future directions.....	57
4.6 Conclusion.....	58
5 Abbreviations .....	59
6 References.....	61
7 Supplementary information .....	78
8 Index of figures and tables.....	94
9 Acknowledgements.....	96

## Summary

Inhibitory neurotransmission is fundamental to sound localization in the auditory brainstem, where precise processing of temporal and intensity cues relies on fast, hyperpolarizing inhibition. During early postnatal development, however, GABA and glycine act as depolarizing neurotransmitters, providing excitatory drive that is thought to be essential for neuronal maturation. As development progresses, the activity of the  $K^+$ - $Cl^-$  cotransporter KCC2 lowers intracellular chloride, converting GABA/glycine responses from depolarizing to hyperpolarizing, a process known as the depolarization-to-hyperpolarization (D/H) shift. The precise timing of this transition determines the duration of the depolarizing window, yet whether and how the length of this window shapes the maturation of specific neuronal properties and synaptic circuit remains unknown.

The medial nucleus of the trapezoid body (MNTB) to lateral superior olive (LSO) pathway in the auditory brainstem provides a well-established model to address this question. Within this circuit, the LSO integrates ipsilateral excitatory input with contralateral glycinergic inhibition via the MNTB to encode interaural level differences for sound localization. Intermingled with LSO neurons, lateral olivocochlear (LOC) neurons receive less potent inhibitory inputs from the same source, but serve a fundamentally different function by modulating the sensitivity and dynamic range of auditory nerve fibers. Using  $KCC2^{AD/AD}$  mice, in which a phospho-mimetic mutation renders KCC2 constitutively active and thereby curtails the depolarizing phase, I investigated how a shortened period of depolarizing inhibition affects intrinsic membrane properties and inhibitory synaptic transmission in these two functionally distinct but anatomically intermingled neuronal populations.

In LSO neurons, the curtailed or abolished depolarizing window led to a reduction in inhibitory postsynaptic current amplitude, that was likely attributable to decreased glycine receptor abundance. Intrinsic membrane properties, short-term plasticity, and presynaptic release dynamics remained unchanged, pointing to a selective postsynaptic deficit in receptor expression or stabilization. In LOC neurons, by contrast, the frequency of miniature inhibitory postsynaptic currents was reduced, alongside transient changes in synaptic kinetics, while postsynaptic current amplitude and intrinsic properties were preserved. This pattern suggests that development of inhibition in LOC neurons does not depend on depolarizing inhibition to the same extent as LSO neurons.

Together, these findings demonstrate that the duration of the depolarizing window is critical for inhibitory synaptic strengthening and that its curtailment produces cell-specific consequences: reduced postsynaptic glycine receptor expression or impaired receptor clustering in LSO neurons, but primarily presynaptic alterations in LOC neurons. The dissociation between preserved intrinsic properties and altered synaptic development further indicates that these two aspects of neuronal maturation are governed by separable developmental programs. These results establish the  $KCC2^{AD/AD}$  model as a valuable tool for dissecting how depolarizing inhibition instructs inhibitory circuit assembly in the auditory brainstem.

## Zusammenfassung

Inhibitorische Neurotransmission spielt eine wichtige Rolle für die Schalllokalisation im auditorischen Hirnstamm, da die Verarbeitung von interauralen Zeit- und Intensitätsunterschieden von der zeitlichen Präzision und der Stärke der Inhibition abhängig ist. Während der frühen postnatalen Entwicklung wirken GABA und Glycin jedoch als depolarisierende Neurotransmitter und liefern einen exzitatorischen Antrieb, der für die neuronale Reifung als essenziell angesehen wird. Im Laufe der Entwicklung steigt die Aktivität des  $K^+$ - $Cl^-$ -Cotransporters KCC2 wodurch die intrazelluläre Chlorid Konzentration sinkt und wandelt die GABA/Glycin-Antworten von depolarisierend zu hyperpolarisierend um – ein Prozess, der als Depolarisation-Hyperpolarisation-(D/H) Shift bezeichnet wird. Das genaue Timing des D/H Shifts bestimmt die Dauer der depolarisierenden Wirkung, doch ist bislang wenig bekannt, wie diese frühe Depolarisation die Reifungsprozesse in neuronalen Schaltkreisen determiniert.

Der Signalweg vom medialen Kern des Trapezkörpers (MNTB) zum lateralen oberen Oliv (LSO) im auditorischen Hirnstamm bietet ein etabliertes Modell, um diese Frage zu adressieren. In diesem Schaltkreis integriert die LSO ipsilateralen exzitatorischen Input mit kontralateraler glyciniger Inhibition über den MNTB, um interaurale Intensitätsunterschiede für die Schalllokalisation zu kodieren. Inmitten der LSO-Neuronen befinden sich laterale olivocochleäre (LOC)-Neuronen, die weniger starke inhibitorische Eingänge aus dem MNTB erhalten, aber eine grundlegend andere Funktion erfüllen, indem sie die Empfindlichkeit und den Dynamikbereich der Hörnervenfasern modulieren. Unter Verwendung von  $KCC2^{AD/AD}$  Mäusen, bei denen eine phosphomimetische Mutation den KCC2 Transporter konstitutiv aktiviert, untersuchte ich, wie eine verkürzte Periode depolarisierender Inhibition die Entwicklung der intrinsischen Membraneigenschaften und der inhibitorischen synaptischen Transmission in diesen beiden funktionell unterschiedlichen, aber anatomisch vermischten neuronalen Populationen beeinflusst.

In den LSO-Neuronen führte die verkürzte oder aufgehobene frühe Depolarisation zu einer Reduktion der Amplitude inhibitorischer postsynaptischer Ströme, was wahrscheinlich auf eine verminderte Anzahl von Glyzinrezeptoren zurückzuführen ist. Intrinsische Membraneigenschaften, Kurzzeitplastizität und präsynaptische Freisetzungsdynamik blieben unverändert, was auf ein selektives postsynaptisches Defizit in der Rezeptorexpression oder Rezeptorclustering hindeutet. Bei LOC-Neuronen hingegen war die Frequenz der miniaturen inhibitorischen postsynaptischen Ströme (mIPSC) reduziert, begleitet von transienten Veränderungen der synaptischen Kinetik, während sich die Amplitude der postsynaptischen Ströme und die intrinsischen Eigenschaften normal entwickeln. Dieses Muster deutet darauf hin, dass die Reifung der inhibitorischen Eingängen an den LOC-Neuronen nicht in demselben Maße auf depolarisierende Inhibition angewiesen ist wie an den LSO-Neuronen.

### *Zusammenfassung*

Zusammengefasst, zeigen diese Ergebnisse, dass die Dauer der frühen GABA/Glycin Depolarization eine wichtige Rolle für die Entwicklung der Stärke der MNTB-LSO Inhibition spielt. Eine Verkürzung dieser depolarisierenden Wirkung verursacht eine verminderte Expression oder beeinträchtigte Stabilisierung von Glyzinrezeptoren in den LSO-Neuronen, aber vorwiegend präsynaptische Veränderungen in den LOC-Neuronen. Diese Ergebnisse zeigen zudem, dass die Entwicklung von intrinsischen Membraneigenschaften welche für Aktionspotentialaktivität entscheidend sind, unabhängig von der frühen Depolarization verläuft. Diese Ergebnisse etablieren das  $KCC2^{AD/AD}$ -Modell als wertvolles Werkzeug, um zu untersuchen, wie depolarisierende Inhibition die Reifung inhibitorischer Schaltkreise im auditorischen Hirnstamm steuert.

## 1 Introduction

### 1.1 Neuronal development

Neuronal development is a complex, tightly regulated process that generates neurons with distinct morphologies, functional properties and connectivity required for proper nervous system function. This process begins with neuronal migration from sites of origin to their final positions (Hatten, 1999; Rakic, 1972), followed by the initiation of neurite outgrowth (Bray, 1973; Dent et al., 2003). Subsequently, neurons undergo terminal differentiation and engage in target-specific synaptogenesis (Goodman & Shatz, 1993; Waites et al., 2005). Finally, neurons form precise connections with their target cells, establishing the functional circuits that underlie nervous system activity (Sanes & Yamagata, 2009).

#### 1.1.1 The role of depolarizing inhibition in neuronal development

A hallmark of early brain development is the transient period of depolarizing GABAergic and glycinergic transmission. Unlike their predominantly hyperpolarizing role in the adult brain, these neurotransmitters provide excitatory drive during embryogenesis and early postnatal development (Ben-Ari, 2002; Ben-Ari et al., 2007; Owens & Kriegstein, 2002). This polarity is dictated by the electrochemical gradient for chloride, which is tightly regulated by cation-chloride cotransporters (CCCs) (De Koninck, 2007). In immature neurons, high expression of the  $\text{Na}^+\text{-K}^+\text{-2Cl}^-$  cotransporter (NKCC1) and low expression or activity of the  $\text{K}^+\text{-Cl}^-$  cotransporter (KCC2) result in an elevated intracellular chloride concentration ( $[\text{Cl}^-]_i$ ). Consequently, activation of  $\text{GABA}_A$  or glycine receptors triggers chloride efflux, depolarizing the membrane (Chamma et al., 2012; Kahle et al., 2008; Payne et al., 2003). As development progresses, a transcriptional switch upregulates and activates KCC2, which efficiently extrudes chloride (Amadeo et al., 2018; Clayton et al., 1998; Rivera et al., 1999; Stein et al., 2004; Yamada et al., 2004). This lowers  $[\text{Cl}^-]_i$  and shifts the equilibrium potential for chloride ( $E_{\text{Cl}^-}$ ) negative to the resting membrane potential (RMP), thereby establishing the mature, hyperpolarizing inhibition, a process known as depolarization-hyperpolarization (D/H) shift (Ben-Ari et al., 2007; Chamma et al., 2012; Lee & Rajakumar, 2022; Rivera et al., 1999; Yamada et al., 2004) (**Figure 1.1**).

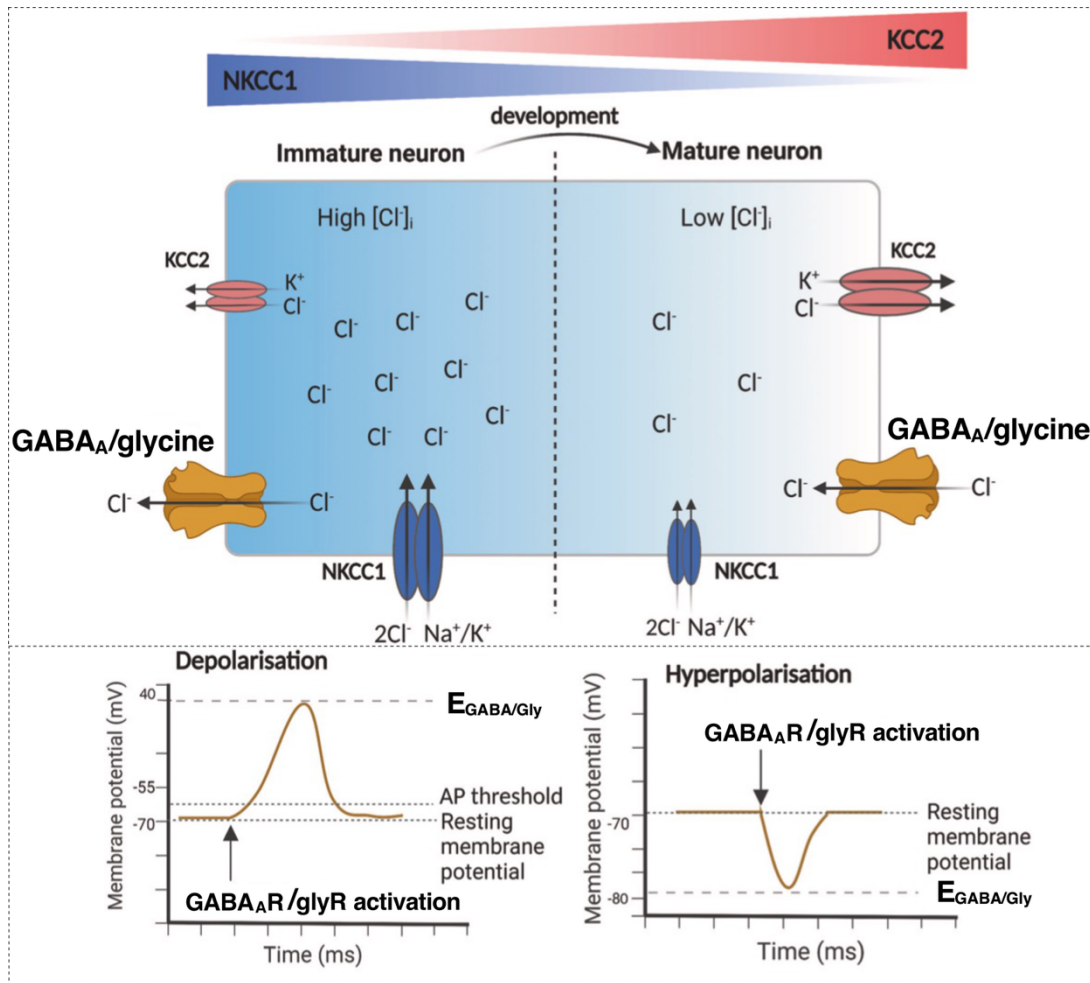


**Figure 1.1 Developmental shift in KCC2 and NKCC1 transport activities changes GABAergic/glycinergic signaling from depolarizing to hyperpolarizing.** Top: Schematic illustrating the shift in  $[Cl^-]_{in}$  driven by CCCs: Left: in immature neurons, high expression of the importer NKCC1 and low expression or activity of the extruder KCC2 maintain high  $[Cl^-]_{in}$ . Right: With maturation, KCC2 is upregulated and activated while NKCC1 is downregulated, leading to efficient chloride extrusion and low  $[Cl^-]_{in}$ . Bottom: Physiological consequences of chloride regulation: Left: In immature neurons, high  $[Cl^-]_{in}$  sets the equilibrium potential for GABA/glycine ( $E_{GABA/Gly}$ ) positive to RMP (here shown as  $-70$  mV). Consequently, receptor activation drives  $Cl^-$  efflux, resulting in membrane depolarization. Right: In mature neurons, low  $[Cl^-]_{in}$  shifts  $E_{GABA/Gly}$  negative to RMP, causing  $Cl^-$  influx and membrane hyperpolarization upon receptor activation. Diagram modified from (McMoneagle et al., 2024). ( $[Cl^-]_{in}$ : intracellular chloride concentration, NKCC1:  $Na^+-K^+-Cl^-$  cotransporter 1, KCC2:  $K^+-Cl^-$  cotransporter 2, GABA<sub>A</sub>R:  $\gamma$ -aminobutyric acid receptor type A, GlyR: glycine receptor,  $Na^+$ : sodium,  $K^+$ : Potassium; AP: action potential).

Notably, GABA/glycine signaling is established before glutamatergic transmission, serving as the

principal source of excitation during circuit assembly (Ben-Ari et al., 2007; Ben-Ari et al., 2012; Cherubini et al., 1991; Tyzio et al., 1999). This depolarizing inhibition plays a crucial role in neuronal development (Ben-Ari et al., 2007; Kullmann et al., 2002; Owens et al., 1996). By triggering sodium action potentials and activating voltage-gated calcium channels (VGCCs), depolarizing GABA drives intracellular calcium influx (Ben-Ari et al., 2007; Leinekugel et al., 1997). These calcium signals activate downstream cascades regulating gene expression, neurite outgrowth, and synaptic maturation (Ganguly et al., 2001). Furthermore, GABA/glycine-mediated depolarization relieves the voltage-dependent  $Mg^{2+}$  block of NMDA receptors, facilitating their activation even by weak glutamatergic inputs (Leinekugel et al., 1997). This synergistic interaction drives the generation of giant depolarizing potentials, the synchronized network oscillations essential for synaptic wiring (Ben-Ari et al., 1989; Khazipov et al., 1997). Together, these mechanisms provide an initial excitatory drive that engages immature networks without the risk of glutamate-induced excitotoxicity, helping to balance network activity during development (Sernagor et al., 2010).

This system operates as a self-limiting feedback loop. GABA/glycine-mediated calcium influx promotes KCC2 expression, thereby triggering the switch that terminates the excitatory phase (Ganguly et al., 2001). Thus, depolarizing GABA/glycine provides the necessary electrochemical signals to drive morphological differentiation, synchronize early network activity, and establish balanced excitatory-inhibitory networks.

The importance of precise timing for this developmental transition is underscored by pathological conditions. A delayed D/H shift, resulting in persistent depolarization, has been implicated in autism spectrum disorder, Down syndrome, and neuropathic pain (Coull et al., 2003; Kahle et al., 2008; Tyzio et al., 2014). Conversely, a premature D/H shift could curtail the depolarizing phase before activity-dependent developmental programs, such as dendritic refinement, synaptogenesis, and topographic map formation, have been completed, potentially yielding immature or improperly wired circuits. However, the precise causal role of depolarizing inhibition remains unclear, as most evidence is correlational and it is difficult to dissociate its functions from those of the subsequent hyperpolarizing phase. Investigating this requires a system in which inhibitory inputs are well defined and the developmental timeline is precisely characterized. These criteria are met by the inhibitory synapses formed by the principal neurons in the medial nucleus of the trapezoid body (MNTB) and their target neurons in the lateral superior olive (LSO), as a part of the sound localization circuit of the auditory brainstem.

## 1.2 Functional organization of LSO and LOC circuits

The lateral superior olive (LSO) comprises one of the major nuclei in the auditory brainstem. LSO principle neurons function as subtractive comparators for sound localization (Boudreau & Tsuchitani, 1968). They integrate excitatory input from spherical bushy cells (SBCs) in the ipsilateral anteroventral cochlear nucleus (AVCN) with inhibitory input from the contralateral side via the MNTB. The MNTB is driven by excitatory input from globular bushy cells (GBC) located in contralateral AVCN (Bledsoe et al., 1990; Cant & Casseday, 1986; Moore & Caspary, 1983; Smith et al., 1993; Sommer et al., 1993). When a sound source is ipsilateral, excitation overrides weak contralateral inhibition, driving high firing rates. Conversely, contralateral sound sources drive potent inhibition that suppresses the weaker excitation, leading to decreased firing (Grothe et al., 2010; Tollin et al., 2008). This computation creates a neural representation of auditory space along the azimuth, that is transmitted to the inferior colliculus (IC) for higher-order processing (Glendenning et al., 1992; Grothe et al., 2010). Beyond pure coding of interaural level differences (ILD), LSO neurons exhibit sensitivity to interaural time differences (ITDs) for transients and amplitude-modulated sounds, contributing to complex spatial representations (Franken et al., 2021; Joris & Yin, 1995).

Lateral olivocochlear (LOC) neurons are intermingled with principal LSO neurons and similarly receive ipsilateral excitation from T-stellate cells in the CN and contralateral inhibition from the MNTB (Hong et al., 2022; Sterenborg et al., 2010; Warr & Guinan, 1979). Functionally, however, they serve a fundamentally different role: LOC neurons project non-myelinated efferent fibers to the ipsilateral cochlea (Warr & Guinan, 1979), terminating on type I spiral ganglion neurons (SGN) beneath inner hair cells (Guinan, 2018; Liberman, 1980; Simmons, 2002). Through this efferent pathway, they modulate the sensitivity and dynamic range of auditory nerve fibers (Fuchs & Lauer, 2019). This modulation involves a complex cocktail of neurotransmitters and neuromodulators, including acetylcholine (ACh), GABA, dopamine, calcitonin gene-related peptide (CGRP), and enkephalin (Ciuman, 2010; Darrow et al., 2006; Doleviczenyi et al., 2008; Eybalin, 1993; Le Prell et al., 2014; Maison et al., 2013). While ACh mediates fast inhibition via  $\alpha 9\alpha 10$  nicotinic receptors (Elgoyhen et al., 2001; Katz et al., 2004), GABA and dopamine provide slower modulatory control (Goutman et al., 2005; Ruel et al., 2001; Wu et al., 2020). Despite this extensive anatomical and neurochemical characterization, the cellular mechanisms through which the LOC system modulates afferent activity, particularly *in vivo* under natural auditory conditions, remain incompletely understood (Arnold et al., 1998; Fuchs & Lauer, 2019; Nouvian et al., 2015). LOC dysfunction may impair cochlear gain control and noise tolerance, contributing to conditions such as hidden hearing loss and hyperacusis (Fuchs

& Lauer, 2019; Liberman et al., 2014). Understanding the developmental trajectory of LOC neurons is therefore essential for elucidating how these modulatory circuits are established.

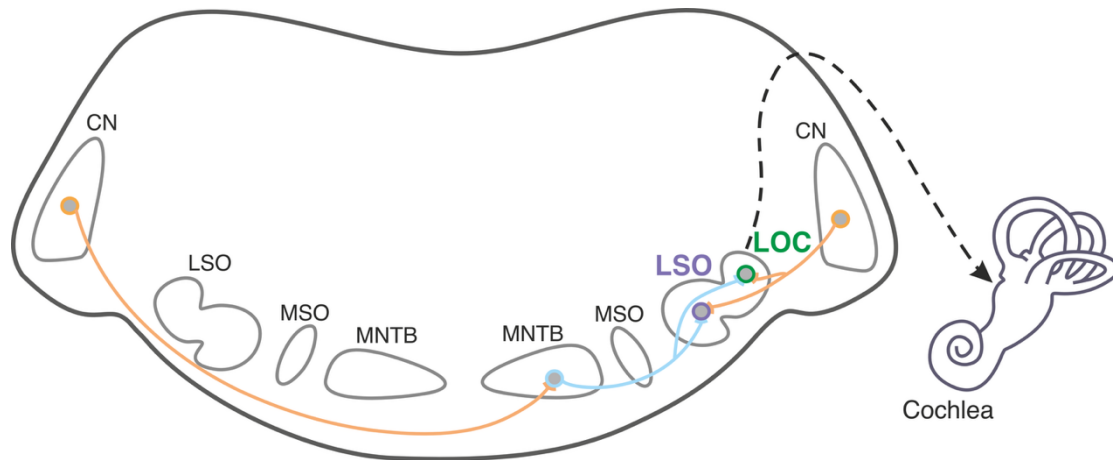


**Figure 1.2 Synaptic organization of LSO and LOC circuits.** Schematic illustrating the convergent inputs onto principal LSO neurons (purple) and LOC neurons (green). Both neuronal populations integrate excitatory inputs (orange) from the ipsilateral CN with inhibitory inputs (blue) from the MNTB, which is driven by the contralateral CN. LSO neurons serve a role in sound localization, whereas LOC neurons provide efferent feedback to the ipsilateral cochlea (dashed line). CN: cochlea nucleus; LSO: lateral superior olive; MSO: medial superior olive; MNTB: medial nucleus of the trapezoid body.

### 1.2.1 Development of LSO and LOC neurons

The development of the LSO/LOC systems requires the coordinated execution of genetic programs, trophic interactions, and activity-dependent refinement (Friauf & Lohmann, 1999 ; Kandler & Friauf, 1995; Simmons, 2002). These processes establish the topographic maps and neuronal connections essential for sound localization and efferent feedback control (Friauf et al., 2019).

In the LSO, immature neurons (during the first postnatal week) respond to both GABA and glycine with depolarization (Kotak et al., 1998; Nabekura et al., 2004). The high intracellular chloride concentration in the immature LSO appears to be maintained largely by the anion exchanger 3 (AE3), although this remains debate, in contrast to other brain regions where NKCC1 dominant (Balakrishnan et al., 2003; Becker et al., 2003; Kandler & Gillespie, 2005). During the first two postnatal weeks in altricial rodents, inhibitory receptors on LSO principal neurons undergo a developmental shift: GABAergic markers decrease while glycinergic transmission becomes dominant (Friauf & Lohmann, 1999 ; Kotak et al., 1998). This process coincides with the upregulation of KCC2, which renders glycine and GABA hyperpolarizing (Balakrishnan et al., 2003). This shift is

believed to be crucial for the LSO's mature computational role in encoding ILDs (Kandler & Gillespie, 2005; Kotak et al., 1998).

In contrast, the development of LOC neurons remains poorly characterized. Due to their scarcity and anatomical integration within the LSO, their specific developmental trajectory and chloride regulation remain poorly understood.

### **1.3 KCC2 and depolarizing inhibition – the LSO as a model system**

The role of KCC2 as the primary driver of the D/H shift has been established across multiple brain regions. KCC2 expression correlates with the onset of hyperpolarizing inhibition in the hippocampus, cortex and spinal cord (Ben-Ari et al., 2007; Blaesse et al., 2009; Kaila et al., 2014; Rivera et al., 1999). Conversely, pharmacological blockade or genetic ablation of KCC2 preserves the immature, depolarizing GABA responses in mature neurons or results in cell death (Ji et al., 2025; Kelley et al., 2018; Kontou et al., 2021).

In most forebrain regions, such as the hippocampus and neocortex, the D/H shift is driven by a progressive postnatal transcription of KCC2 combined with downregulation of the chloride-accumulating transporter NKCC1 (Ben-Ari et al., 2007; Blaesse et al., 2009; Kaila et al., 2014; Rivera et al., 1999). Within the auditory brainstem, however, the timing of D/H shift differ. The nuclei of the SOC exhibit a staggered timing of the D/H shift that spans nearly two weeks. While the superior paraolivary nucleus (SPN) transitions before birth, the LSO around P4-8, and the medial superior olive (MSO) around P5-9, many MNTB neurons remain depolarized by glycine throughout P10 (**Figure 1.3**) (Löhrke et al., 2005; Milenkovic & Rubsam, 2011). Notably, membrane-associated KCC2 immunoreactivity was already detectable in all SOC nuclei during this depolarizing period, indicating that the sole presence of KCC2 at the membrane does not confer functional chloride extrusion (Löhrke et al., 2005).

The LSO has become a key structure in studying this phenomenon. Unlike the hippocampus, where developmental upregulation at the mRNA and protein level parallels the D/H shift, KCC2 mRNA and protein are already abundantly present in the neonatal LSO during the depolarizing phase, with no substantial increase during maturation (Balakrishnan et al., 2003; Blaesse et al., 2006). Biochemical analysis revealed that this developmental activation correlates with a shift from monomeric to oligomeric (dimeric, trimeric, and tetrameric) KCC2 forms, a transition observed both in the brainstem

and throughout the brain (Blaesse et al., 2006). Translocation of KCC2 from membrane-raft to non-raft domains has been proposed as an additional posttranslational mechanism by which transport activity is conferred (Friauf et al., 2011; Hartmann et al., 2009). In the cochlear nucleus, the phosphorylation state of KCC2 differs between developing and adult tissue, with the phosphorylated form predominating at mature stages (Friauf et al., 2011; Vale et al., 2005). More recently, phosphorylation of KCC2 at serine 937 has been identified as a potent mechanism for enhancing transport activity in auditory brainstem neurons: a gain-of-function KCC2 Thr934Ala/Ser937Asp knock-in mouse model exhibited an earlier developmental onset of hyperpolarizing glycinergic responses and more negative chloride reversal potentials in mature neurons (Radulovic et al., 2023).

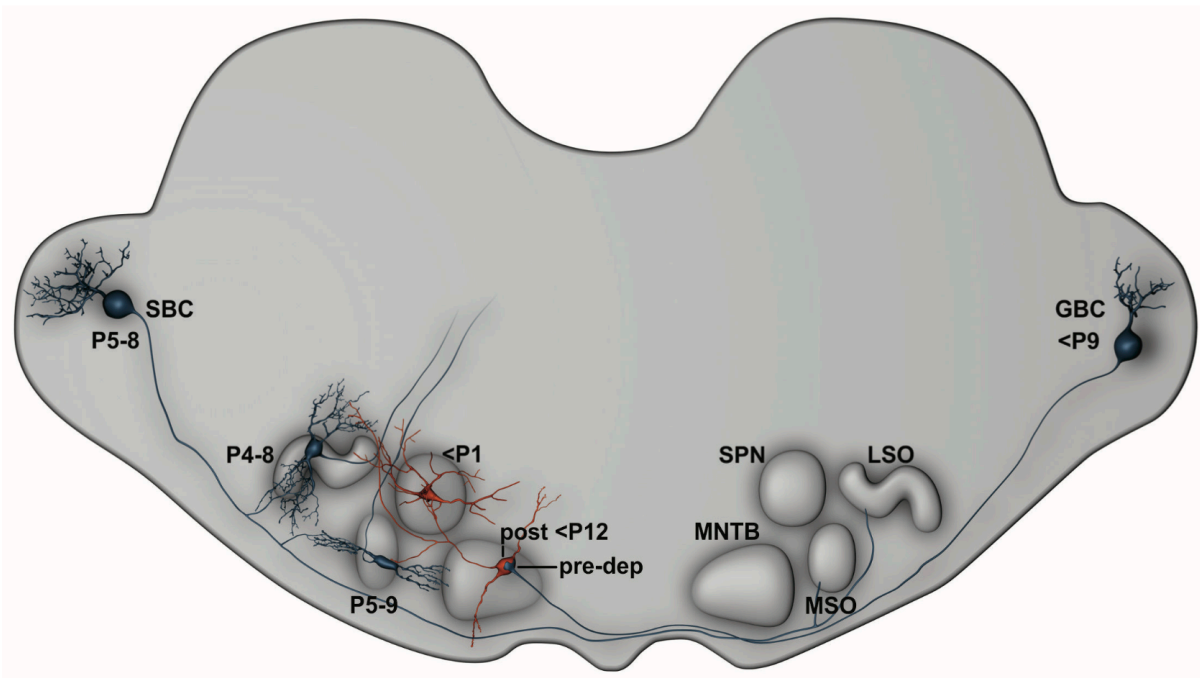


**Figure 1.3 Shift from depolarizing to hyperpolarizing actions of GABA and glycine in the auditory brainstem of mammals.** The image summarizes currently available experimental evidence, assessed with gramicidin perforated-patch recordings or with voltage-sensitive dye measurements. The  $\text{Cl}^-$  gradient undergoes a developmental shift with different time courses in distinct nuclei, but it is completed before hearing onset (<P12). The inhibitory neurons release glycine (MNTB) or GABA (SPN), while all other neurons shown here use glutamate as neurotransmitter. SBC: spherical bushy cell and GBC: globular bushy cell in the cochlear nucleus; LSO: lateral superior olive; MSO: medial superior olive; SPN: superior paraolivary nucleus; MNTB: medial nucleus of the trapezoid body (Milenkovic & Rubsamen, 2011).

Together, these findings establish the LSO as a system in which the D/H shift depends not on transcriptional upregulation of KCC2, as in the forebrain, but on a constellation of posttranslational mechanisms—oligomerization, raft-to-non-raft translocation, and phosphorylation—that activate a pre-existing pool of transporter protein. The D/H shift in the LSO also displays tonotopic heterogeneity: recordings with voltage-sensitive dye revealed large hyperpolarizing responses in high-frequency regions by P6, whereas low-frequency regions do not reach comparable amplitudes until P8 (Löhrke et al., 2005). Furthermore, its timing is subject to both experience and hormonal regulation (Rivera et al., 2004). Neonatal deafening via cochlear ablation prevents glycine-induced responses from becoming hyperpolarizing, with a significantly greater proportion of LSO neurons retaining elevated  $[Cl^-]_i$  ( $>15$  mM) at P14–16, indicating that afferent activity is required for normal maturation of chloride homeostasis (Friauf et al., 2011; Shibata et al., 2004).

The LSO represents a suitable model system to investigate the consequences of curtailing depolarizing inhibition for several reasons. First, its inputs are precisely defined and physically segregated: excitatory inputs terminate on dendrites, while inhibitory inputs terminate on the soma of the same LSO neuron (Boudreau & Tsuchitani, 1968; Glendenning et al., 1981; Tollin, 2003). Second, using gramicidin patch-clamp recordings during the critical developmental period, the extra- and intracellular environment can be tightly controlled to measure the  $E_{Cl^-}$  (Hirtz et al., 2012; Kullmann & Kandler, 2001). Third, the D/H shift occurs within a precisely defined temporal window (P4-8) and coincides with multiple well-characterized developmental changes.

During the depolarizing period, MNTB-LSO synapses co-release not only glycine and GABA (Nabekura et al., 2004) but also glutamate (Case & Gillespie, 2011; Cooper & Gillespie, 2011; Gillespie et al., 2005). While GABA dominates at P3–5 (~75% of the total inhibitory current), it gradually declines by hearing onset, making glycine the dominant transmitter (~90% at hearing onset) (Kotak et al., 1998). Importantly, glutamate co-release plays a specific role in the refinement of MNTB–LSO connections. Disruption of this co-release selectively impairs the refinement of inhibitory MNTB inputs while leaving the excitatory CN–LSO pathway unaffected. Consistent with this, CaV1.2 KO mice show impaired synaptic elimination and strengthening, resulting in broader MNTB input width, increased convergence, and weaker single-fiber strength (Hirtz et al., 2012).

This transient depolarizing inhibition coincides with the major period of activity-dependent circuit refinement (P4–8), during which the initially coarse tonotopic map is sharpened approximately 2-fold

(Clause et al., 2014; Hirtz et al., 2012; Kandler et al., 2009; Kim & Kandler, 2003). MNTB fiber convergence drops from 20–25 inputs per LSO neuron at P3 to only 3–10 by P11 (Hirtz et al., 2012; Kim & Kandler, 2003, 2010; Noh et al., 2010; Walcher et al., 2011), while maintained connections are strengthened 10–12-fold, primarily through increased quantal content and addition of release sites (Kim & Kandler, 2010). This strengthening is supported by a 3-fold increase in bouton number per MNTB fiber between P4 and P13 (Clause et al., 2014). Simultaneously, dendrites of LSO neurons undergo pruning (Rietzel & Friauf, 1998).

Together, the MNTB-LSO projection combines a clearly delineated D/H shift window with temporally overlapping transient features, including GABA/glycine/glutamate co-release, spontaneous activity-dependent refinement, neurotransmitter switching, and progressive biophysical specialization. This makes the LSO an appropriate model system for understanding how the early depolarizing period of GABAergic/glycinergic signaling contributes to the assembly and maturation of inhibitory circuits.

## 1.4 The KCC2<sup>AD/AD</sup> mouse model

### 1.4.1 Phospho-mimetic mutation enhances KCC2 transport activity

To investigate the impact of curtailing the depolarizing phase on neuronal development, I used the Thr934Ala/Ser937Asp (KCC2<sup>AD/AD</sup>) mouse line generated via CRISPR/Cas9-mediated genome editing. In this model, the Ser937Asp mutation mimics a constitutively phosphorylated state, while the adjacent Thr934Ala prevents regulation of the Thr934 site by locking it into a dephosphorylated form. This specific design isolates the effect of Ser937 phosphorylation by preventing confounding regulation by kinases or phosphatases at the Thr934 site. Thallium (Tl<sup>+</sup>) flux-based fluorescence assay quantitatively confirmed a two-fold enhanced transport activity of this KCC2 variant in a heterologous expression system (**Fig. 1.4**) (Radulovic et al., 2023). This model enables manipulation of chloride homeostasis without globally disrupting GABA/glycine signaling. By accelerating the transition from depolarizing to hyperpolarizing inhibition, it allows testing the necessity of the prolonged depolarizing phase for circuit formation and the dissection of the pre- and postsynaptic consequences of premature hyperpolarization.

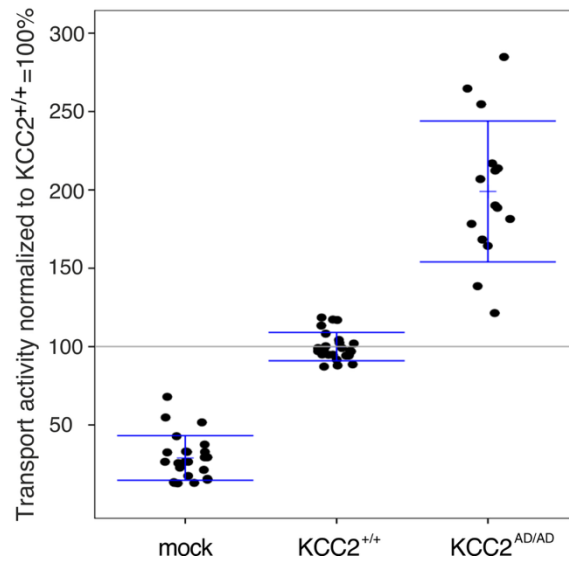


**Figure 1.4 Enhanced KCC2 transport activity in KCC2<sup>AD/AD</sup> mice.** HEK293 cells were transiently transfected with KCC2<sup>+/+</sup> or KCC2<sup>AD/AD</sup>. TI<sup>+</sup> flux measurement was performed to determine the KCC2 transport activity. KCC2<sup>+/+</sup> displayed a higher transport activity ( $100 \pm 1.8\%$ ,  $p = 1.93 \times 10^{-10}$ ) than mock transfected cells ( $24 \pm 2.9\%$ ). The transport activity of KCC2<sup>AD/AD</sup> ( $199 \pm 11.6\%$ ) is significantly enhanced ( $p = 0.001$ ). The graph represents the data of at least five independent measurements including three technical replicates per independent measurement, normalized to KCC2<sup>+/+</sup>. Depicted are mean values  $\pm$  SE (Radulovic et al., 2023).

### 1.4.2 Enhanced KCC2 activity curtails the depolarizing phase

To validate the physiological impact of this mutation, gramicidin perforated-patch clamp recordings were performed on neurons in the LSO during the critical developmental window (postnatal days P3 and P5). In wild-type control mice (KCC2<sup>+/+</sup>), the  $E_{Cl^-}$  followed the typical development shift from -36.6 mV at P3 to -63.8 mV at P5. In contrast, KCC2<sup>AD/AD</sup> mice exhibited a mature, hyperpolarized  $E_{Cl^-}$  of -79.4 mV as early as P3, with no further changes at P5. This demonstrates a hyperpolarizing chloride gradient already at P3, when GABA/glycine are normally depolarizing LSO neurons (Radulovic et al., 2023), while whether depolarizing inhibition persists before P3 remains unknown. In contrast, WT neurons remain depolarizing until the second postnatal week (Ehrlich et al., 1999). This mouse line uncouples the timing of the D/H shift from normal development, allowing me to compare WT and KCC2<sup>AD/AD</sup> mice during the critical window and reveal how chloride action instructs inhibitory circuit development in the LSO.

## Introduction

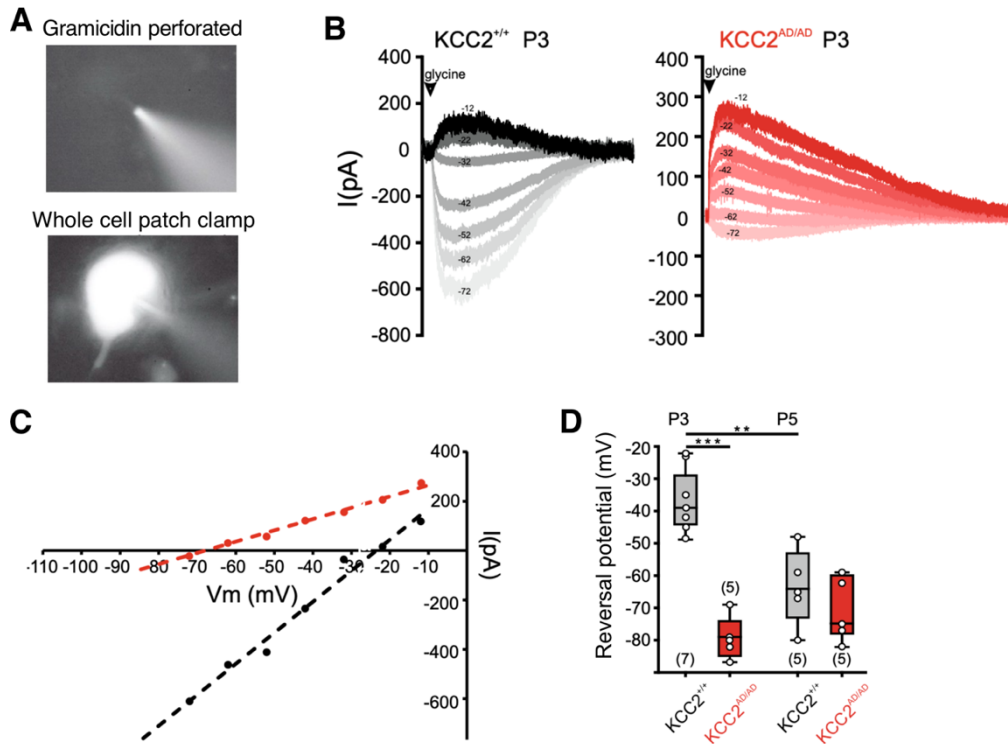


**Figure 1.5 Curtailed depolarizing phase in  $KCC2^{AD/AD}$  mice.** Gramicidin perforated recordings in LSO neurons. (A) (top) image of gramicidin perforated recording, visible patch pipette loaded with Atto 488; (bottom) whole-cell recording configuration with Atto 488 inside the cell following patch rupture. (B) Representative traces from recordings made in control ( $KCC2^{+/+}$ ) and homozygous  $KCC2$  Thr<sup>934</sup>Ala/Ser<sup>937</sup>Asp ( $KCC2^{AD/AD}$ ) mice at P3 showing current traces in response to glycine application at different holding potentials. (C) Representative plot of peak current amplitudes at different voltages for both groups at P3 (black  $KCC2^{+/+}$ , red  $KCC2^{AD/AD}$ ). Line intersection with x-axis indicates the  $E_{Gly^-}$ . (D) Population data from  $KCC2^{+/+}$  and  $KCC2^{AD/AD}$  at P3 and P5 showing significantly hyperpolarized  $E_{Gly^-}$  at P3 in  $KCC2^{AD/AD}$  compared to  $KCC2^{+/+}$ . The  $KCC2^{+/+}$  group shows a developmental change towards hyperpolarized values from P3 to P5 (Radulovic et al., 2023).

## 1.5 Hypothesis and aims

Based on the established role of depolarizing GABAergic and glycinergic signaling as critical trophic factor during early development, I hypothesize that the precise timing of the shift to hyperpolarizing inhibition is essential for the normal maturation of neuronal properties and synaptic circuitry in the auditory brainstem. Specifically, I propose that curtailing the depolarizing phase would disrupt both intrinsic membrane properties and the formation of inhibitory synaptic circuits in LSO and LOC neurons.

The primary aim of this thesis was to investigate how a curtailed or absent depolarizing inhibition influences the maturation of LSO and LOC neurons. Using the  $KCC2^{AD/AD}$  mouse line at two age groups (P14-shortly after hearing onset and P20-adult-like hearing), I addressed two specific objectives:

**1) Membrane properties**

I investigated how curtailing depolarizing inhibition during development affect intrinsic excitability. This included a detailed analysis of passive membrane properties, hyperpolarization-activated Cyclic Nucleotide-gated (HCN) channel function and action potential parameters defined by voltage-gated sodium and potassium channels.

**2) Synaptic properties**

I investigated how curtailing depolarizing inhibition during development affects the assembly of inhibitory synaptic circuits. This involved characterizing the miniature inhibitory postsynaptic currents (mIPSCs), evoked inhibitory postsynaptic currents (eIPSCs) and responses to local glycine application to dissect pre- and postsynaptic mechanisms.

Together, these experiments aimed to reveal how the timing of depolarizing inhibition contributes to the development cell properties and inhibitory synapses in two functionally distinct but anatomically intermingled neuronal populations.

## 2 Material and methods

### 2.1 Animals

This study used C57BL6/J, KCC2 wild-type (KCC2<sup>+/+</sup>) and KCC2 Thr934Ala/Ser937Asp (KCC2<sup>AD/AD</sup>) mice of both sexes (Radulovic et al., 2023). Experiments were performed at two developmental windows: postnatal day P13-15 and P20-25. All animals were bred at the University of Oldenburg animal facility, kept on a 12 h light/dark cycle with ad libitum access to food and water. All experimental protocols were approved and conducted in accordance with the German Animal Welfare Act (TSchG §4).

### 2.2 Acute brain slice preparation

Coronal slices (200 µm) containing LSO and MNTB were prepared using a vibratome (Leica VT1200 S) in ice cold, carbogenated (5% CO<sub>2</sub> and 95% O<sub>2</sub>) artificial cerebrospinal fluid (aCSF) maintained at pH 7.4. The composition of slicing solution varied with the experiment type. For current-clamp recordings, a low-calcium solution was used containing (in mM: 125 NaCl, 2.5 KCl, 0.1 CaCl<sub>2</sub>, 3 MgCl<sub>2</sub>, 1.25 NaH<sub>2</sub>PO<sub>4</sub>, 25 NaHCO<sub>3</sub>, 25 glucose, 3 myo-inositol, 2 sodium pyruvate, and 0.4 ascorbic acid), For voltage-clamp recordings a glucose-based solution was used containing (in mM): 260 glucose, 26 NaHCO<sub>3</sub>, 1.25 NaH<sub>2</sub>PO<sub>4</sub>, 3 myo-inositol, 2 sodium pyruvate, 6 MgCl<sub>2</sub>, 0.5 CaCl<sub>2</sub> (Weingarten et al., 2023) at at 37°C, pH 7.4. Slices were then transferred to an incubation chamber containing standard recording solution (same as slicing aCSF for current-clamp recordings, except CaCl<sub>2</sub> and MgCl<sub>2</sub> adjusted to 2 mM and 1mM, respectively) and allowed to recover for 1 hour at 37°C before being stored at room temperature until recording.

### 2.3 Whole-cell patch-clamp recordings

LSO and LOC neurons were visualized under an upright microscope (Axioskop 2 FS plus, Zeiss) equipped with a 63x water-immersion objective (W Plan-Apochromat 63x/1.0, Cat# 421480-9900-000, Zeiss) and an IR-CCD camera (IR-1000, DAGE-MTI). The recording chamber was continuously perfused with aCSF at a rate of ~1ml/min, with the temperature maintained at 35-37°C using a dual automatic temperature controller (TC-344B, Warner Instruments). Recording pipettes were pulled from borosilicate glass (GB-150F-8P, Science Products) to a resistance of 3–5 MΩ. For current-clamp recordings, pipettes were filled with an intracellular solution containing (in mM): 120 K-gluconate, 20 KCl, 1 NaCl, 0.05 CaCl<sub>2</sub>, 10 HEPES, 0.1 EGTA, 5 Na-Phosphocreatine, 2 Mg<sub>2</sub>-ATP, 0.3 Na<sub>2</sub>-GTP, 0.2% biocytin. For voltage-clamp recording a cesium-based solution was used

containing (in mM): 115.5 Cs-gluconate, 20 TEA-Cl, 10 HEPES, 5 Na<sub>2</sub>-phosphocreatine, 4 Mg-ATP, 0.3 Na<sub>2</sub>-GTP, 5 EGTA, 14.5 Cs-Cl, 6 QX314. Data were acquired using a Multiclamp 700B amplifier (Molecular Devices), digitized at a 100 kHz with a Digidata 1440A interface (Molecular Devices), and recorded using pClamp software (RRID:SCR\_011323, version 11.2.2, Molecular Devices). All reported voltages were corrected for a calculated liquid junction potential of -15 mV (current-clamp) or -14 mV (voltage-clamp). LSO and LOC neurons were distinguished *in situ* by soma size, morphology and responses to current injection.

### 2.3.1 Current clamp recording

To characterize membrane properties, current pulses (200 ms duration) were injected using two different protocols: course increments ranging from -400 to +1500 (100 pA steps) or fine increments ranging from -50 to +50 pA (5 pA steps). Rheobase was defined as the lowest current level required to trigger AP. AP parameters (threshold, latency, amplitude, half-width, maximum rising slope and maximum decaying slope) were measured at the rheobase. The membrane time constant ( $\tau$ ) was determined by fitting a mono-exponential function to the voltage response elicited by -10 pA pulse. Sag amplitudes were measured at current injection of -300 pA, and input resistance ( $R_{in}$ ) was calculated from the voltage response to fine-step current injections (-20 to +20pA) by using IV diagram and linear fit to the data points. Slope of the fit corresponds to the membrane  $R_{in}$ .

### 2.3.2 Voltage clamp recording

#### 2.3.2.1 Miniature inhibitory postsynaptic current (mIPSC) recording and analysis

To isolate mIPSC, the aCSF was supplemented with 6-Cyano-7-nitroquinoxaline-2,3-dione (CNQX, 10  $\mu$ M), D-2-amino-5-phosphonopentanoic acid (D-AP5, 50  $\mu$ M), and tetrodotoxin (TTX, 1  $\mu$ M) to block AMPA, NMDA glutamate receptors and voltage-gated sodium channels, respectively. Baseline mIPSC frequency was established by recording for at least one minute. A minimum of 300 events for LSO neurons and 50 events for LOC neurons were recorded per cell. Peak amplitude, rise time ( $\tau$  rise) and decay time ( $\tau$  decay) were analyzed in Clampfit, with kinetics determined by mono-exponential fitting.

#### 2.3.2.2 Evoked inhibitory postsynaptic current (eIPSC) recording

eIPSCs were evoked by single pulse or train stimuli delivered by a concentric electrode positioned medial to the LSO or within the MNTB. Excitatory transmission was blocked using CNQX (10  $\mu$ M)

and D-AP5 (50  $\mu$ M). The reversal potential was determined by holding the cell at potentials ranging from -74 to -14mV (10mV increments) during single pulse stimulation. To identify the inhibitory receptor contribution, strychnine (1  $\mu$ M, glycine receptors antagonist) and SR95531 (20  $\mu$ M, GABA<sub>A</sub> receptor antagonist) were bath-applied following baseline recordings.

### **2.3.2.3 Pressure-puff glycine application**

Glycine (0.35 mM in standard aCSF) was applied to the soma of LSO neurons via a Picospritzer (General Valve Corp.) Consistent stimulation was ensured by controlling pipette diameter (3  $\mu$ m), pressure (20 psi), duration (10 ms), and distance from the cell (10  $\mu$ m). Current responses were recorded at a holding potential of -74mV.

## **2.4 Electroporation**

For detailed morphological reconstruction, LSO and LOC neurons were electroporated in acute slices as previously described (Kanjhan & Bellingham, 2013). Pipettes (3–5 M $\Omega$ ) were filled with cesium-based intracellular solution supplemented with 1-2% Neurobiotin and Atto 590. Square-wave voltage pulses (200 mV, 0.5 s duration, 1 Hz) were applied for 2-3 min. Slices were left in the bath for an additional ~5-10 min to allow diffusion of Neurobiotin throughout the cell.

## **2.5 Post-hoc morphological identification of LSO and LOC**

Following electrophysiology, slices containing biocytin-filled neurons were fixed with 4% paraformaldehyde (PFA) in phosphate-buffered saline (PBS) overnight at 4°C. Slices were washed with PBS (6  $\times$  5 min) followed by PBS containing 0.3% TritonX-100 (PBST, 6  $\times$  5 min). To visualize biocytin, slices were incubated for 2.5 h at room temperature with Cy5-conjugated streptavidin (5  $\mu$ g/mL, Cat#016-170-084, Jackson ImmunoResearch) in PBST. This was followed by washes in PBST (6  $\times$  5 min), PBS (2  $\times$  5 min) and ultrapure water (2 $\times$ 5 min). All incubation and washing steps were performed on a tilting shaker in the dark. Slices were mounted on glass slides using Aqua-Poly/Mount mounting medium (Cat#18606, Polysciences, Inc.) and imaged using a Leica SP8 confocal scanning microscope using a 10x (0.3 NA, Cat#11506505) dry objective and a 63x (1.4 NA, Cat#11506350) oil-immersion objectives with 647 nm excitation wavelength.

## **2.6 Immunohistochemistry**

Mice (P14 and P20) were anesthetized with intraperitoneal injection of pentobarbital sodium (160mg/kg), followed by cardiac perfusion with saline and 4% PFA (pH 7.2–7.4). Brains were post-fixed overnight at 4°C and sectioned at 30 µm using a vibratome (Microm HM 650). For standard double immunofluorescence, slices were blocked with 5% normal goat serum (NGS) in PBST for 2 hours at room temperature. Slices were then incubated with chicken anti-Glyt2 (1:500; Cat#272006, Synaptic Systems) and mouse anti-gephyrin (1:500; Cat#147021, Synaptic Systems) in PBST with 3% NGS for 2 hours at 37°C, followed by overnight incubation at 4°C. After washing with PBST (3 × 5 min) and PBS (3 × 5 min), slices were incubated with secondary antibodies, Alexa Fluor 488 anti-chicken (1:500, Jackson Immuno Research, Cat#103-545-155,) and Cy5 anti-mouse (1:500, Jackson ImmunoResearch, Cat#115-175-146) for 2.5 h at room temperature.

For sections containing electroporated cells, a modified protocol was used. Sections were fixed and washed as described above, then blocked with 5% goat serum in PBST for 3 hours at room temperature. Slices were incubated with mouse anti-gephyrin (1:500, Synaptic Systems, Cat#147021) in PBST with 3% NGS overnight at room temperature. Secondary detection was performed using Alexa Fluor 488-conjugated streptavidin (5 µg/mL, Jackson ImmunoResearch, Cat#016-540-084) and Cy5 anti-mouse (1:500, Jackson ImmunoResearch, Cat#115-175-146) for 3 hours at room temperature. All slices were mounted and images as described in section 2.5.

## **2.7 Statistics**

Statistical analysis was performed using GraphPad Prism 10 (GraphPad Software). The quantitative cellular data presented is expressed as mean ± standard error of the mean (SEM). Sample size was not predetermined. Significance was assessed using an alpha level of 0.05. Comparison between groups based on gene/age were made using two-way ANOVA with Tukey's multiple comparisons post-hoc test.

## 3 Results

### 3.1 Differentiation of LSO and LOC neurons

#### 3.1.1 Morphology and intrinsic membrane properties

LOC neurons are distributed within and around the LSO, intermingled with principal LSO neurons (Maraslioglu-Sperber et al., 2024; Vetter & Mugnaini, 1992; Williams et al., 2022). These two populations can be distinguished by their distinct morphological and electrophysiological characteristics. LSO neurons exhibit low input resistance ( $R_{in}$ ), a prominent Ih-mediated sag potential and a short latency to the first AP at rheobase (Adam et al., 2001; Sterenborg et al., 2010). In contrast, LOC neurons are characterized by high  $R_{in}$ , the absence of Ih, and a delayed AP onset at rheobase (Adam et al., 1999; Maraslioglu-Sperber et al., 2024; Sterenborg et al., 2010). I used these electrophysiological criteria to segregate the two neuronal populations during current-clamp recordings (**Figure 3.1 A2, B2**). Morphologically, LSO principal neurons have large, fusiform or oval soma with oriented dendrites perpendicular to the tonotopic axis (rostro-caudally), whereas LOC neurons possess smaller, round or ovoid soma with dendrites that extend more locally and lack a clear tonotopic organization (Sanes, 1990; Williams et al., 2022). Post-hoc morphological analysis of biocytin-filled neurons further confirmed the identity of LSO (**Figure 3.1 A1**) and LOC (**Figure 3.1 B1**) neurons based on their characteristic cell morphology and dendritic orientation.

Population analysis revealed clear differences in intrinsic membrane properties between LSO and LOC neurons independent of genotype (as previously shown in (Maraslioglu-Sperber et al., 2024; Sterenborg et al., 2010)). The sag amplitude was significantly larger in LSO neurons compared to LOC at both age groups (P14:  $KCC2^{+/+}$   $p < 0.001$ ;  $KCC2^{AD/AD}$   $p < 0.001$ ; P20:  $KCC2^{+/+}$   $p = 0.005$ ;  $KCC2^{AD/AD}$   $p = 0.01$ ) (**Figure 3.1 C1**). These findings are consistent with the presence of strong Ih currents in LSO neurons and their absence in LOC neurons (Maraslioglu-Sperber et al., 2024; Sterenborg et al., 2010).

The  $R_{in}$  further distinguished the two neuronal populations. LOC neurons exhibited substantially higher  $R_{in}$  than LSO neurons at both ages (P14 and P20:  $p < 0.001$  for both genotypes) (**Figure 3.1 C2**). These findings are consistent with earlier reports (Maraslioglu-Sperber et al., 2024; Sterenborg et al., 2010).

## Results

Another parameter enabling differentiation was the AP latency at rheobase. LOC neurons displayed a markedly delayed spike onset compared with LSO neurons at both developmental stages (P14 and P20:  $p < 0.001$  for both genotypes). No developmental changes were detected in either neuronal population across genotypes ( $p > 0.99$ ) (**Figure 3.1 C3**). Based on these three parameters, LSO and LOC neurons visually segregate into two distinct populations (**Figure 3.1 D1-D3**).

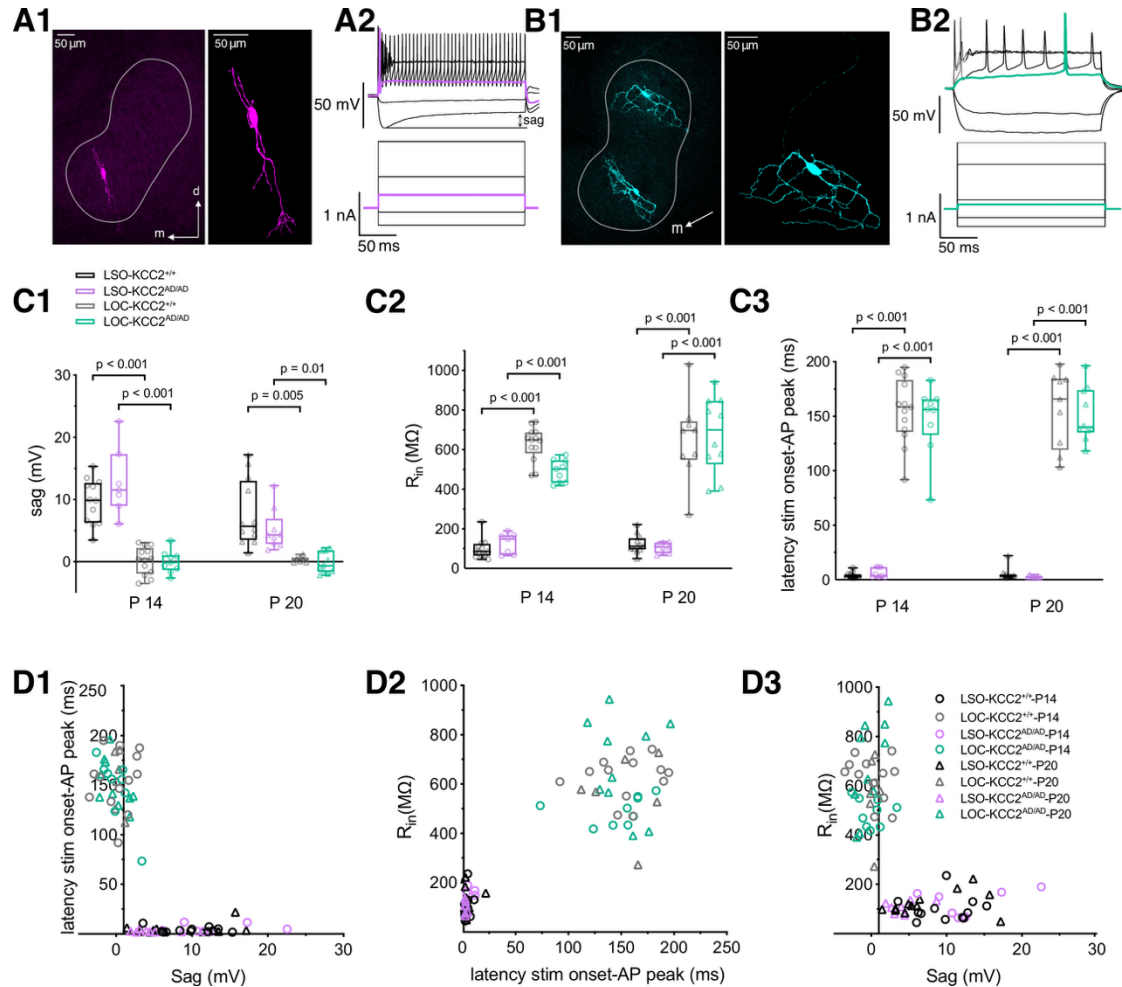


**Figure 3.1 Differentiation of LSO and LOC neurons according to morphology and intrinsic membrane properties.**

(**A1**) Confocal image of a biocytin-filled LSO neuron (magenta) Left: Low-magnification image showing the neuron's location within the LSO (white outline). Right: High-magnification image of the same cell displaying neuron's bipolar morphology. (**A2**) Representative voltage responses to current injections (stimulation protocol shown below), note the characteristic high-frequency firing in response to strong depolarizations and the prominent voltage sag in response to hyperpolarization. (**B1**) Confocal image of biocytin-labelled LOC neurons (cyan) located within the boundary of the LSO (white outline). Right: High-magnification image of the top cell, showing a disc-shaped soma and extensive dendrites. (**B2**) Representative voltage responses, exhibiting a characteristic AP delay at rheobase and the absence of voltage sag. (**C**) Comparison of intrinsic properties between LSO and LOC neurons in wildtype ( $KCC2^{+/+}$ , black, gray) and mutant ( $KCC2^{AD/AD}$ , purple, green) mice at P14 and P20. (**C1**) LSO neurons displayed significantly larger sag potentials compared

## Results

to LOC in response to -300 pA current injection at both ages. **(C2)**  $R_{in}$ , calculated from small steps (5pA) current injection and **(C3)** AP latency at rheobase were higher in LOC neurons. **(D1-D3)** Scatter plots illustrating the segregation of LSO (black, purple) and LOC (gray, green) neurons to distinct clusters based on the correlation between **(D1)** AP latency and sag potential, **(D2)**  $R_{in}$  and AP latency, and **(D3)**  $R_{in}$  and sag potential. Boxplots show median, interquartile range (IQR) and min/max values. Individual data points represent single neurons. 2-way ANOVA with Tukey's multiple comparison post-hoc tests.

Based on the classification parameters established under these experimental conditions, neurons in all subsequent experiments were categorized as either LSO or LOC.

### 3.1.2 Synaptic kinetics

Beyond intrinsic membrane properties, LSO and LOC neurons can also be distinguished by the kinetics of their synaptic currents. Although both neuronal populations receive inhibitory input from the MNTB, synaptic events in LOC neurons are substantially slower than those in LSO neurons (Haragopal et al., 2025; Sterenborg et al., 2010). Consistent with this, the rise time constant ( $\tau_{rise}$ ) of evoked inhibitory postsynaptic currents (eIPSCs) was slower in LOC neurons compared with LSO neurons at both developmental stages (P14:  $p < 0.001$ ; P20:  $p < 0.001$ ). Developmentally,  $\tau_{rise}$  became faster in LOC neurons ( $p < 0.001$ ), whereas no change occurred in LSO neurons ( $p = 0.97$ ) (**Figure 3.2 B**).

Similarly, the decay time constant ( $\tau_{decay}$ ) was longer in LOC neurons than in LSO neurons at both ages (P14:  $p < 0.001$ ; P20:  $p < 0.001$ ). During maturation, decay kinetics accelerated in LOC neurons ( $p < 0.001$ ), while remaining unchanged in LSO neurons ( $p = 0.93$ ) (**Figure 3.2 C**). These differences in synaptic kinetics likely reflect distinct receptor composition, synaptic architecture, or electrotonic filtering between the two cell types.

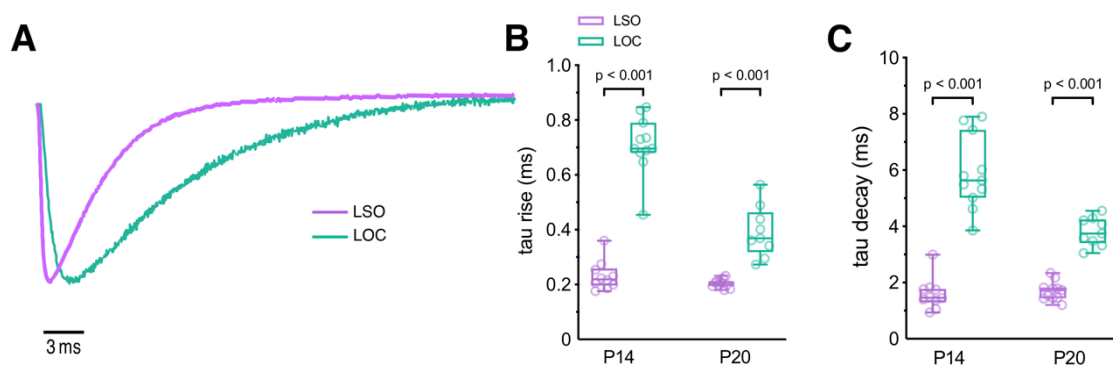


**Figure 3.2 Differentiation LSO and LOC neurons based on IPSC kinetics. (A)** Representative normalized traces of

### *Results*

IPSCs recorded from LSO (purple) and LOC (green) neurons. Note the slower kinetics of the LOC event. **(B and C)** Population data for IPSC tau rise and tau decay. LOC neurons exhibited slower rise time **(B)** longer decay **(C)**. Note the development speed-up of IPSC kinetics in LOC neurons (tau rise and tau decay:  $p < 0.001$ ) which was absent in LSO neurons (tau rise:  $p = 0.97$ , tau decay:  $p = 0.93$ ). Boxplots show median, IQR and min/max values. Individual data points represent single neurons. 2-way ANOVA with Tukey's multiple comparison post-hoc tests.

Together, the distinct intrinsic membrane properties and synaptic kinetics provide reliable physiological criteria for distinguishing LSO and LOC neurons. The presence of large  $I_h$  currents, low input resistance, and fast synaptic kinetics identifies LSO neurons specialized for rapid auditory processing. In contrast, LOC neurons exhibit high input resistance, delayed spike initiation, and slower inhibitory synaptic currents, consistent with their modulatory role within the olivocochlear system. The clear separation of these parameters further validates the electrophysiological classification used throughout this study to analyze the effects of the premature developmental chloride shift on these two neuronal populations.

## 3.2 Effects of the curtailed depolarizing phase on LSO neurons

### 3.2.1 Intrinsic excitability or AP properties are unaffected

To determine whether the curtailed depolarizing phase alters intrinsic membrane properties of LSO neurons, I first analyzed voltage responses to small-amplitude current steps (5 pA increments from -50 pA to 50 pA) to calculate membrane input resistance ( $R_{in}$ ).  $R_{in}$  is a key parameter of neuronal excitability, as it determines magnitude of membrane potential deflection in response to a given synaptic or injected current, thereby influencing the likelihood of reaching action potential threshold.  $R_{in}$  was similar between  $KCC2^{+/+}$  and  $KCC2^{AD/AD}$  at both P14 and P20 (P14:  $p = 0.57$ , P20:  $p = 0.74$ ), and no developmental change was observed in  $KCC2^{+/+}$  ( $p = 0.66$ ) or  $KCC2^{AD/AD}$  ( $p = 0.60$ ) (**Figure 3.3 A**).

Consistent with this, the membrane time constant ( $\tau$ ), a function of the cell's  $R_{in}$  and membrane capacitance ( $\tau = R_{in} \times C$ ), defining how fast a neuron's membrane potential responds to changes in input, remained unaltered across genotypes at either developmental stage (P14:  $p = 0.95$ , P20:  $p = 0.52$ ) and did not change between P14 and P20 in either genotype ( $KCC2^{+/+}$ :  $p = 0.76$ ,  $KCC2^{AD/AD}$ :  $p = 0.75$ ) (**Figure 3.3 B**). Together, these results indicate that the curtailed or abolished depolarizing phase does not disrupt the passive membrane properties of LSO neurons.

Given that GABA/glycine-mediated depolarization can facilitate neuronal excitation during early development (Ben-Ari et al., 1989; Leinekugel et al., 1997), precocious hyperpolarization might be expected to alter spike generation by reducing excitatory drive or triggering homeostatic compensation. So next I assessed neuronal excitability and active firing properties. The rheobase current was comparable between genotypes at both ages (P14:  $p = 0.73$ , P20:  $p = 0.27$ ). Consistent with the stable  $R_{in}$  and  $\tau$  values, rheobase did not change significantly between P14 and P20 ( $KCC2^{+/+}$ :  $p = 0.07$ ,  $KCC2^{AD/AD}$ :  $p = 0.93$ ) (**Figure 3.3 C**), suggesting that neuronal excitability is largely mature by P14. Furthermore, the first spike latency at rheobase was similar between genotypes (P14:  $p = 0.90$ , P20:  $p = 0.52$ ), and also unchanged across development ( $KCC2^{+/+}$ :  $p = 0.92$ ,  $KCC2^{AD/AD}$ :  $p = 0.51$ ) (**Figure 3.3 D**). These findings indicate that the mechanisms governing spike initiation remain unaffected by the curtailed or abolished depolarizing phase.

Finally, the voltage sag amplitude, reflecting activation of the hyperpolarization-activated current (I<sub>h</sub>), was comparable between genotypes at either age group (P14:  $p = 0.26$ , P20:  $p = 0.81$ ). However, LSO neurons of  $KCC2^{AD/AD}$  mice exhibited a developmental change in sag amplitude ( $KCC2^{+/+}$ :  $p =$

## Results

0.68,  $KCC2^{AD/AD}$ :  $p = 0.009$ ) (**Figure 3.3 E**). This suggests a delayed maturation of Ih in the mutant condition, possibly reflecting altered developmental regulation of HCN channel expression or activation. As the sag amplitude decreases to levels comparable with controls at later stages, this difference likely represents a transient developmental delay that is compensated during maturation.

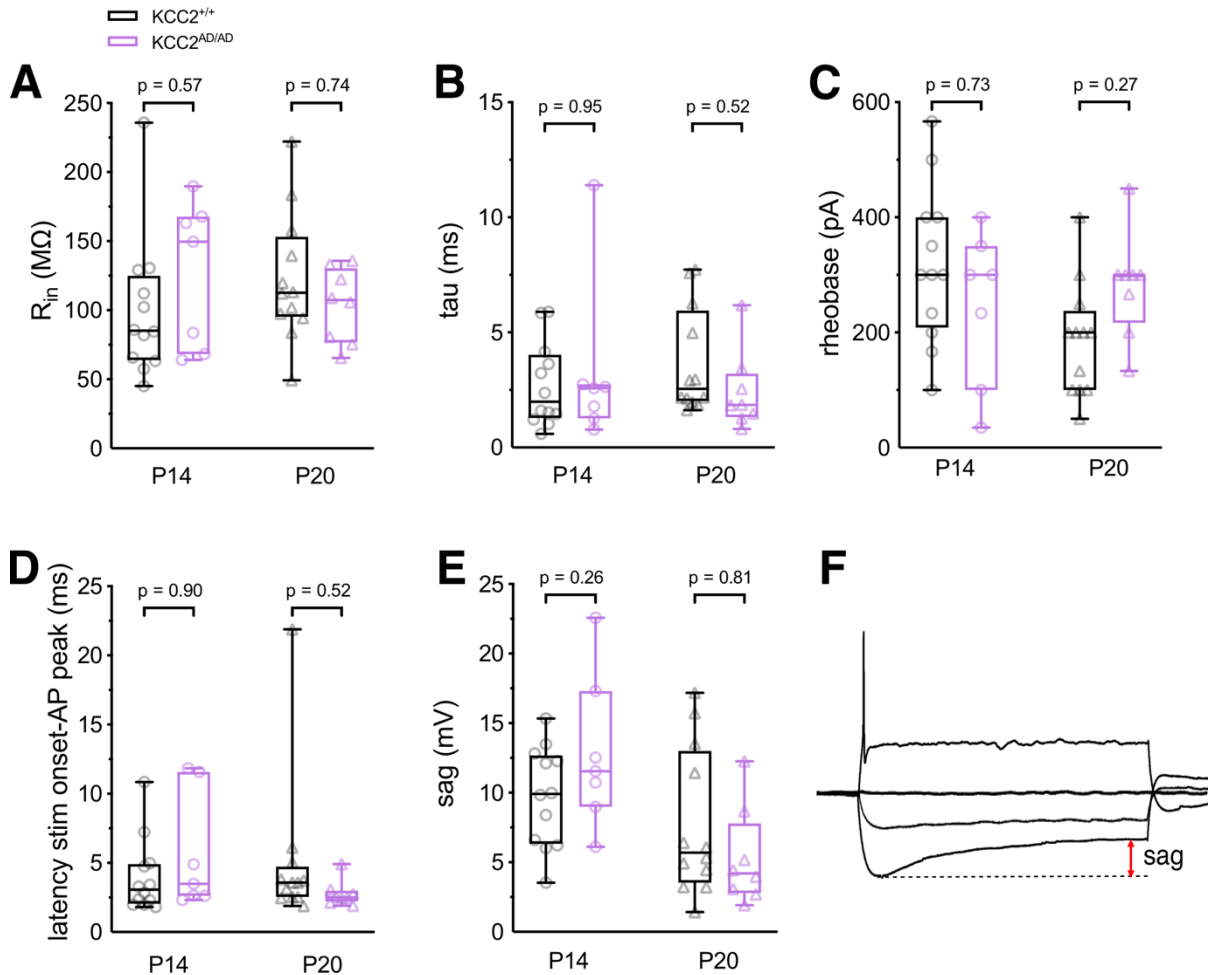


**Figure 3.3** Curtailed depolarizing phase does not impact intrinsic membrane properties of LSO neurons. (A-E)

Intrinsic electrophysiological parameters in neurons from wildtype ( $KCC2^{+/+}$ , black) and mutant ( $KCC2^{AD/AD}$ , purple) mice at P14 and P20. (A) Input resistance, (B) membrane time constant, (C) rheobase current (D) first AP latency at rheobase, (E) sag potential. (F) Representative current-clamp traces showing voltage responses to current steps. The red arrow indicates the measurement of the sag potential. Boxplots show median, IQR and min/max values. Individual data points represent single neurons. 2-way ANOVA with Tukey's multiple comparison post-hoc tests.

After establishing that the passive membrane properties were not affected by early maturation of chloride homeostasis, I next investigated firing properties by analyzing APs elicited at rheobase. AP threshold is dictated by the density and gating kinetics of voltage-gated sodium channels. Because

## Results

the manipulation eliminates the normal developmental window of depolarizing inhibition, network activity during a critical period may be altered, potentially triggering homeostatic plasticity that secondarily adjusts intrinsic excitability (Turrigiano, 2012). Thus, examining firing properties allowed me to determine whether loss of depolarizing inhibition leads to compensatory changes in active membrane properties. The voltage threshold for AP initiation was similar between  $KCC2^{+/+}$  and  $KCC2^{AD/AD}$  at both P14 and P20 (P14:  $p = 0.93$ , P20:  $p = 0.66$ ). In addition, no developmental changes were observed between P14 and P20 ( $KCC2^{+/+}$ :  $p = 0.31$ ,  $KCC2^{AD/AD}$ :  $p = 0.81$ ) (**Figure 3.4 B**), indicating that the maturation of AP threshold is already completed by P14.

The AP amplitudes, measured either from baseline or from threshold, were similar between genotypes and across developmental stages. Specifically, baseline to peak amplitude was comparable (P14:  $p = 0.95$ , P20:  $p > 0.99$ ), and with no developmental differences ( $KCC2^{+/+}$ :  $p = 0.13$ ,  $KCC2^{AD/AD}$ :  $p = 0.21$ ) (**Figure 3.4 C**). Likewise, threshold to peak amplitude did not differ between genotypes (P14:  $p = 0.95$ , P20:  $p > 0.99$ ) and remained stable across development ( $KCC2^{+/+}$ :  $p = 0.75$ ,  $KCC2^{AD/AD}$ :  $p = 0.50$ ) (**Figure 3.4 D**). These results indicate that the mechanisms underlying spike generation do not depend on depolarizing inhibition.

To further assess potential alterations in ion channel dynamics, I examined the kinetics of the AP waveform. The AP half-width measured as duration at the half of AP amplitude was indistinguishable between genotypes at both ages (P14:  $p > 0.99$ , P20:  $p > 0.99$ ) and did not change developmentally ( $KCC2^{+/+}$ :  $p = 0.76$ ,  $KCC2^{AD/AD}$ :  $p = 0.82$ ) (**Figure 3.4 E**). The maximum rising slope, reflecting sodium influx during depolarization, was comparable between genotypes (P14:  $p > 0.99$ , P20:  $p = 0.98$ ) and across developmental stages ( $KCC2^{+/+}$ :  $p = 0.76$ ;  $KCC2^{AD/AD}$ :  $p = 0.67$ ) (**Figure 3.4 F**). Similarly, the maximum decaying slope, driven primarily by outward potassium currents, was preserved in mutant mice (P14:  $p > 0.99$ , P20:  $p > 0.99$ ), and similar between P14 and P20 in  $KCC2^{+/+}$  ( $p > 0.99$ ) and  $KCC2^{AD/AD}$  ( $p > 0.99$ ) (**Figure 3.4 G**).

Finally, the amplitude of the afterhyperpolarization (AHP), which is primarily mediated by potassium efflux and contributes to the regulation of firing frequency and refractory period, was not different between genotypes (P14:  $p = 0.85$ , P20:  $p > 0.99$ ) and across developmental stages ( $KCC2^{+/+}$ :  $p > 0.99$ ,  $KCC2^{AD/AD}$ :  $p = 0.83$ ) (**Figure 3.4 H**).

Results

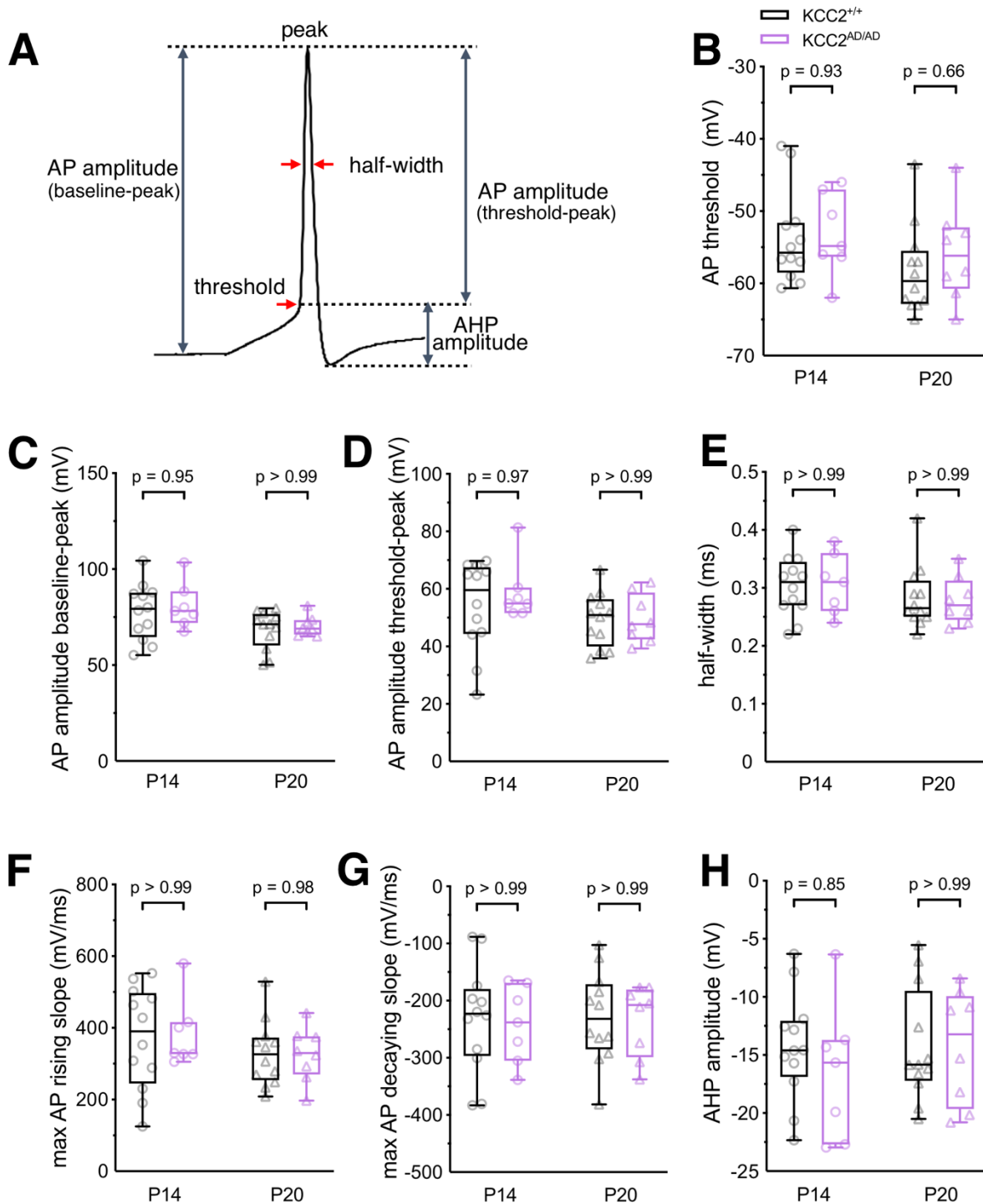


**Figure 3.4 Normal maturation of active neuronal properties despite the curtailed depolarizing phase. (A)** Single AP illustrating the quantification of waveform parameters: voltage threshold, peak amplitude, half-width, and afterhyperpolarization (AHP) amplitude. **(B-H)** Population analysis of AP properties in LSO neurons from wildtype ( $KCC2^{+/+}$ , black) and mutant ( $KCC2^{AD/AD}$ , purple) mice at P14 and P20. **(B)** AP threshold, **(C)** absolute AP amplitude (baseline to peak), **(D)** relative AP amplitude (threshold to peak), **(E)** AP half-width, **(F)** maximum rising slope, **(G)** maximum decaying slope, **(H)** AHP amplitude. Boxplots show median, IQR and min/max values. Individual data points represent single neurons. 2-way ANOVA with Tukey's multiple comparison post-hoc tests.

In summary, the comprehensive profiling of membrane properties ( $R_{in}$ ,  $\tau$ , rheobase, sag potential, and AP waveform parameters) demonstrates that the maturation of intrinsic electrophysiological properties of LSO neurons proceeds normally in  $KCC2^{AD/AD}$  mice. These findings indicate that curtailed or abolished depolarizing phase does not critically regulate the development of voltage-gated ion channels responsible for passive membrane properties and for AP generation.

### 3.2.2 Synaptic properties of LSO neurons

#### 3.2.2.1 Spontaneous release frequency is unaffected

During early postnatal development, the LSO circuit undergoes extensive structural and functional refinement. Initially, presynaptic MNTB axons and postsynaptic LSO dendrites exhibit broad branching, forming a coarse topographic map (Kandler & Friauf, 1993; Rietzel & Friauf, 1998; Sanes & Siverls, 1991; Sanes et al., 1992). Physiologically, this immature state is characterized by miniature inhibitory postsynaptic currents (mIPSC) with low frequency, small amplitudes, and slow decay kinetics (Nabekura et al., 2004). As development progresses, both MNTB terminals and LSO dendrites undergo significant pruning, to sharpen the tonotopic precision of the circuit (Clause et al., 2014; Kandler & Gillespie, 2005; Kim & Kandler, 2003; Sanes & Hafidi, 1996; Sanes et al., 1992; Sanes & Takacs, 1993). In LSO neurons, mIPSC amplitudes typically increase and decay kinetics accelerate (Nabekura et al., 2004; Walcher et al., 2011), consistent with maturation of inhibitory synaptic transmission. This developmental progression provides a relevant framework for comparison with P14 and P20 datasets, which correspond to stages of ongoing versus more advanced synaptic refinement, respectively.

Given that this period of synaptic refinement coincides with the shift in chloride homeostasis, I investigated whether the curtailed or abolished depolarizing phase in  $KCC2^{AD/AD}$  mice alters the maturation of spontaneous synaptic transmission. To address this, I recorded mIPSC in the presence of 1  $\mu$ M TTX to isolate spontaneous, AP-independent release events (**Figure 3.5 A, B**). Analysis of mIPSC frequency—reflects the number of inhibitory synapses (axonal boutons) contacting the recorded neuron and the probability of spontaneous vesicle fusion at those terminals—revealed no differences between  $KCC2^{+/+}$  and  $KCC2^{AD/AD}$  at either age group (P14:  $p = 0.24$ , P20:  $p = 0.49$ ), and no developmental change was observed between P14 and P20 ( $KCC2^{+/+}$ :  $p = 0.83$ ,  $KCC2^{AD/AD}$ :  $p = 0.99$ ) (**Figure 3.5 C**).

Results

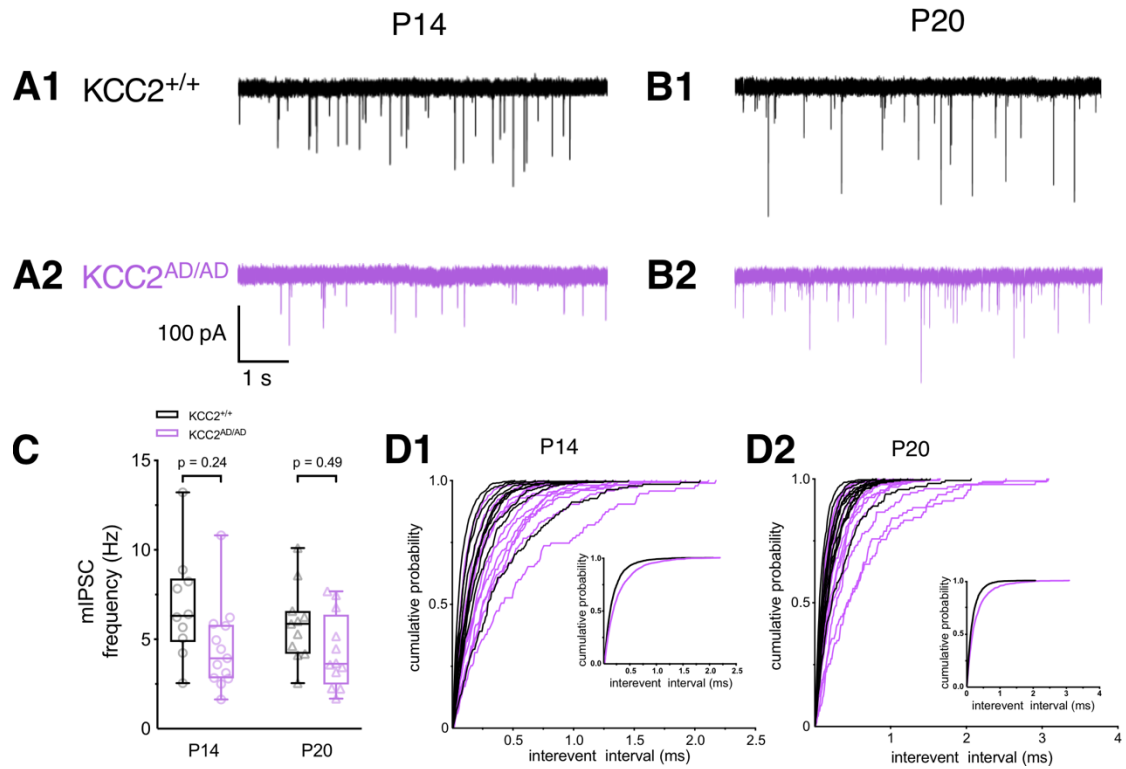


**Figure 3.5 Spontaneous release at the MNTB-LSO synapse is unaffected by curtailed depolarizing phase. (A, B)** Representative voltage-clamp recordings of mIPSCs isolated from LSO neurons in  $KCC2^{+/+}$  (black) and  $KCC2^{AD/AD}$  (purple) mice at P14 (A) and P20 (B). (C) Quantification of mean mIPSC frequency. (D) Cumulative probability distribution of interevent intervals (IEI) at P14 (D1) and P20 (D2). Main panels display distributions for individual cells (thin lines), while insets show the aggregated population mean. The temporal structure of spontaneous release remains intact in the  $KCC2^{AD/AD}$  group. Boxplots show median, IQR and min/max values. Individual data points represent single neurons. 2-way ANOVA with Tukey's multiple comparison post-hoc tests. Total events analyzed: P14:  $KCC2^{+/+}$  4132 events,  $KCC2^{AD/AD}$  3446 events; P20:  $KCC2^{+/+}$  3884 events,  $KCC2^{AD/AD}$  3010 events.

To further assess presynaptic release properties, I examined the temporal pattern of spontaneous events by analyzing the interevent interval (IEI). The cumulative probability distribution (CPD) of the IEIs showed no difference between genotypes (Figure 3.5 D). Together, these results indicate that the curtailed depolarizing phase does not affect the frequency or temporal distribution of spontaneous inhibitory events in LSO neurons, suggesting that AP-independent GABA/glycine presynaptic release remains intact, potentially reflecting similar spontaneous vesicular release probability and the number of functional inhibitory synaptic contacts.

### 3.2.2.2 mIPSC amplitude is developmentally reduced in $KCC2^{AD/AD}$ mice

In contrast, analysis of mIPSC amplitudes revealed a developmental deficit in the mutant condition. At P14, mean amplitudes were comparable between genotypes ( $p = 0.21$ ), although the CPD distribution suggested a subtle tendency towards smaller events in the mutant group. By P20, however, this deficit became more pronounced with smaller mIPSC amplitudes in  $KCC2^{AD/AD}$  ( $p < 0.001$ ). Consistent with this observation, the CPD at P20 showed a shift towards smaller quantal events in the mutant group. Moreover, the developmental increase in the quantal size observed in control neurons, was absent in  $KCC2^{AD/AD}$  mice (P14 vs P20:  $KCC2^{+/+}$ :  $p = 0.02$ ,  $KCC2^{AD/AD}$ :  $p = 0.87$ ) (**Figure 3.6**). These results indicate that although spontaneous release frequency remains unaffected, the strength of individual inhibitory synaptic events (quantal size) fails to mature normally in  $KCC2^{AD/AD}$  mice.

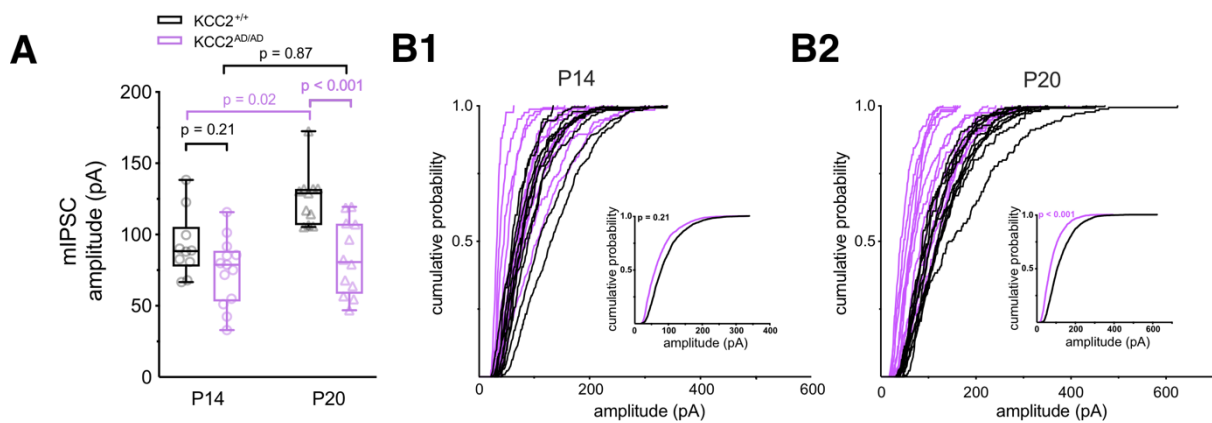


**Figure 3.6** mIPSC in LSO neurons show no developmental increase in amplitude in  $KCC2^{AD/AD}$  mice. **(A)**

Quantification of mean mIPSC amplitude in LSO neurons. While amplitudes were comparable between  $KCC2^{+/+}$  (black) and  $KCC2^{AD/AD}$  (purple) at P14, they were smaller in the later at P20. **(B)** Cumulative probability distributions of mIPSC amplitudes at P14 **(B1)** and P20 **(B2)**. Main panels display distributions for individual cells (thin lines), illustrating the variability within populations; insets show the aggregated population mean. Note the distinct leftward shift in the mutant group at P20, indicative of reduced quantal size. Boxplots show median, IQR and min/max values. Individual data points represent single neurons. 2-way ANOVA with Tukey's multiple comparison post-hoc tests. Total events analyzed: P14:  $KCC2^{+/+}$  2465 events,  $KCC2^{AD/AD}$  2100 events; P20:  $KCC2^{+/+}$  2701 events,  $KCC2^{AD/AD}$  2017 events.

### 3.2.2.3 mIPSC kinetics develop normally

To determine whether the reduced quantal size is associated with changes in channel kinetics or dendritic filtering, I next analyzed mIPSC kinetics. Neither the tau rise (reflects the activation kinetics of receptor opening and the electrotonic distance of the synapse) nor the tau decay (determined by

## Results

receptor gating kinetics and subunit composition—parameters that are sensitive to developmental changes such as the  $\alpha 2$ -to- $\alpha 1$  subunit switch) differed significantly between genotypes (tau rise: P14:  $p = 0.45$ , P20:  $p = 0.68$ ; tau decay: P14:  $p = 0.45$ , P20:  $p = 0.68$ ) (**Figure 3.7**). Furthermore, these parameters remained stable across development (tau rise:  $KCC2^{+/+}$ :  $p = 0.50$ ,  $KCC2^{AD/AD}$ :  $p = 0.22$ ; tau decay:  $KCC2^{+/+}$ :  $p > 0.99$ ,  $KCC2^{AD/AD}$ :  $p = 0.59$ ). The preservation of synaptic kinetics suggests that the receptor gating properties and synaptic filtering remain unchanged despite the reduction in current amplitude.

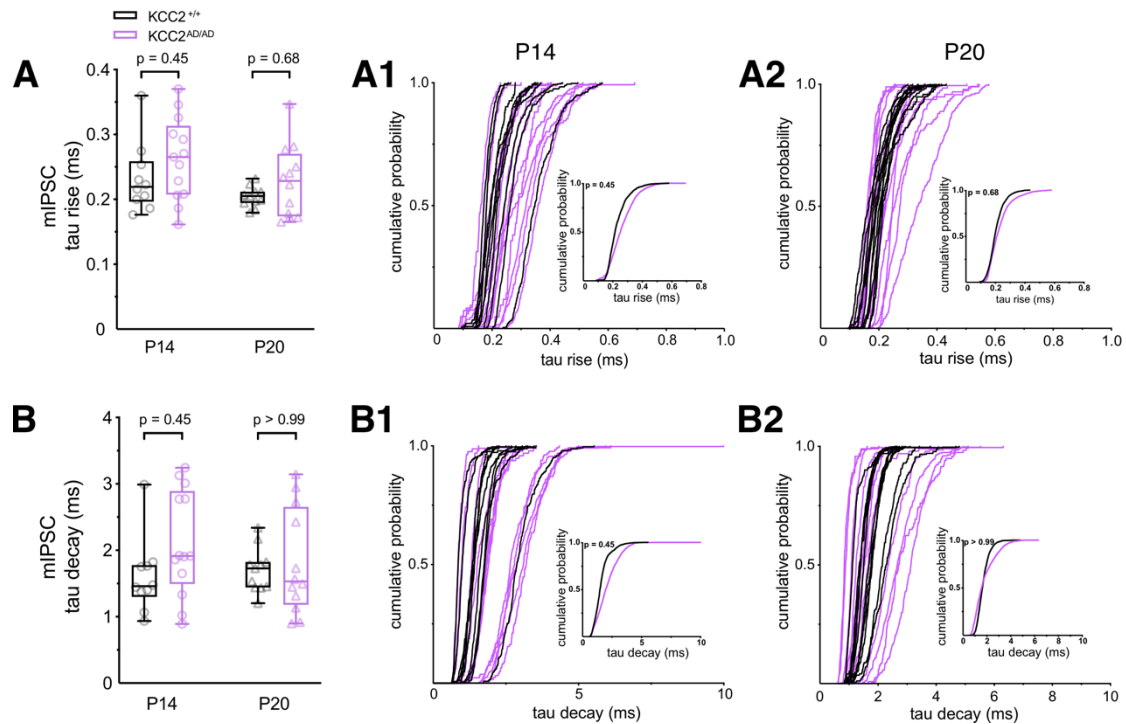


**Figure 3.7** Curtailed depolarizing phase does not affect the kinetics of mIPSC in LSO neurons. **(A, B)** Quantification of mIPSC kinetic parameters. **(A)** rise time constant (tau rise), **(B)** decay time constant (tau decay). Cumulative probability distribution (CPD) of tau rise **(A1, A2)** and tau decay **(B1, B2)** at P14 and P20. Main panels display data from individual cells (thin lines), while insets show the aggregated population mean. Boxplots show median, IQR and min/max values. Individual data points represent single neurons. 2-way ANOVA with Tukey's multiple comparison post-hoc tests.

Taken together, these findings indicate that the curtailed depolarizing inhibition selectively disrupts the maturation of inhibitory quantal size in LSO neurons without affecting the frequency or timing of spontaneous release. The reduced quantal amplitude observed at P20 could reflect a pre- or postsynaptic deficit. Presynaptically, smaller mIPSC amplitude could be caused by reduced vesicle size or less transmitter per vesicle. Postsynaptically, fewer glycine receptors at synaptic sites or differences in receptor clustering could result in smaller mIPSC amplitude.

### 3.2.2.4 Reduced eIPSC amplitude with preserved kinetics and short-term plasticity

To determine how the reduction in quantal size affects the synaptic strength, I recorded eIPSC by stimulating MNTB fibers projecting to the LSO. The currents were pharmacologically confirmed inhibitory by their sensitivity to strychnine and SR95531 (**Figure 3.11 A1 A2**). Consistent with the mIPSC data, maximal eIPSC amplitudes were significantly smaller in  $KCC2^{AD/AD}$  mice at both developmental stages (P14:  $p = 0.003$ , P20:  $p = 0.03$ ). Notably, the amplitudes were comparable between P14 and P20 within genotype ( $KCC2^{+/+}$ :  $p = 0.38$ ,  $KCC2^{AD/AD}$ :  $p = 0.10$ ), suggesting that the amplitude deficit persists throughout this developmental window in  $KCC2^{AD/AD}$  mice.

Similar to the mIPSC results, the kinetics of eIPSC were comparable between the genotypes. The tau rise did not differ at either age (P14:  $p > 0.99$ , P20  $p > 0.99$ ), and no developmental changes were detected ( $KCC2^{+/+}$ :  $p = 0.13$ ,  $KCC2^{AD/AD}$ :  $p = 0.24$ ). Likewise, tau decay was similar between genotypes (P14:  $p = 0.68$ , P20:  $p > 0.99$ ). Developmentally, the tau decay became faster in control neurons ( $p = 0.002$ ), whereas this acceleration was not significant in  $KCC2^{AD/AD}$  ( $p = 0.08$ ) (**Figure 3.8**). These results possibly indicate a delayed or incomplete  $\alpha 2$ -to- $\alpha 1$  subunit switch. Overall, these data suggest that the temporal properties of inhibitory synaptic currents remain largely preserved despite the reduction in amplitude.

To determine whether changes in presynaptic release probability contribute to the reduced eIPSC amplitudes, I next analyzed short-term plasticity (STP) during stimulus trains delivered at 10 Hz, 100 Hz, and 200 Hz. Both  $KCC2^{+/+}$  and  $KCC2^{AD/AD}$  neurons exhibited characteristic short-term depression (STD) at P14 (**Figure 3.9**) and P20 (**Figure S.1**), consistent with previous reports for this synapse (Brill et al., 2019; Kramer et al., 2014). Although the absolute current amplitudes were consistently smaller in the  $KCC2^{AD/AD}$  neurons across stimulation frequencies, the relative short-term depression profiles were similar between genotypes. The preservation of STD dynamics indicate that synaptic vesicle (SV) release probability and vesicle replenishment mechanisms are largely intact.

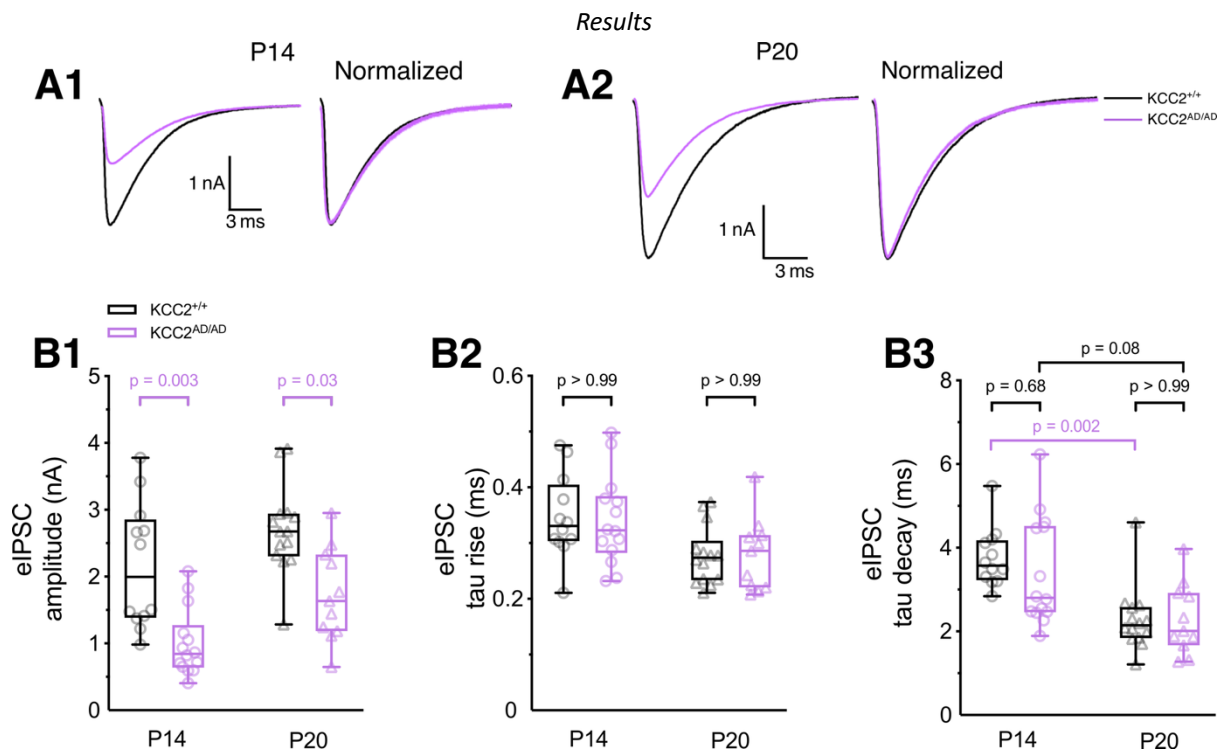


**Figure 3.8** Curtailed depolarizing phase reduces the eIPSC amplitudes in LSO neurons. **(A)** Representative eIPSC recorded from LSO neurons upon MNTB stimulation at P14 (**A1**) and P20 (**A2**). Left: Superimposed traces from KCC2<sup>+/+</sup> (black) and KCC2<sup>AD/AD</sup> (purple), illustrating the reduction in peak amplitude in the KCC2<sup>AD/AD</sup> group. Right: Peak-scaled normalized traces demonstrating identical waveform kinetics between genotypes. **(B)** Quantification of eIPSC properties. **(B1)** eIPSC amplitude is reduced in KCC2<sup>AD/AD</sup> mice, whereas rise time **(B2)** and decay time **(B3)** are indistinguishable between phenotypes. Boxplots show median, IQR and min/max values. Individual data points represent single neurons. 2-way ANOVA with Tukey's multiple comparison post-hoc tests.

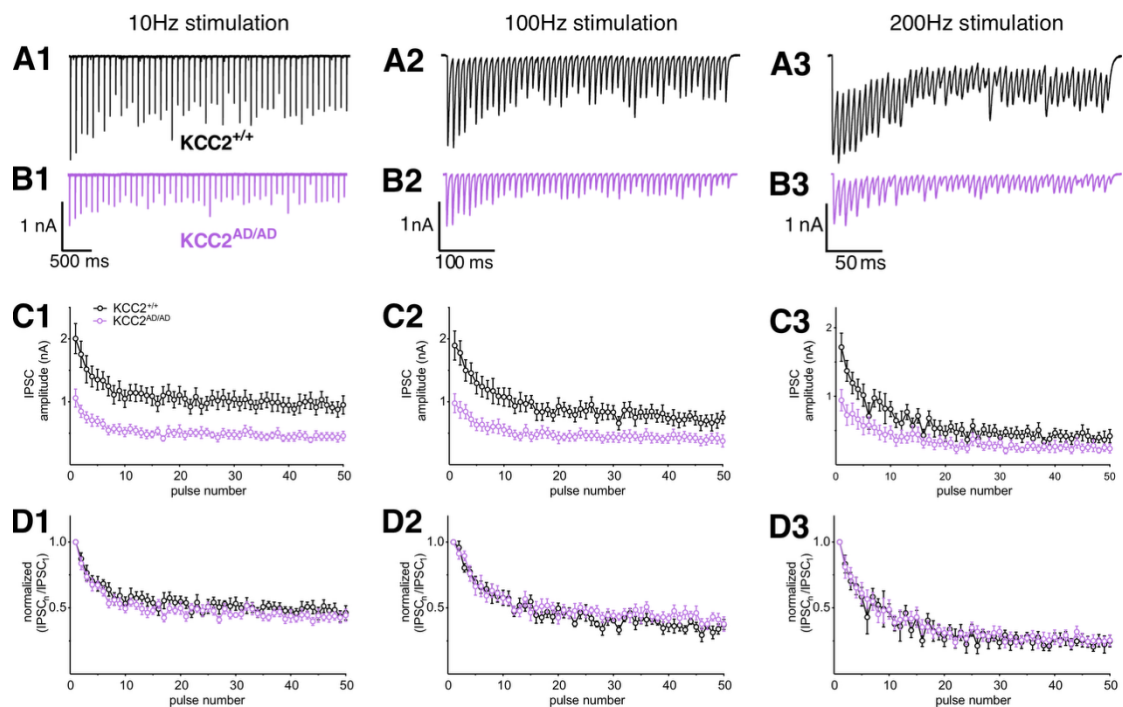


**Figure 3.9 Normal short-term plasticity in LSO neurons of KCC2<sup>AD/AD</sup> mice at P14.** (A, B) Representative eIPSC trains from KCC2<sup>+/+</sup> (A, black) and KCC2<sup>AD/AD</sup> (B, purple) neurons in response to 50 stimuli delivered at 10 Hz (left), 100Hz (middle) and 200Hz (right). (C) Quantification of eIPSC peak amplitudes plotted against pulse number for 10 Hz (C1), 100 Hz (C2), and 200 Hz (C3) stimulation. The current amplitude is lower in KCC2<sup>AD/AD</sup> group across tested frequencies. (D) Normalized synaptic depression profile (IPSC<sub>n</sub>/IPSC<sub>1</sub>) for the frequencies shown in C. The degree of depression and steady-state levels are indistinguishable between genotypes at 10 Hz (D1), 100 Hz (D2), and 200 Hz (D3). Error bar in C and D show SEM.

Taken together, the reduction in both quantal size and evoked inhibitory currents in the absence of major changes in kinetics or short-term plasticity strongly suggests a postsynaptic origin of the synaptic deficit. A potential candidate is a reduction of functional glycine receptors or changes in receptor clustering at the postsynaptic density. Another possible cause could be a smaller chloride driving force in KCC2<sup>AD/AD</sup> mice.

### 3.2.2.5 Reduced IPSC amplitude is not explained by altered chloride driving force

Given the elevated Cl<sup>-</sup>-extrusion capacity by the mutation mimicking KCC2-phosphorylation (Radulovic et al., 2023), I further tested whether the reduced IPSC amplitude could result from a change in electrochemical driving force. Specifically, a shift in intracellular chloride concentration could alter the chloride reversal potential ( $E_{Cl^-}$ ), thereby affecting the current amplitudes at a given holding potential. To investigate this, I determined  $E_{Cl^-}$  by recording eIPSCs at varying membrane potentials (-74 mV to -14 mV). After correcting for the liquid junction potential,  $E_{Cl^-}$  values were comparable between KCC2<sup>+/+</sup> and KCC2<sup>AD/AD</sup> neurons at both P14 and P20 (P14:  $p = 0.15$ , P20:  $p = 0.75$ ) (Figure 3.10). These values closely match the theoretical Nernst potential calculated for the recording solutions used (-36 mV). The similar  $E_{Cl^-}$  values are consistent with previous observations that Cs<sup>+</sup>-based internal solutions interfere with the Cl<sup>-</sup>-extruding capacity of KCC2 (Kakazu et al., 1999; Kakazu et al., 2000; Price & Trussell, 2006). Consequently, these measurements indicate that the reduced IPSC amplitudes observed in KCC2<sup>AD/AD</sup> neurons cannot be explained by a decreased chloride driving force under the recording conditions. While a developmental change in  $E_{Cl^-}$  was detected between P14 and P20 in KCC2<sup>AD/AD</sup> (P14 =  $-42.69 \pm 1.6$ , P20 =  $-34.62 \pm 2.93$ ,  $p = 0.04$ ), no change was observed in control neurons (P14 =  $-36.53 \pm 1.68$ , P20 =  $-30.55 \pm 1.6$ ,  $p = 0.29$ ) (Figure 3.10). This likely reflects residual Cl<sup>-</sup> extrusion by the constitutively active KCC2<sup>AD/AD</sup> despite Cs<sup>+</sup> interference, especially at P14. In principle, increased KCC2 activity would be expected to lower intracellular chloride concentration, thereby shifting the chloride equilibrium potential.

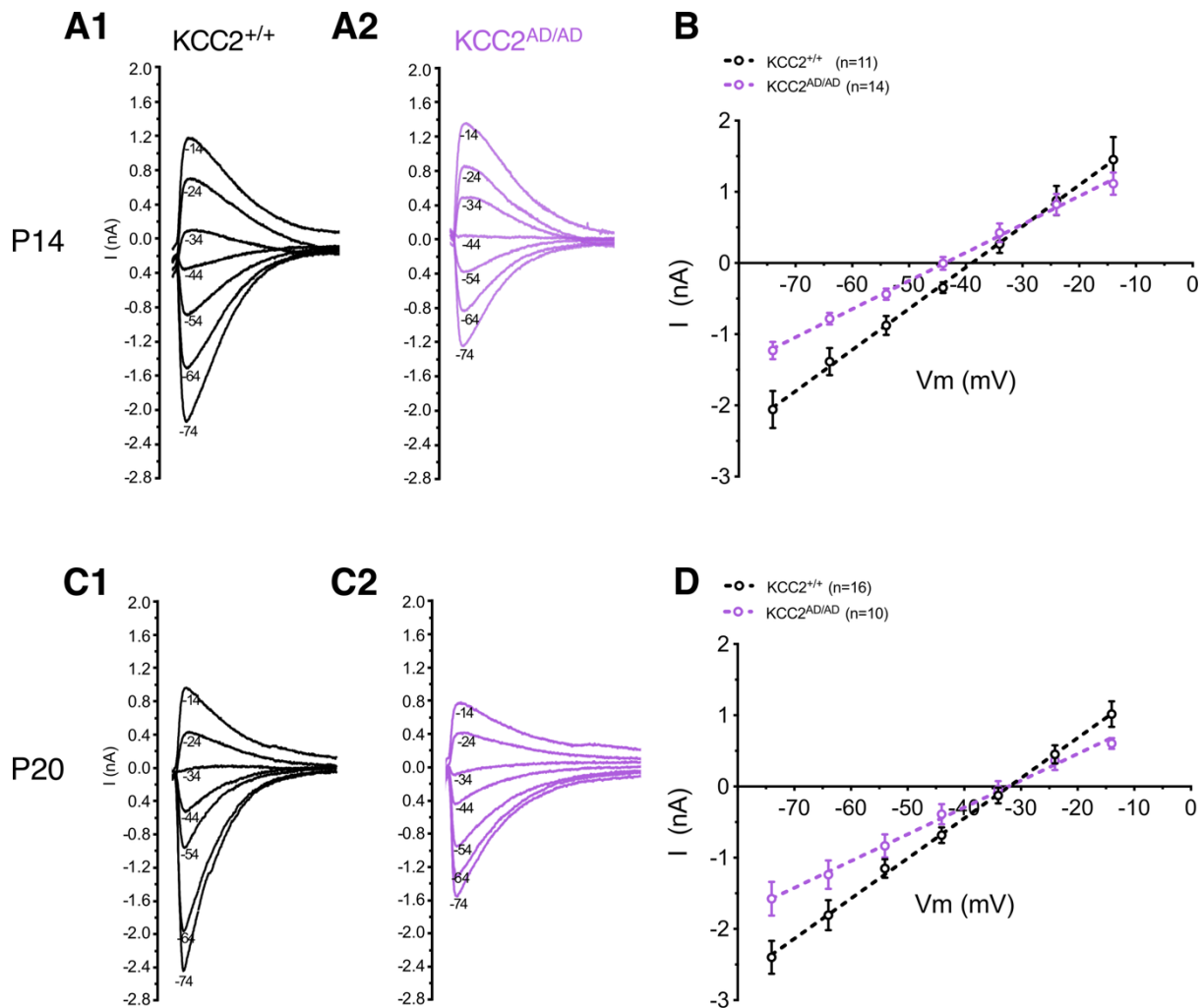


**Figure 3.10 No major differences in  $E_{IPSC}$  across genotypes.** (A, C) Representative eIPSCs recorded from LSO neurons at varying holding potentials (indicated in mV next to traces) for KCC2<sup>+/+</sup> (black) and KCC2<sup>AD/AD</sup> (purple) mice at P14 (A) and P20 (C). Note that while the absolute current amplitudes are smaller in the KCC2<sup>AD/AD</sup> group, the reversal potential is similar (B, D), current-voltage (I-V) relationship for eIPSCs recorded at P14 (B) and P20 (D). The intersection with the x-axis represents  $E_{IPSC}$ . Error bar in C and D show SEM.

### 3.2.2.6 Glycine receptor availability is reduced at postsynaptic sites

Having excluded presynaptic release deficits and alterations in driving force, I next tested the hypothesis that the reduced synaptic strength is caused by a deficit in postsynaptic receptor availability. First, I confirmed the pharmacological identity of inhibitory currents. In both genotypes and age groups, application of glycine receptor antagonist strychnine (1  $\mu$ M) reduced eIPSCs

### Results

amplitude by > 95% of the eIPSC (P14: KCC2<sup>+/+</sup> 97.1 ± 0.95%, n = 6, KCC2<sup>AD/AD</sup> 97.66 ± 1.19%, n = 6; P20: KCC2<sup>+/+</sup> 97.68 ± 1.21%, n = 6, KCC2<sup>AD/AD</sup> 95.82 ± 1.47%, n = 6) (**Figure 3.11 A B**), and the remaining component was completely abolished by GABA<sub>A</sub> receptor antagonist SR95531 (20 μM) (**Figure 3.11 A1, A2**). These results confirm that inhibitory transmission in LSO neurons at P14 and P20 is predominantly glycinergic in both KCC<sup>+/+</sup> and KCC2<sup>AD/AD</sup> mice.

To directly assess the functional availability of postsynaptic glycine receptors independent of presynaptic function, I applied glycine (0.35 mM) directly to the soma via pressure application. The concentration was optimized in preliminary trials to maximize the response amplitude while minimizing voltage errors associated with space-clamp limitations (**Figure 3.11 E**). Similar to synaptic stimulation experiments, pressure-application evoked currents were significantly smaller in KCC2<sup>AD/AD</sup> neurons compared to controls at both developmental stages (P14: p < 0.001, P20: p = 0.004). Developmentally, glycine-evoked currents increase between P14 and P20, although this increase reached significance only in KCC2<sup>AD/AD</sup> neurons (KCC2<sup>+/+</sup>: p = 0.06, KCC2<sup>AD/AD</sup>: p = 0.007) (**Figure 3.11 C1 C2 and D**). Together, these results indicate that the depolarizing inhibition is required for functional development of postsynaptic glycine receptors in LSO neurons. Because glycine was applied directly to the soma, these findings suggest a postsynaptic mechanism independent of presynaptic release. Therefore, the smaller glycine-evoked currents are potentially caused by a reduced number of functional glycine receptors or decreased receptor clustering at postsynaptic sites.

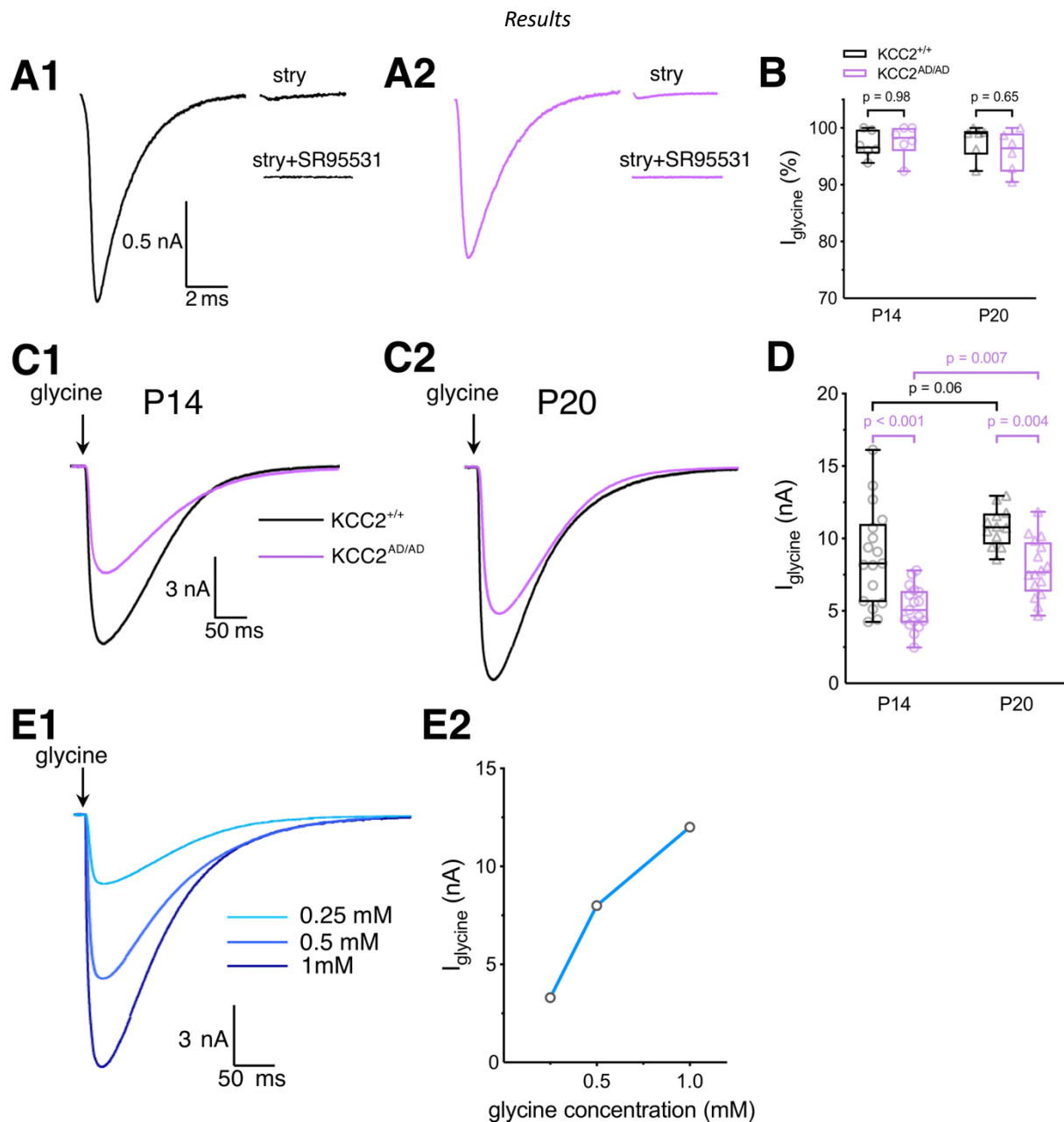


**Figure 3.11 GlyR-mediated currents are reduced in LSO neurons of  $KCC2^{AD/AD}$  mice.** (A, B) Pharmacological characterization of inhibitory inputs. (A) Representative eIPSC recorded from  $KCC2^{+/+}$  (A1) and  $KCC2^{AD/AD}$  (A2) at P14. The current is almost entirely abolished by the glycine receptor antagonist strychnine (1  $\mu$ M) with the residual component blocked by GABA<sub>A</sub> antagonist SR95531 (20  $\mu$ M). (B) Quantification of the glycinergic contribution to the total inhibitory current. No significant difference was observed between genotypes, confirming predominantly glycinergic transmission in both groups. (C, D) Assessment of postsynaptic receptor availability. (C) Representative currents evoked by direct somatic pressure application of glycine (0.35 mM, 10 ms) at P14 (C1) and P20 (C2). (D) Peak glycine-evoked currents are smaller in  $KCC2^{AD/AD}$  (purple) than in  $KCC2^{+/+}$  (black) at both P14 and P20, indicating an impaired development of glycine receptors. (E) Titration of GlyR responses. Representative traces (E1) and dose-dependent plot (E2) showing the relationship between glycine concentration and  $I_{gly}$ , used to determine the optimal stimulation parameters for experiments in C and D. Boxplots show median, IQR and min/max values. Individual data points represent single neurons. 2-way ANOVA with Tukey's

multiple comparison post-hoc tests.

### 3.2.2.7 Gephyrin puncta density is reduced at P14

To provide an anatomical substrate for the observed functional deficits, I quantified the density of inhibitory synapses using immunohistochemistry for the presynaptic glycine transporter GlyT2 (Jiang et al., 2024; Wiessler et al., 2025) and gephyrin as primary postsynaptic scaffold for glycine and GABA receptors (Burdina et al., 2025; Fraser et al., 2025; Macha et al., 2025).

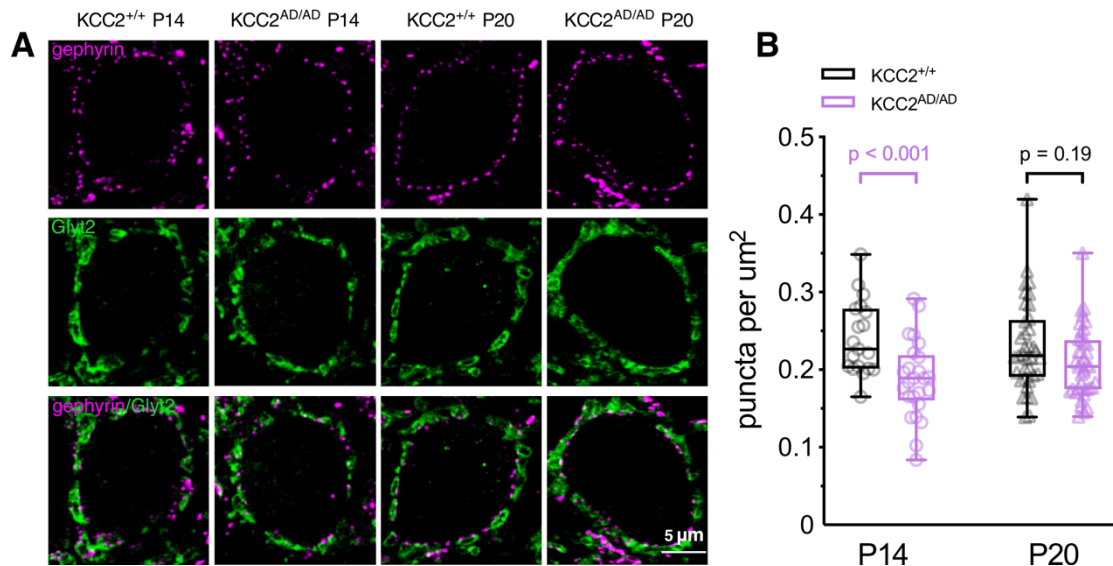


**Figure 3.12 Postsynaptic gephyrin abundance is reduced in  $KCC2^{AD/AD}$  mice of P14 LSO neurons. (A)**

Representative confocal images of LSO neurons immuno-stained for the postsynaptic scaffolding protein gephyrin (magenta, top row) and the presynaptic glycine transporter GlyT2 (green, middle row) in  $KCC2^{+/+}$  and  $KCC2^{AD/AD}$  mice at P14 and P20. The merged images (bottom row) highlight the alignment of presynaptic terminals with postsynaptic gephyrin clusters along the somatic membrane. **(B)** Quantification of gephyrin puncta density (puncta/ $\mu\text{m}^2$ ) on the somatic membrane. At P14,  $KCC2^{AD/AD}$  mice (purple) exhibit significant reduction in gephyrin cluster density compared to  $KCC2^{+/+}$  (black), mirroring the functional reduction in glycine-evoked currents. By P20, although the median density remains lower in  $KCC2^{AD/AD}$  group, the difference is not statistically significant. Boxplots show median, IQR and min/max values. Individual data points represent single neurons. 2-way ANOVA with Tukey's multiple comparison post-hoc tests.

Consistent with the reduction in puff-evoked currents, quantitative analysis revealed a significant decrease in the density of gephyrin puncta in  $KCC2^{AD/AD}$  mice at P14 compared to controls ( $p < 0.001$ ;) **(Figure 3.12)**. By P20, although the mean density remained lower in the mutant group, this difference did not reach statistical significance ( $p = 0.19$ ); and it was similar between P14 and P20 ( $KCC2^{+/+}$ :  $p = 0.42$ ,  $KCC2^{AD/AD}$ :  $p = 0.69$ ). Collectively, these structural and functional data indicate that the curtailed or abolished depolarizing phase disrupts maturation of postsynaptic receptor expression or clustering, leading to reduced glycinergic transmission.

### 3.3 Effects of enhanced KCC2 activity on LOC neurons

Before presenting the findings, an important caveat must be noted: the developmental trajectory of intracellular chloride concentration in LOC neurons has not been characterized. It is therefore unknown, whether LOC neurons experience a period of depolarizing GABA/glycine signaling during early postnatal development, and if so, when the D/H shift would occur. Addressing this question would require gramicidin-perforated patch clamp recordings to measure the reversal potential of glycinergic currents across developmental time points. Nevertheless, because LOC neurons are situated within the same superior olivary complex circuit as LSO neurons and receive glycinergic input from the same MNTB source, examining them within the same genetic model offers a valuable opportunity to investigate cell-type-specific dependencies on chloride regulation. Consequently, in the context of LOC neurons, I avoid making conclusions about the presence or timing of a D/H shift and instead focus on the effects of constitutive enhanced KCC2 transport activity driven by the  $KCC2^{AD/AD}$  genotype.

#### 3.3.1 Intrinsic membrane properties of LOC neurons are preserved

I next examined whether the development of LOC neurons is affected by the  $KCC2^{AD/AD}$  mutation, applying the same characterization used for LSO neurons. Similar to findings in the LSO (**chapter 3.2.1**), the  $R_{in}$  of LOC neurons was comparable between  $KCC2^{+/+}$  and  $KCC2^{AD/AD}$  at both P14 and P20 (P14:  $p = 0.1$ , P20:  $p = 0.93$ ). However,  $R_{in}$  was lower in  $KCC2^{AD/AD}$  neurons at P14 compared to P20 ( $p = 0.03$ ), whereas no developmental change was observed in  $KCC2^{+/+}$  neurons ( $p = 0.99$ ) (**Figure 3.13 A**). This developmental increase in  $R_{in}$  suggests that LOC neurons in  $KCC2^{AD/AD}$  mice may initially possess a larger leak conductance, reflecting a higher number of channels open at resting membrane potential. As development proceeds, this conductance is reduced, leading to an increase in  $R_{in}$  and indicating a normalization of membrane properties by P20.

The membrane time constant was similar across genotypes (P14:  $p = 0.38$ , P20:  $p = 0.68$ ), and developmental stages ( $KCC2^{+/+}$ :  $p = 0.93$ ,  $KCC2^{AD/AD}$ :  $p = 0.17$ ) (**Figure 3.13 B**). Together, this data indicates the passive intrinsic electrophysiological properties in LOC neurons keep largely intact in  $KCC2^{AD/AD}$  mice.

I next evaluated neuronal excitability by measuring rheobase. No genotype-dependent differences were detected (P14:  $p = 0.32$ , P20:  $p = 0.81$ ). However, rheobase decreased from P14 to P20 in  $KCC2^{AD/AD}$  LOC neurons ( $p = 0.02$ ), whereas no developmental change was observed in controls ( $p$

## Results

= 0.96) (**Figure 3.13 C**). This reduction is consistent with the increased  $R_{in}$  observed at P20, and suggests a modest increase in neuronal excitability during development in the mutant animals.

The characteristic delayed onset of the first spike was unaffected by the  $KCC2^{AD/AD}$  mutation (P14:  $p = 0.64$ , P20:  $p = 0.99$ ), and no developmental differences were observed ( $KCC2^{+/+}$ :  $p = 0.96$ ,  $KCC2^{AD/AD}$ :  $p = 0.98$ ) (**Figure 3.13 D**). The preservation of this firing delay suggests that the ion channel composition underlying delayed spike initiation, such as low-threshold potassium conductance, remain intact.

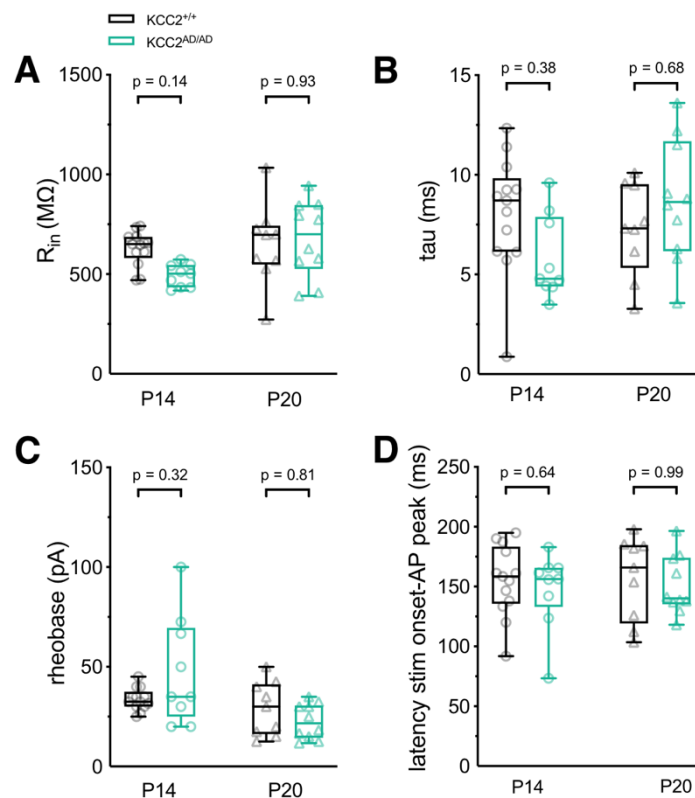


**Figure 3.13 Intrinsic membrane properties of LOC neurons develop normally in  $KCC2^{AD/AD}$  mice.** (A-C) Population data for membrane properties in LOC neurons from  $KCC2^{+/+}$  (black) and  $KCC2^{AD/AD}$  (green) mice. (A) input resistance, (B) membrane time constant, (C) rheobase current, (D) latency to the first AP. Boxplots show median, IQR and min/max values. Individual data points represent single neurons. 2-way ANOVA with Tukey's multiple comparison post-hoc tests.

AP properties were likewise unaffected. No genotype-dependent differences were observed in AP threshold (P14:  $p = 0.54$ , P20  $p = 0.89$ ) (**Figure 3.14 B**), amplitude (baseline-to-peak: P14:  $p = 0.99$ , P20:  $p = 0.80$ , **Figure 3.14 C**; threshold-to-peak: P14:  $p > 0.99$ ; P20:  $p = 0.97$ , **Figure 3.14 D**), or AHP at either age (P14:  $p > 0.99$ ; P20:  $p > 0.99$ ) (**Figure 3.14 E**). All parameters remained stable between P14 and P20, indicating that AP properties are mature by the end of the second postnatal

## Results

week (AP threshold:  $KCC2^{+/+}$ :  $p = 0.52$ ,  $KCC2^{AD/AD}$ :  $p = 0.91$ ; **Figure 3.14 B**; baseline-to-peak amplitude:  $KCC2^{+/+}$ :  $p = 0.75$ ,  $KCC2^{AD/AD}$ :  $p = 0.40$ ; **Figure 3.14 C**; threshold-to-peak amplitude:  $KCC2^{+/+}$ :  $p = 0.88$ ,  $KCC2^{AD/AD}$ :  $p = 0.63$ ; **Figure 3.14 D**; AHP:  $KCC2^{+/+}$ :  $p = 0.69$ ,  $KCC2^{AD/AD}$ :  $p = 0.81$ ; **Figure 3.14 E**).

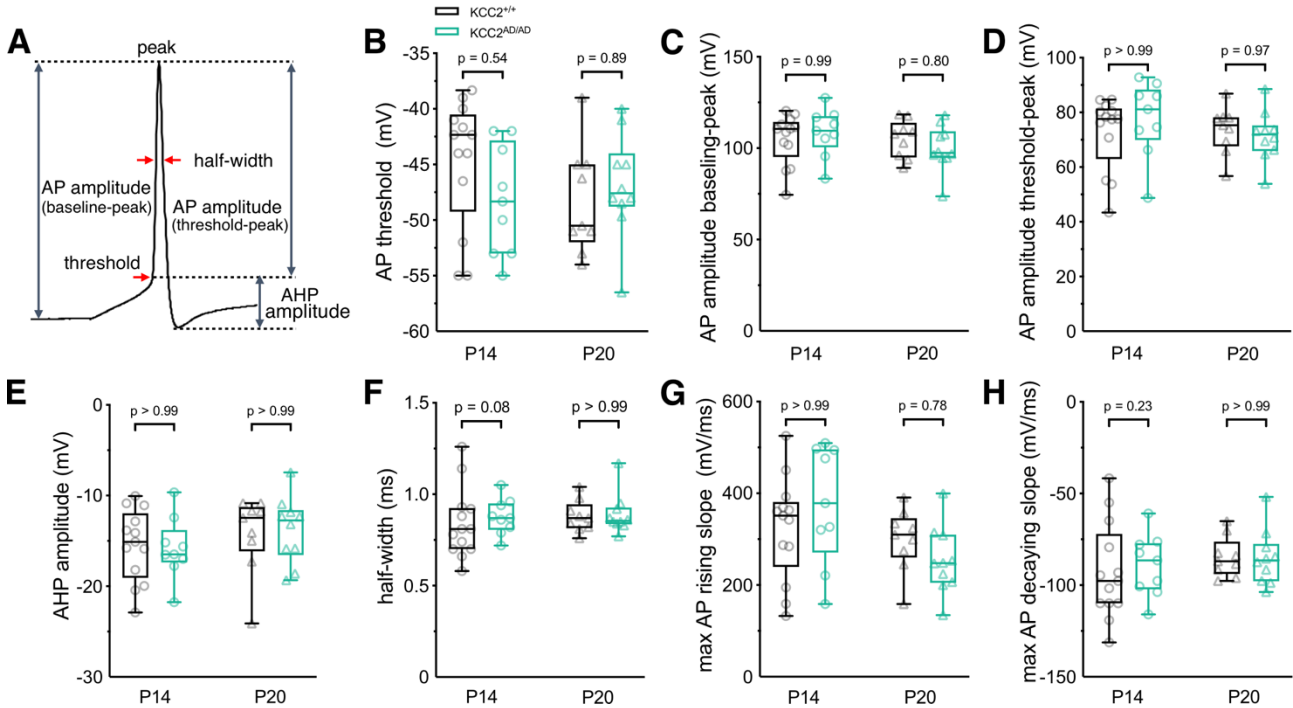


**Figure 3.14 AP properties unchanged in LOC neurons in  $KCC2^{AD/AD}$  mice.** (A) Illustrating of parameters quantified from APs. (B-H) Comparison of AP properties in LOC neurons from  $KCC2^{+/+}$  (black) and  $KCC2^{AD/AD}$  (green) mice. No genotype-dependent differences were observed in (B) AP threshold, (C) AP amplitude from baseline to peak, (D) AP amplitude from threshold to peak, (E) AHP amplitude, (F) AP half-width, (G) maximum rising slope of AP and (H) maximum decaying slope of AP. Boxplots show median, IQR and min/max values. Individual data points represent single neurons. 2-way ANOVA with Tukey's multiple comparison post-hoc tests.

Similarly, AP kinetics such as half-width and the maximum slope of depolarization and repolarization were comparable between genotypes and across ages (half-width: P14:  $p = 0.08$ , P20  $p > 0.99$ ; maximum rising slope: P14:  $p > 0.99$ , P20:  $p = 0.78$ ; Maximum decaying slope: P14:  $p = 0.23$ , P20  $p > 0.99$ ); and it was also comparable between P14 and P20 (half-width:  $KCC2^{+/+}$ :  $p = 0.07$ ,  $KCC2^{AD/AD}$ :  $p > 0.99$ ; maximum rising slope:  $KCC2^{+/+}$ :  $p = 0.50$ ,  $KCC2^{AD/AD}$ :  $p = 0.07$ ; Maximum decaying slope:  $KCC2^{+/+}$ :  $p = 0.08$ ,  $KCC2^{AD/AD}$ :  $p = 0.96$ ) (**Figure 3.15 F-H**). These results suggest that the expression of voltage-gated sodium and potassium channels responsible for determining the AP waveform develop normally in LOC neurons of  $KCC2^{AD/AD}$  mice.

### 3.3.2 Synaptic properties of LOC neurons

#### 3.3.2.1 mIPSC frequency is reduced in $KCC2^{AD/AD}$ mice

Having established that the development of intrinsic membrane properties is not impacted in  $KCC2^{AD/AD}$  mice, I next investigated synaptic properties of LOC neurons. The frequency of mIPSCs recorded in the presence of 1  $\mu$ M TTX was consistently reduced in the  $KCC2^{AD/AD}$  group (P14:  $p < 0.001$ ; P20:  $p = 0.03$ ), while it was comparable between P14 and P20 ( $KCC2^{+/+}$ :  $p = 0.07$ ,  $KCC2^{AD/AD}$ :  $p = 0.98$ ) (**Figure 3.15 C**). This reduction in mIPSC frequency was further examined by analyzing IEI. The CPD of IEIs showed a robust right-ward shift in the mutant group at both ages, reflecting longer interevent intervals, consistent with a lower frequency (**Figure 3.15 D1 and D2**). These data suggest a presynaptic deficit, potentially reflecting either a reduced probability of spontaneous vesicular release or a decreased number of functional inhibitory synaptic contacts onto LOC neurons.

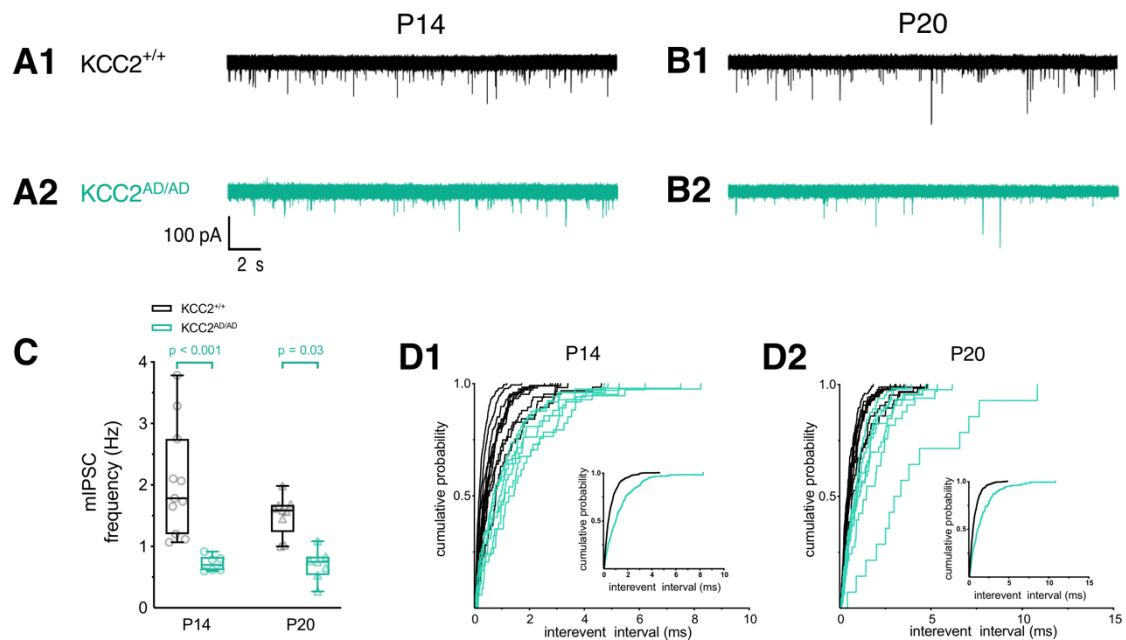


**Figure 3.15 Spontaneous synaptic release is reduced in  $KCC2^{AD/AD}$  mice.** (A, B) Representative voltage-clamp recordings of mIPSC isolated from LOC neurons in  $KCC2^{+/+}$  (black) and  $KCC2^{AD/AD}$  (green) at P14 (A) and P20 (B). Note less synaptic events in  $KCC2^{AD/AD}$  traces. (C) Population data showing a reduction in mIPSCs frequency compared to controls. (D) Cumulative probability distribution of inter-event intervals at P14 (D1) and P20 (D2). Main panels display distributions for individual cells (thin lines), while insets show the aggregated population mean. Boxplots show median, IQR and min/max values. Individual data points represent single neurons. 2-way ANOVA with Tukey's multiple comparison post-hoc tests. The total number of events analyzed for the CPD was P14:  $KCC2^{+/+}$  1336 events,  $KCC2^{AD/AD}$  272 events; P20:  $KCC2^{+/+}$  831 events,  $KCC2^{AD/AD}$  312 events.

## Results

Notably, although mIPSC frequency was reduced, their amplitude remained unchanged between genotypes (P14:  $p > 0.99$ ; P20:  $p = 0.99$ ), and amplitudes were also comparable between P14 and P20 ( $KCC2^{+/+}$ :  $p = 0.18$ ,  $KCC2^{AD/AD}$ :  $p = 0.15$ ) (**Figure 3.16**). The preservation of mIPSC amplitude indicates that postsynaptic receptor responsiveness and quantal size remain stable despite the reduction in event frequency. Together, these observations indicate that presynaptic activity or synapse number onto LOC neurons may be reduced in  $KCC2^{AD/AD}$  mice.

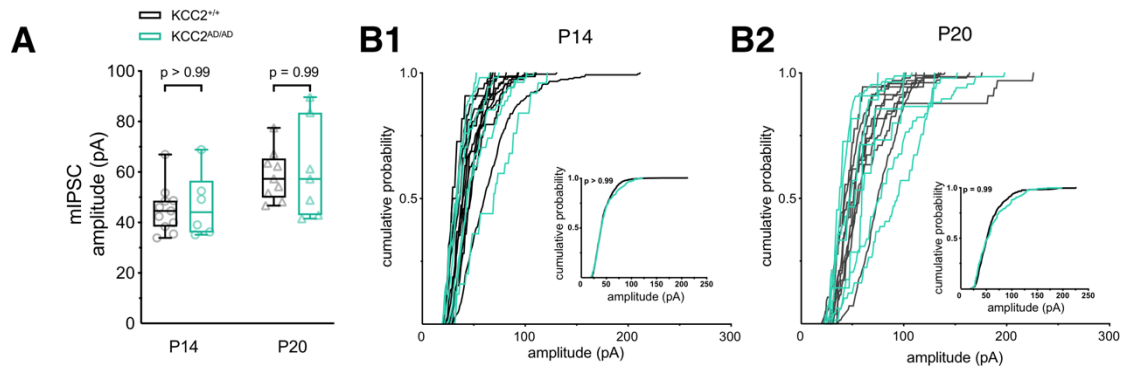


**Figure 3.16 mIPSC amplitude is preserved in LOC neurons of  $KCC2^{AD/AD}$  mice.** (A) Population data for mean mIPSC amplitudes were similar between  $KCC2^{+/+}$  (black) and  $KCC2^{AD/AD}$  (green). (B) CPD of amplitudes at P14 (B1) and P20 (B2). Main panels display distributions for individual cells (thin lines), while insets show the aggregated population mean. Boxplots show median, IQR and min/max values. Individual data points represent single neurons. 2-way ANOVA with Tukey's multiple comparison post-hoc tests. The total number of events analyzed for the CPD was P14:  $KCC2^{+/+}$  985 events,  $KCC2^{AD/AD}$  322 events; P20:  $KCC2^{+/+}$  649 events,  $KCC2^{AD/AD}$  271 events.

### 3.3.2.2 mIPSC kinetics are transiently accelerated at P14.

To further assess glycine receptor gating dynamics, I analyzed the kinetics of mIPSCs. The tau rise was significantly shorter in the  $KCC2^{AD/AD}$  group at P14 ( $p = 0.004$ ). At P20, however, tau rise was similar between genotypes ( $p = 0.83$ ), and both groups exhibited faster kinetics compared with P14 ( $KCC2^{+/+}$ :  $p < 0.001$ ,  $KCC2^{AD/AD}$ :  $p = 0.003$ ) (**Figure 3.17 A**). A comparable developmental pattern was observed for tau decay. Although a similar trend toward faster decay was present in the mutant at P14 ( $p = 0.06$ ), the values were comparable between genotypes at P20 ( $p > 0.99$ ). In both groups, decay kinetics became significantly faster with development ( $KCC2^{+/+}$ :  $p < 0.001$ ,  $KCC2^{AD/AD}$ :  $p = 0.003$ ) (**Figure 3.17 B**). These results indicate that inhibitory synaptic currents undergo normal developmental acceleration of kinetics, with a transiently shorter rise time in the mutant at P14.

## Results

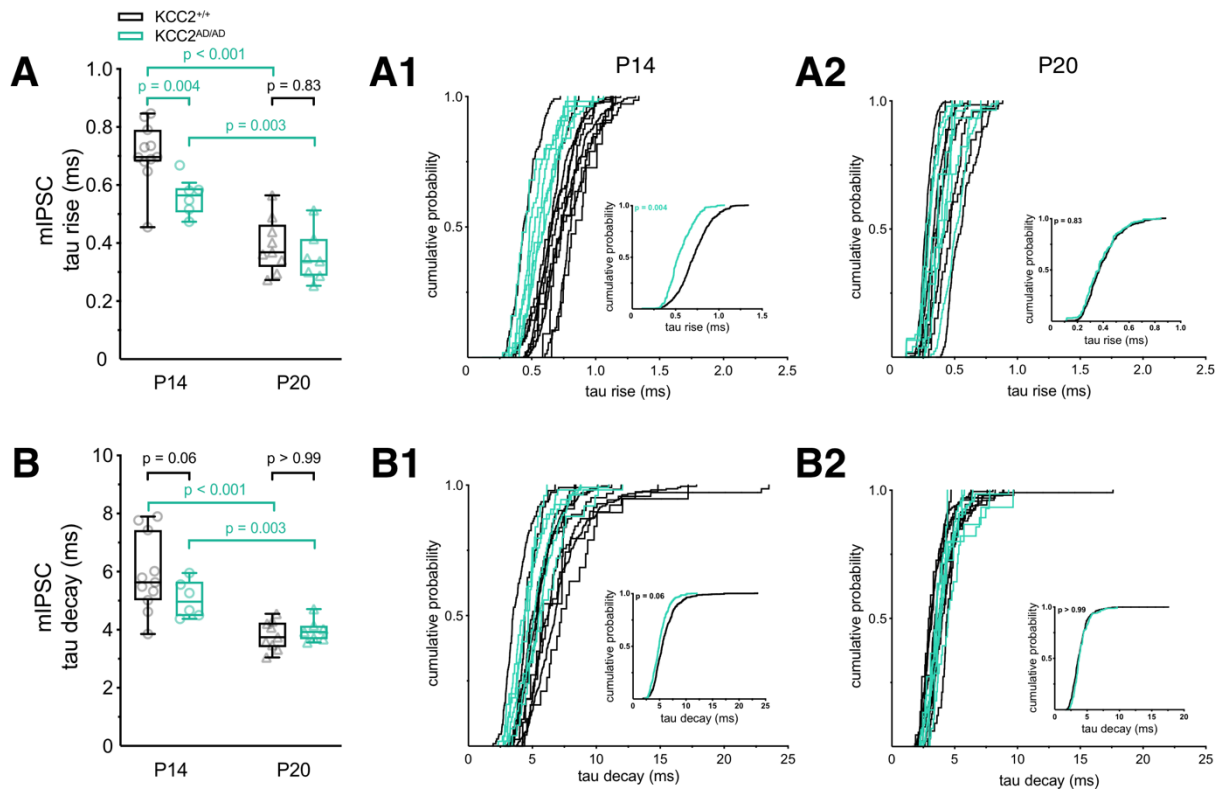


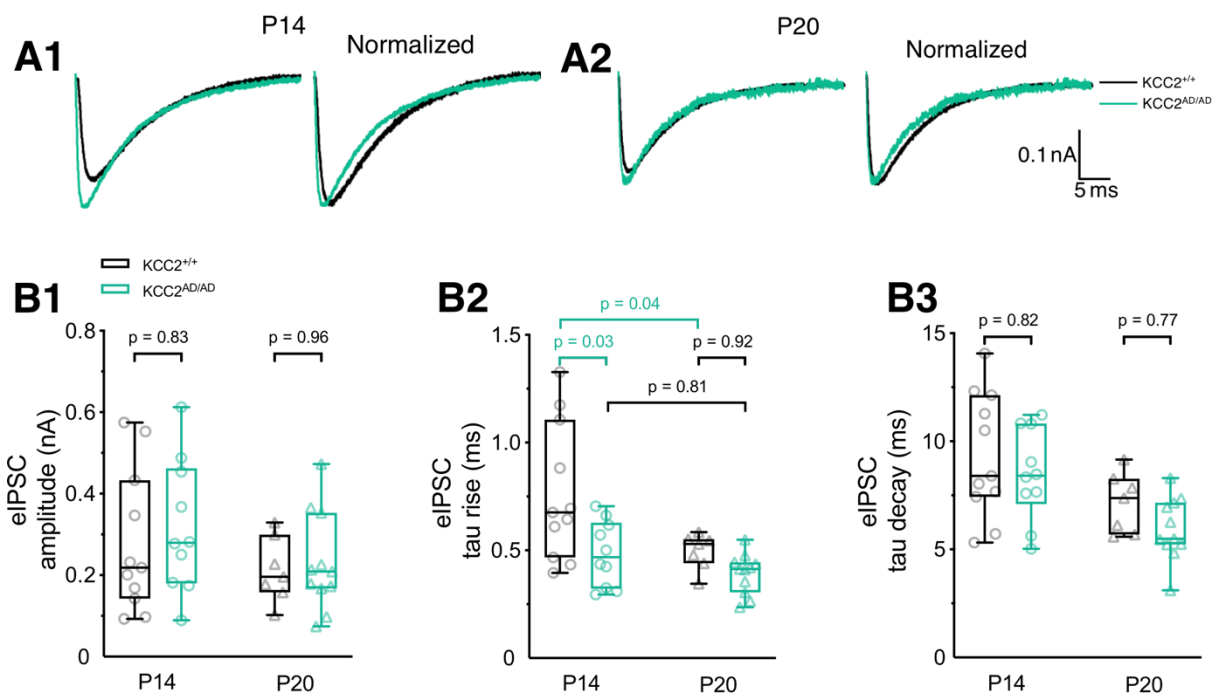
**Figure 3.17 mIPSC kinetics in LOC neurons exhibit transient acceleration in KCC2<sup>AD/AD</sup> mice at P14. (A)** Quantification of mIPSC rise time constant ( $\tau$  rise). At P14, KCC2<sup>AD/AD</sup> neurons (green) display faster rise times compared to controls (KCC2<sup>+/+</sup>, black). **(B)** mIPSC decay time constant ( $\tau$  decay) was similar between genotypes. **(A, B)** Cumulative probability distribution (CPD) of  $\tau$  rise **(A)** and  $\tau$  decay **(B)** at P14 and P20. Note the leftward shift in the P14 rise time distribution **(A1)**. Boxplots show median, IQR and min/max values. Individual data points represent single neurons. 2-way ANOVA with Tukey's multiple comparison post-hoc tests.

Taken together, these results demonstrate that in LOC neurons a persistent reduction in mIPSC frequency at both P14 and P20, as well as a shorter rise time at P14, without affecting mIPSC amplitude. This pattern suggests that for LOC neurons, it influences presynaptic aspects of inhibitory transmission rather than postsynaptic receptor strength. One possible mechanism is reduced early network activity and activity-dependent synapse formation, thereby decreasing the number or release probability of inhibitory inputs onto LOC neurons. At the same time, the unchanged amplitude and largely preserved kinetics at later stages indicate that postsynaptic receptor composition and function mature normally. The transiently faster rise kinetics observed at P14 may reflect subtle changes in receptor localization or synaptic geometry during early development, which are later compensated as synaptic circuits mature. Overall, these findings suggest that while intrinsic membrane properties remain unchanged, the development and functional organization of inhibitory synaptic inputs have been selectively influenced.

### 3.3.2.3 eIPSC amplitude is preserved despite transiently faster rise kinetics

To determine if these faster channel activation kinetics observed in  $KCC2^{AD/AD}$  at P14 persist during physiological synaptic activity, I recorded eIPSC by stimulating inhibitory inputs medial to the LSO or in the MNTB. Consistent with mIPSC data, single eIPSC at P14 exhibited faster rise time in  $KCC2^{AD/AD}$  compared to controls ( $p = 0.03$ ). However, the tau rise was similar at P20 ( $p = 0.92$ ). Developmentally, the control group showed a speeding of rise kinetics from P14 to P20 ( $p = 0.04$ ), while in  $KCC2^{AD/AD}$  remained unchanged at P20 ( $p = 0.81$ ) (**Figure 3.18 B2**). This suggests accelerated early synaptic kinetics, resulting in a transient developmental advance that later converges with control values.

In contrast to observations in LSO neurons, eIPSC amplitude was not affected in LOC neurons from  $KCC2^{AD/AD}$  mice (P14:  $p = 0.83$ , P20:  $p = 0.96$ ). Moreover, amplitudes remained stable across development ( $KCC2^{+/+}$ :  $p > 0.99$ ,  $KCC2^{AD/AD}$ :  $p = 0.39$ ) (**Figure 3.18 B1**), indicating normal development of inhibitory strength. Similarly, the tau decay was comparable between genotypes (P14:  $p = 0.83$ , P20:  $p = 0.96$ ), and did not change between P14 and P20 ( $KCC2^{+/+}$ :  $p = 0.22$ ,  $KCC2^{AD/AD}$ :  $p = 0.09$ ) (**Figure 3.18 B3**). These results further support the idea that postsynaptic receptor function and the overall synaptic current profile during evoked transmission remain intact in LOC neurons.



## Results

**Figure 3.18 eIPSC are transiently accelerated in LOC neurons of  $KCC2^{AD/AD}$  mice. (A)** Representative eIPSCs recorded from LOC neurons at P14 (**A1**) and P20 (**A2**). (Left) Superimposed traces showing comparable amplitudes between  $KCC2^{+/+}$  (black) and  $KCC2^{AD/AD}$  (green) mice. (Right): Peak-scaled traces revealing the faster rise time in the P14  $KCC2^{AD/AD}$  group. (**B1**) eIPSC amplitudes in  $KCC2^{AD/AD}$  mice are comparable to controls. (**B2**) Rise time constants are faster in  $KCC2^{AD/AD}$  at P14, but they are similar at P20. (**B3**) Decay time constants are similar between genotypes at both ages. Boxplots show median, IQR and min/max values. Individual data points represent single neurons. 2-way ANOVA with Tukey's multiple comparison post-hoc tests.

To examine short-term synaptic dynamics, I applied stimulus trains at 10, 50, and 100 Hz to evaluate STP. Both genotypes displayed comparable levels and time courses of STD at both P14 (**Figure 3.19**) and P20 (**Figure S.2**). This suggests that presynaptic release probability and vesicle recycling during action potential-evoked transmission develop normally. Together, these data suggest that although spontaneous inhibitory transmission is reduced, the fundamental machinery underlying activity-dependent synaptic release follows physiological development.

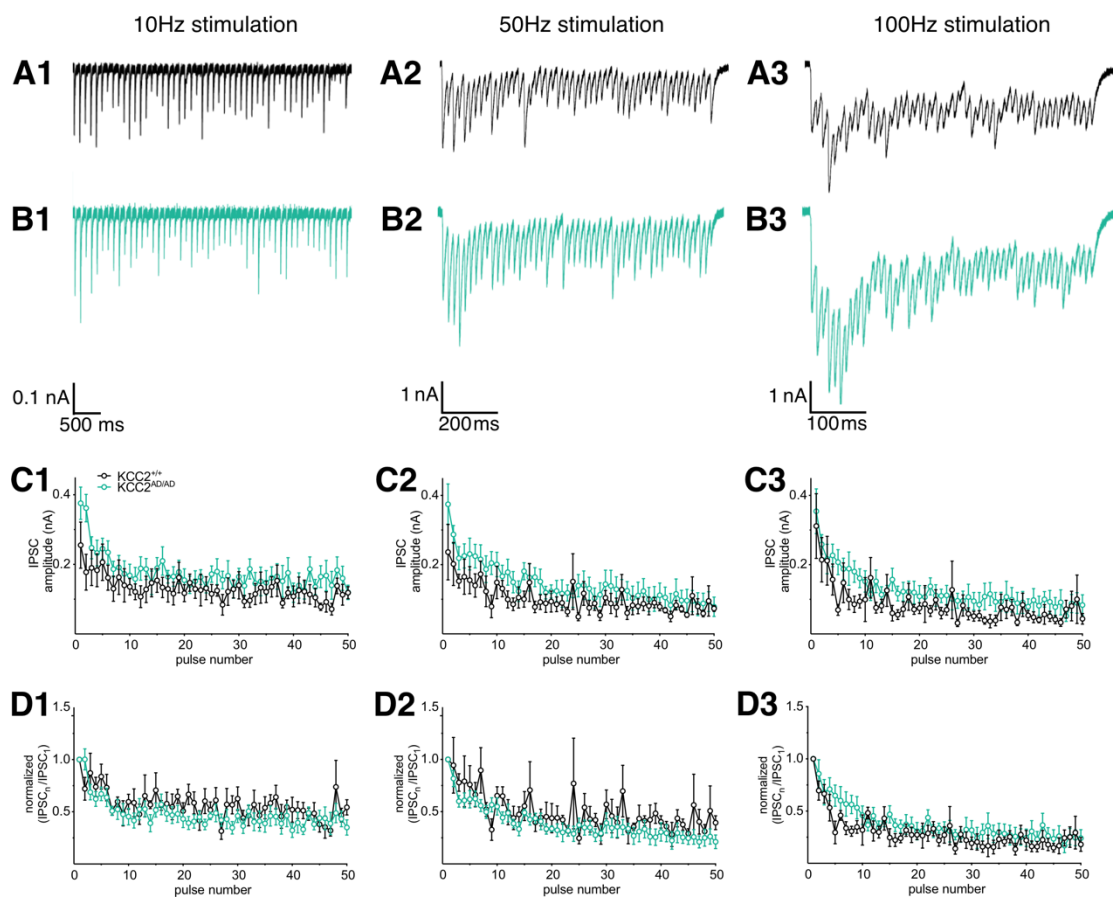


**Figure 3.19 Normal short-term plasticity in LOC neurons from  $KCC2^{AD/AD}$  mice at P14. (A, B)** Representative eIPSC from LOC neurons in  $KCC2^{+/+}$  (**A**, black) and  $KCC2^{AD/AD}$  (**B**, green) mice in response to stimuli delivered at 10 Hz (left),

### Results

50Hz (middle) and 100Hz (right). Both genotypes exhibited comparable short-term depression. **(C)** eIPSC amplitudes recorded at P14 and plotted against pulse number for different stimulus frequencies. **(D)** Normalized synaptic depression profile (IPSCn/IPSC1). Depression and steady-state levels are similar between genotypes and across stimulus frequencies. The error bar in **C** and **D** shows SEM.

Taken together, these findings indicate that the  $KCC2^{AD/AD}$  mutation selectively alters specific aspects of inhibitory synaptic development in LOC neurons. The reduced mIPSC frequency points to a presynaptic alteration, such as a decreased number of inhibitory synaptic contacts or reduced spontaneous vesicle release probability. However, the preservation of IPSC amplitude, decay kinetics, and STD suggests that the postsynaptic receptor complement and the mechanisms supporting AP-evoked transmitter release are largely unaffected.

Overall, the  $KCC2^{AD/AD}$  mutation exerts distinct effects on the two neuronal populations examined. In LSO neurons, inhibitory synaptic transmission is weakened through reduced IPSC amplitudes, potentially reflecting a decreased number of glycine receptors at postsynaptic sites. In contrast, LOC neurons primarily exhibit a reduction in spontaneous inhibitory input frequency, indicating presynaptic alterations in synapse number or spontaneous release activity. Importantly, these presynaptic changes do not translate into deficits in AP-evoked transmission, suggesting that activity-dependent release mechanisms and synaptic strength during evoked signaling remain intact. These differences highlight cell-type-specific sensitivity of inhibitory circuit development to the timing of chloride homeostasis maturation, possibly reflecting distinct developmental programs or patterns of activity-dependent synaptic refinement within the LSO–LOC network.

## 4 Discussion

In this thesis, I systematically investigated the developmental consequences of a curtailed or abolished depolarizing inhibition on the maturation of LSO and LOC neurons and their respective inhibitory inputs. By leveraging the  $KCC2^{AD/AD}$  mouse model, in which constitutively enhanced chloride extrusion curtails or abolishes the depolarizing window, I uncoupled the timing of chloride extrusion from other developmental milestones and revealed a dissociation between intrinsic and synaptic development. Comprehensive electrophysiological profiling demonstrated that the intrinsic excitability of both neuronal populations is remarkably resilient to chloride dysregulation, with no significant alterations in passive membrane properties or AP dynamics. In contrast, synaptic maturation was sensitive to the timing of the D/H shift and manifested in a cell-type specific pattern. LSO neurons exhibited a postsynaptic deficit, characterized by reduced synaptic amplitude and a corresponding loss of glycine receptors, whereas LOC neurons displayed a presynaptic deficit, defined by a reduction in frequency of spontaneous SV release. Together, these results suggest that the temporal regulation of chloride homeostasis primarily drives synaptic development with little or no contribution to the maturation of intrinsic excitability.

### 4.1 Rationale for using the $KCC2^{AD/AD}$ mouse model

The principal aim of this study was to investigate how the curtailing the period of depolarizing inhibition influences the maturation of LSO and LOC neurons. To address this question, I used a constitutive  $KCC2$  phospho-mutant mouse model ( $KCC2$  Thr934Ala/Ser937Asp;  $KCC2^{AD/AD}$ ), previously characterized by Radulovic et al (2023). This model carries a double mutation that mimics constitutive phosphorylation at serine 937—a potent phospho-site that enhances  $KCC2$  transport activity—while locking the neighboring threonine 934 in a dephosphorylated state. The choice of this model was guided by several considerations.

First, the  $KCC2^{AD/AD}$  mutation produces a two-fold increase in  $KCC2$  transport activity in heterologous expression systems and accelerates the developmental onset of hyperpolarizing glycinergic responses in LSO (Radulovic et al., 2023). This provides a well-defined genetic tool to examine the consequences of a curtailed or abolished depolarizing phase. This gain-of-function approach complements the more commonly studied loss-of-function models that delay or prevent this transition. The auditory brainstem, and particularly the LSO, is a suitable model system for such investigations because the developmental timeline of its inhibitory circuitry has been extensively characterized.

MNTB-LSO contacts from embryonically, followed by giant depolarizing potentials occurring during the first postnatal week, functional silencing of inappropriate connections taking place between approximately P3 and P7, the transmitter phenotype switches from GABA to glycine during the first two postnatal weeks, axonal pruning occurring after hearing onset, and finally synaptic strengthening (Kandler & Friauf, 1993; Löhrke et al., 2005; Nabekura et al., 2004; Sanes & Siverls, 1991). This foundation of normative data enables precise interpretation of how curtailing the early depolarizing inhibition alters specific developmental milestones.

Second, the  $KCC2^{AD/AD}$  model makes it possible to dissect the direct effects of altered chloride homeostasis from the indirect consequences of changed network activity. Unlike manipulations that abolish sensory experience, such as cochlear ablation (Shibata et al., 2004), or globally suppress activity, the  $KCC2$ -gain-of-function mutation enhances chloride extrusion cell-autonomously, thereby prematurely terminating or abolishing the period during which GABA/glycine is depolarizing. This allows one to ask specifically which aspects of LSO and LOC neuron development depend on the presence of depolarizing inhibition during the critical postnatal window.

Third, the LSO and LOC present a valuable comparative paradigm. Both cell types receive glycinergic inputs and are situated within the same nucleus, yet they serve different functions (LSO: binaural sound localization; LOC: cochlear efferent modulation) and exhibit different developmental profiles. Examining both populations within the same genetic model provides insight into cell-type-specific dependencies on depolarizing inhibition. This comparison is particularly informative because the developmental trajectory of chloride maturation in LOC neurons remains entirely unknown. Determining whether LOC neurons undergo a similar D/H shift to that observed in LSO or whether they maintain a distinct chloride regulation profile tied to their later-maturing efferent role, could reveal fundamental principles governing how synaptic inhibition is sculpted to meet cell-type-specific functional demands.

## **4.2 Preserved intrinsic excitability versus altered synaptic properties**

### **4.2.1 Intrinsic properties develop independently of depolarizing inhibition**

A comprehensive analysis of passive and active intrinsic membrane properties revealed no significant differences between  $KCC2^{+/+}$  and  $KCC2^{AD/AD}$  mice in either LSO or LOC neurons at P14 or P20. Input resistance, membrane time constant, rheobase, sag potential amplitude (reflecting HCN channel function), and action potential waveform parameters (threshold, amplitude, half-width,

rise/decay kinetics) were all indistinguishable between genotypes (**Figures 3.3, 3.4 for LSO, 3.13, 3.14 for LOC**).

These findings demonstrate that the maturation of voltage-gated sodium and potassium channels, HCN channels, and the overall membrane architecture governing passive properties are guided by developmental mechanisms other than depolarizing inhibition. This conclusion aligns with observations from another KCC2 phospho-mutant model: Moore et al. (2018) reported that KCC2-T906A/T1007A mice, which also exhibit enhanced KCC2 function, showed no alterations in basal neuronal excitability.

The implication is that intrinsic excitability is governed by molecular programs largely autonomous from chloride homeostasis. These programs likely involve transcription factors (e.g., REST, NRSF), neurotrophic signaling (e.g., BDNF), and homeostatic activity-dependent mechanisms that do not depend solely on the polarity of GABA/glycine responses (Park & Poo, 2013; Pozzi et al., 2013; Turrigiano, 2011). Two caveats should be noted, however. First, somatic whole-cell recordings may not capture more subtle changes in subthreshold conductance or dendritic excitability. Second, although intrinsic properties at the ages examined here were indistinguishable between genotypes, it is possible that they were transiently altered during the first few postnatal days but had already been restored by homeostatic mechanisms by the time of recording.

#### 4.2.2 Synaptic properties exhibit cell-type-specific alterations

In contrast to the preserved intrinsic properties, inhibitory transmission was altered in both LSO and LOC neurons, but with qualitatively distinct phenotypes.

##### 4.2.2.1 LSO neurons: postsynaptic reduction in glycine receptor number

In LSO neurons of KCC2<sup>AD/AD</sup> mice, I observed a consistent reduction in the amplitude of both mIPSCs (**Figure 3.6**) and eIPSCs (**Figure 3.8**) at P14 and P20. Importantly, mIPSC frequency (**Figure 3.5**) and kinetics (rise and decay times; **Figure 3.7**) were unchanged, and the  $E_{Cl^-}$  was identical between genotypes when measured with Cs-gluconate internal solution (**Figure 3.10**). These findings collectively argue against a presynaptic locus (which would be expected to alter frequency) and against an altered driving force for chloride (which would shift  $E_{Cl^-}$ ). Instead, they point toward a reduction in the number or function of postsynaptic glycine receptors.

Three independent lines of evidence support this postsynaptic interpretation. First, direct application of glycine produced smaller currents in KCC2<sup>AD/AD</sup> LSO neurons (**Figure 3.11**), indicating a reduced

postsynaptic receptor complements independent of presynaptic release. Second, immunohistochemical quantification revealed a reduction in the density of gephyrin puncta—the scaffolding protein essential for glycine and GABA receptor clustering—in the LSO of mutant mice at P14 (**Figure 3.12**). That a similar trend persisted at P20 without reaching statistical significance may reflect a limitation of confocal imaging resolution and two-dimensional analysis. Further quantification using super-resolution microscopy with nanobodies to better separate individual puncta combined with three-dimensional reconstruction methods could help resolve this. Third, the preservation of mIPSC frequency and short-term plasticity dynamics argues against altered presynaptic release probability or reduced numbers of release sites.

These findings indicate that premature termination of the depolarizing phase impairs the expression or stabilization of postsynaptic glycine receptors in LSO neurons. This interpretation is consistent with the established role of depolarizing GABA/glycine in promoting synapse maturation: In the developing hippocampus, depolarizing GABA drives calcium influx through VGCCs which facilitates activity-dependent maturation of inhibitory synapses and stabilization of postsynaptic scaffolding proteins including gephyrin (Ben-Ari et al., 2007; Owens & Kriegstein, 2002; Tyagarajan & Fritschy, 2014). The developmental timeline of the LSO is particularly instructive in this context. Functional silencing of aberrant MNTB-LSO connections occurs during the first postnatal week (P3-P7), a period when GABA/glycine is still depolarizing. This silencing involves LTD-like mechanisms that depend on GABA/glycine-mediated calcium transients (Gillespie et al., 2005; Kim & Kandler, 2003). Subsequently, from approximately P7 onward, the surviving connections are strengthened (Kim & Kandler, 2003, 2010). My data suggest that curtailing the depolarizing window primarily compromises this later strengthening phase, resulting in fewer functional glycine receptors at surviving synapses.

#### 4.2.2.2 LOC neurons: presynaptic reduction in release frequency

In contrast to LSO neurons, LOC neurons from  $KCC2^{AD/AD}$  mice exhibited a markedly reduced mIPSC frequency at P14 and P20 (**Figure 3.15**), with no change in mIPSC or eIPSC amplitudes (**Figure 3.16; 3.18**) and only minor kinetic alterations (tau rise at P14; **Figure 3.17; 3.18**). This pattern of reduced frequency and preserved amplitude is characteristic for a presynaptic phenotype (Koyama et al., 2002), indicating either fewer release sites or reduced spontaneous release probability.

### 4.2.3 Cell-type-specific engagement of pre- and postsynaptic mechanisms

The cell-type-specificity of the observed phenotypes (LSO: postsynaptic; LOC: presynaptic) underscores a key principle: depolarizing inhibition serves multiple developmental functions that are differentially engaged depending on the neuron's identity, synaptic architecture, and developmental process.

#### **Mechanistic basis in LSO neurons**

In LSO principal neurons, which receive highly convergent MNTB input that is subsequently refined through competitive processes, depolarizing inhibition appears critical for the postsynaptic consolidation phase. The reduction of the IPSCs amplitude and gephyrin puncta density suggests that curtailed depolarizing phase disrupts the signaling cascade that establish or stabilizes glycine receptor clusters. This cascade likely involves calcium influx through VGCCs and NMDA receptors, the latter being co-activated by depolarizing GABA/glycine and co-released glutamate in the immature LSO (Gillespie et al., 2005; Kandler & Gillespie, 2005). Downstream, calcium-calmodulin-dependent protein kinases (CaMKII) phosphorylates glycine receptor subunits and gephyrin, promoting their synaptic accumulation (Mukherjee et al., 2011; Tyagarajan & Fritschy, 2014). By shortening this maturation phase, the  $KCC2^{AD/AD}$  mutation potentially reduces the VGCC activation and calcium influx, thereby weakening this developmental signal.

#### **Mechanistic basis in LOC neurons**

LOC neurons are cholinergic efferent neurons that also co-release GABA and glycine and project to the cochlea (Fujino et al., 1997; Guinan, 2018; Warr & Guinan, 1979). Their inhibitory inputs from the MNTB are less well-characterized than those to the LSO, and the developmental trajectory of chloride maturation in LOC neurons remains unknown. The presynaptic phenotype observed here suggests that depolarizing inhibition plays a distinct role in the development of the presynaptic terminal itself. Several mechanisms could account for this observation. Depolarizing GABA/glycine might act on presynaptic GABA<sub>A</sub> or glycine receptors on MNTB terminals contacting LOC neurons, facilitating calcium influx and thereby promoting growth cone stabilization or synaptic vesicle clustering. Alternatively, the depolarizing phase might be required for the proper development of the LOC neuron's own efferent terminals in the cochlea, engaging homeostatic feedback to its afferent inputs.

## **Comparative analysis: Synaptic architecture dictates the dependency on depolarizing inhibition**

The distinct phenotypes in LSO and LOC neurons likely reflect fundamental differences in their synaptic organization. In the LSO, MNTB inputs evoke large-amplitude IPSCs, reaching several nanoamperes (Haragopal et al., 2025; Kim & Kandler, 2003; Sterenborg et al., 2010), and these synapses undergo robust strengthening and fastening during maturation, which is essential for precise ILD processing. In contrast, IPSCs recorded in LOC neurons are markedly smaller in amplitude and exhibit slower kinetics (Hong et al., 2022; Sterenborg et al., 2010) reflecting a fundamentally different synaptic configuration.

This divergence in synaptic conductance has important implications for how these two cell types depend on depolarizing inhibition during development. Even if LOC neurons do experience a period of depolarizing inhibition, its functional impact may be limited by the weakness of their glycinergic inputs. Small-amplitude, slow IPSCs are unlikely to generate the strong depolarizations required to drive calcium-dependent developmental processes, such as the receptor clustering or synaptic strengthening. In this scenario, the loss of depolarizing inhibition would be less consequential for LOC neurons than for LSO neurons, where powerful MNTB inputs rely on depolarizing GABA/glycine to drive the calcium signals necessary for postsynaptic consolidation.

These considerations highlight that the requirement for depolarizing inhibition is not uniform but is instead dictated by cell-type-specific synaptic architecture and developmental trajectories. The observation that different cell types within the same brain region employ distinct developmental strategies underscores the complexity of activity-dependent circuit assembly and emphasizes the importance of studying multiple neuronal populations when assessing the consequences of a genetic manipulation affecting chloride homeostasis.

### **4.3 Cellular mechanisms linking depolarizing inhibition to synapse maturation**

#### **4.3.1 Calcium signaling as a key regulatory process**

The most parsimonious explanation for the observed synaptic deficits centers on disrupted calcium signaling. In immature neurons, depolarizing GABA/glycine activates VGCCs, producing locally restricted intracellular calcium transients that trigger gene expression, cytoskeletal reorganization,

and synaptic maturation (Ganguly et al., 2001; Gillespie et al., 2005; Leinekugel et al., 1997). In the LSO, specifically, depolarizing MNTB inputs activate VGCCs in LSO dendrites, generating spatially restricted calcium signals (Gillespie et al., 2005).

In  $KCC2^{AD/AD}$  mice, the absence of depolarizing or premature shift to hyperpolarizing inhibition would reduce or eliminate this developmental calcium source. Two downstream consequences are likely. First, diminished calcium influx would reduce activation of CaMKII, which phosphorylates glycine receptor subunits and gephyrin to enhance their synaptic clustering (Flores et al., 2015). Second, calcium-dependent gene expression mediated by transcription factors such as CREB would be attenuated, potentially reducing transcription of genes encoding glycine receptor subunits or scaffolding proteins. The reduction in gephyrin puncta density observed at P14 is consistent with both of these mechanisms.

### **4.3.2 NMDA receptor signaling**

In the immature LSO, MNTB terminals co-release glutamate together with GABA and glycine, activating NMDA receptors on LSO neurons (Gillespie et al., 2005; Kandler & Gillespie, 2005). NMDA receptor activation is critically involved in synaptic refinement and the induction of LTD at MNTB-LSO synapses (Case & Gillespie, 2011; Noh et al., 2010). Crucially, NMDA receptor activation is voltage-dependent, requiring sufficient membrane depolarization to relieve the  $Mg^{2+}$  block (Mayer et al., 1984; Nowak et al., 1984). In the developing LSO, depolarizing GABA/glycine provides this permissive depolarization (Goutman et al., 2005; Kandler & Friauf, 1995). In  $KCC2^{AD/AD}$  mice, premature hyperpolarization of the postsynaptic membrane would enhance the  $Mg^{2+}$  block, reducing NMDA receptor activation when glutamate is released. This could impair NMDA receptor-dependent synaptic refinement. However, the unchanged mIPSC frequency in LSO neurons argues against a major disruption of synaptic pruning, which would be expected to alter the number of functional inputs. Rather, NMDA receptor hypoactivation may primarily affect the consolidation and strengthening of surviving synapses—a process that also depends on NMDA receptor-mediated calcium influx (Case & Gillespie, 2011). The specific involvement of NMDA receptors in the postsynaptic consolidation deficit observed here remains to be investigated.

### **4.3.3 BDNF signaling**

BDNF is a key regulator of inhibitory synapse development, acting through TrkB receptors to promote GABAergic and glycinergic synapse formation and maturation (Huang et al., 1999; Rico et

al., 2002). Both BDNF expression and release are activity-dependent and calcium-regulated (Balkowiec & Katz, 2002; Goggi et al., 2003). Because depolarizing GABA/glycine elevates intracellular calcium, absence or premature termination of the depolarizing phase could reduce BDNF synthesis or secretion, thereby impairing downstream inhibitory synapse maturation. In the LSO, BDNF derived from either MNTB terminals or LSO neurons themselves could act in a paracrine or autocrine manner to regulate glycine receptor clustering. The reduction in gephyrin puncta observed in LSO principal neurons of  $KCC2^{AD/AD}$  mice at P14 might reflect diminished BDNF/TrkB signaling during the first two postnatal weeks—the critical period for MNTB-LSO synapse refinement (Kim & Kandler, 2003, 2010). This is consistent with evidence that TrkB signaling regulates gephyrin phosphorylation and clustering at developing inhibitory synapses (Mou et al., 2013).

#### 4.3.4 Cell-type-specific differences in calcium handling

The differential phenotypes in LSO and LOC neurons may reflect differences in their calcium-handling machinery. LSO neurons express high levels of calcium-binding proteins such as parvalbumin and calbindin (Friauf, 1994, 1993; Lohmann & Friauf, 1996), their strong calcium buffering capacity may, paradoxically, render them highly dependent on robust depolarization-induced calcium influx for postsynaptic maturation, because buffered calcium signals require stronger sources to reach the threshold for downstream signaling cascades. When the depolarizing window is curtailed or absent, the already buffered calcium may fall below this threshold, resulting in impaired receptor stabilization. LOC neurons, which may express a different complement of calcium buffers or VGCC subtypes, could be less sensitive to the reduced calcium influx in the postsynaptic compartment but more vulnerable to presynaptic effects operating through distinct mechanisms. Alternatively, these two cell types may have different critical periods during which depolarizing inhibition is required, and the boundaries of these windows might not align with the premature hyperpolarizing inhibition produced by the  $KCC2^{AD/AD}$  mutation.

#### 4.4 Limitations and technical considerations

Several limitations of this study should be acknowledged.

First, the electrophysiological recordings were performed in acute brain slices: While slice preparations offer precise control over experimental conditions and are well-suited for isolating cell-autonomous and local circuit effects, they lack the full complement of modulatory inputs present *in*

### Discussion

*vivo* (e.g., serotonergic, cholinergic afferents from more distant brain regions) and do not fully recapitulate physiological activity patterns.

Second, the analysis was restricted to two age points (P14 and P20). While these capture key developmental transitions surrounding hearing onset and post-hearing maturation, they may miss transient phenotypes at earlier or intermediate ages. For example, the reduction in gephyrin puncta at P14 might be preceded by a more pronounced deficit at earlier ages (e.g. P10), or it might reflect a developmental phase that eventually normalizes in adulthood. Future studies should examine additional time points, including more immature and adult animals (P60+), to determine whether the observed deficits persist or are eventually compensated.

Third, the immunohistochemical analysis was limited to gephyrin. Although gephyrin is a reliable marker of inhibitory postsynaptic sites, it is an indirect marker for glycine receptor and also scaffolds GABA<sub>A</sub> receptors. It does not distinguish between synaptic and extrasynaptic receptor clusters and provides no information about receptor subunit composition. Immunostaining for glycine receptor  $\alpha$  subunits would complement the gephyrin data. Additionally, ultrastructural analysis by electron microscopy would be required to definitively determine whether synapse number is reduced or whether existing synapses contain fewer receptors.

Fourth, it cannot be excluded that developmental changes within the MNTB contribute to the observed phenotypes. The KCC2<sup>AD/AD</sup> mutation is constitutively expressed in all neurons, including MNTB cells and upstream nuclei. Altered development of MNTB neurons—their intrinsic properties, transmitter release machinery, or axon targeting—could indirectly affect synapse development in both LSO and LOC. Cell-type-specific conditional approaches would be required to definitively dissect cell-autonomous from non-autonomous contributions.

Fifth, this study did not assess the functional consequences of the synaptic alterations for auditory processing. Reduced glycinergic input to LSO neurons, without similar changes to the excitatory inputs, would be predicted to impair binaural processing, specifically interaural level difference coding (Grothe et al., 2010), but this hypothesis remains untested. Future work should combine *in vivo* electrophysiology with behavioral assessments of sound localization to determine whether the synaptic deficits observed *in vitro* translate into measurable functional impairments.

## 4.5 Future directions

The findings of this study open several avenues for future investigation.

**Characterization of chloride maturation in LOC neurons.** A critical unanswered question is whether LOC neurons undergo a D/H shift during development, and if so, when this transition occurs. Gramicidin-perforated patch clamp recordings across postnatal ages (P0–P20) would directly measure the reversal potential of glycinergic currents in LOC neurons. This information is essential for interpreting how enhanced KCC2 transport activity affects LOC development and for determining whether the observed presynaptic phenotype reflects disruption of a depolarizing window or a distinct mechanism.

**Estimation of single-channel conductance.** The reduction in mIPSC amplitude in LSO neurons could reflect either decreased single-channel conductance or a reduction in the number of functional glycine receptors. Non-stationary fluctuation analysis of mIPSCs or eIPSCs would distinguish between these possibilities by determining single-channel current amplitude and the number of open receptors. This analysis would clarify whether the postsynaptic deficit is primarily due to altered receptor properties or reduced receptor clustering, and is currently being pursued.

**Ultrastructural analysis.** Electron microscopy with immunogold labeling for glycine receptors and gephyrin would provide definitive quantification of synapse number, postsynaptic density area, and receptor density per synapse. This approach would distinguish between a reduction in total synapse number and a reduction in receptor content per synapse (Gjoni et al., 2018)– two scenarios that carry different implications for circuit function.

**Functional assessment of auditory processing.** In vivo recordings from LSO neurons in anesthetized or awake KCC2<sup>AD/AD</sup> mice (Muniak et al., 2012; Navawongse & Voigt, 2009) could assess frequency tuning and binaural response properties. Pairing such recordings with behavioral assessments of sound localization performance, would determine whether the synaptic deficits observed in vitro translate into measurable impairments in auditory function.

**Examination of other auditory brainstem nuclei.** The MSO, which also receives glycinergic input from the MNTB and undergoes experience-dependent refinement (Kapfer et al., 2002; Werthat et al., 2008), should be examined to determine whether it shows an LSO-like postsynaptic phenotype. Such comparison would clarify whether the differential engagement of developmental mechanisms is cell-type or nucleus-specific.

## **4.6 Conclusion**

This study demonstrates that curtailing or abolishing the period of depolarizing inhibition through constitutive activation of KCC2, selectively alters inhibitory synapse development in a cell-type-specific manner while leaving intrinsic membrane properties intact. In LSO neurons, the curtailed or abolished depolarizing phase produces a postsynaptic deficit, featuring reduced glycinergic currents and decreased gephyrin puncta density, indicating impaired formation or stabilization of inhibitory postsynaptic sites. In LOC neurons, it produces a presynaptic phenotype with reduced mIPSC frequency, suggesting altered spontaneous release probability or fewer functional release sites. These findings establish that the duration of the depolarizing window is critical for normal inhibitory synapse maturation and reveal that different neuronal populations engage depolarizing inhibition through pre-and postsynaptic mechanisms.

The dissociation between preserved intrinsic properties and altered synaptic development highlights a fundamental principle: intrinsic and synaptic maturation are governed by separate regulatory programs. Intrinsic excitability follows developmental trajectories that are insensitive to the polarity of GABA/glycine signaling, whereas synaptic refinement depends critically on the precise timing of depolarizing inhibition. The KCC2<sup>AD/AD</sup> mouse model provides a valuable tool for further dissecting how depolarizing inhibition instructs circuit assembly and for understanding how disruptions in this process may contribute to auditory processing deficits and, more broadly, to neurodevelopmental disorders associated with altered chloride homeostasis.

## 5 Abbreviations

ACh	Acetylcholine
aCSF	artificial cerebrospinal fluid
AE3	Anion exchanger 3
AHP	Afterhyperpolarization
AP	Action potential
AVCN	Anteroventral cochlear nucleus
BDNF	Brain-Derived Neurotrophic Factor
CaMKII	Calcium-calmodulin-dependent protein kinases
CCCs	Cation-chloride cotransporters
CGRP	Calcitonin gene-related peptide
$[Cl^-]_i$	Intracellular chloride concentration
CN	Cochlea nucleus
CNQX	6-Cyano-7-nitroquinoxaline-2,3-dione
CPD	Cumulative probability distribution
I-V	Current-voltage
D-AP5	D-2-amino-5-phosphonopentanoic acid
D/H	Depolarization-to-hyperpolarization
$E_{GABA/Gly}$	Equilibrium potential for GABA/glycine
eIPSC	Evoked inhibitory postsynaptic current
GABA	$\gamma$ -aminobutyric acid
GBC	Globular bushy cell
GlyR	Glycine receptor
HCN	Hyperpolarization-activated Cyclic Nucleotide-gated
IC	Inferior colliculus
IEI	Interevent interval
IHC	Inner hair cell
ILD	Interaural level difference
IQR	Interquartile range
ITD	Interaural time difference
KCC2	Potassium chloride cotransporter 2

*Abbreviations*

LOC	Lateral olivocochlear
LSO	Lateral superior olive
LTD	long-term depression
mIPSC	Miniature inhibitory postsynaptic current
MNTB	Medial nucleus of the trapezoid body
MSO	Medial superior olive
NGS	Normal goat serum
NKCC1	Sodium potassium chloride cotransporter 1
PBS	Phosphate-buffered saline
PBST	Phosphate-buffered saline containing 0.3% TritonX-100
PFA	Paraformaldehyde
PSC	Postsynaptic current
$R_{in}$	Input resistance
RMP	Resting membrane potential
SEM	Standard error of the mean
SGN	Spiral ganglion neurons
SOC	Superior olivary complex
SPN	Superior paraolivary nucleus
STD	Short-term depression
STP	Short-term plasticity
SV	Synaptic vesicle
$Tl^+$	Thallium
TTX	Tetrodotoxin
VGCC	Voltage-gated calcium channel

## 6 References

- Adam, T. J., Finlayson, P. G., & Schwarz, D. W. (2001). Membrane properties of principal neurons of the lateral superior olive. *J Neurophysiol*, *86*(2), 922-934.  
<https://doi.org/10.1152/jn.2001.86.2.922>
- Adam, T. J., Schwarz, D. W. F., & Finlayson, P. G. (1999). Firing properties of chopper and delay neurons in the lateral superior olive of the rat. *Experimental Brain Research*, *124*(4), 489-502. [https://doi.org/DOI 10.1007/s002210050645](https://doi.org/DOI%2010.1007/s002210050645)
- Amadeo, A., Coatti, A., Aracri, P., Ascagni, M., Iannantuoni, D., Modena, D., Carraresi, L., Brusco, S., Meneghini, S., Arcangeli, A., Pasini, M. E., & Becchetti, A. (2018). Postnatal Changes in K(+)/Cl(-) Cotransporter-2 Expression in the Forebrain of Mice Bearing a Mutant Nicotinic Subunit Linked to Sleep-Related Epilepsy. *Neuroscience*, *386*, 91-107.  
<https://doi.org/10.1016/j.neuroscience.2018.06.030>
- Arnold, T., Oestreicher, E., Ehrenberger, K., & Felix, D. (1998). GABA(A) receptor modulates the activity of inner hair cell afferents in guinea pig cochlea. *Hear Res*, *125*(1-2), 147-153.  
[https://doi.org/10.1016/s0378-5955\(98\)00144-0](https://doi.org/10.1016/s0378-5955(98)00144-0)
- Balakrishnan, V., Becker, M., Löhrike, S., Nothwang, H. G., Güresir, E., & Friauf, E. (2003). Expression and function of chloride transporters during development of inhibitory neurotransmission in the auditory brainstem. *Journal of Neuroscience*, *23*(10), 4134-4145.  
 <Go to ISI>://WOS:000183014300023
- Balkowiec, A., & Katz, D. M. (2002). Cellular mechanisms regulating activity-dependent release of native brain-derived neurotrophic factor from hippocampal neurons. *J Neurosci*, *22*(23), 10399-10407. <https://doi.org/10.1523/JNEUROSCI.22-23-10399.2002>
- Becker, M., Nothwang, H. G., & Friauf, E. (2003). Differential expression pattern of chloride transporters NCC, NKCC2, KCC1, KCC3, KCC4, and AE3 in the developing rat auditory brainstem. *Cell and Tissue Research*, *312*(2), 155-165. <https://doi.org/10.1007/s00441-003-0713-5>
- Ben-Ari, Y. (2002). Excitatory actions of GABA during development: The nature of the nurture. *Nature Reviews Neuroscience*, *3*(9), 728-739. <https://doi.org/10.1038/nrn920>

## References

- Ben-Ari, Y., Cherubini, E., Corradetti, R., & Gaiarsa, J. L. (1989). Giant Synaptic Potentials in Immature Rat Ca3 Hippocampal-Neurons. *Journal of Physiology-London*, 416, 303-325. <https://doi.org/DOI> 10.1113/jphysiol.1989.sp017762
- Ben-Ari, Y., Gaiarsa, J. L., Tyzio, R., & Khazipov, R. (2007). GABA: A pioneer transmitter that excites immature neurons and generates primitive oscillations. *Physiological Reviews*, 87(4), 1215-1284. <https://doi.org/10.1152/physrev.00017.2006>
- Ben-Ari, Y., Khalilov, I., Kahle, K. T., & Cherubini, E. (2012). The GABA excitatory/inhibitory shift in brain maturation and neurological disorders. *Neuroscientist*, 18(5), 467-486. <https://doi.org/10.1177/1073858412438697>
- Blaesse, P., Airaksinen, M. S., Rivera, C., & Kaila, K. (2009). Cation-chloride cotransporters and neuronal function. *Neuron*, 61(6), 820-838. <https://doi.org/10.1016/j.neuron.2009.03.003>
- Blaesse, P., Guillemin, I., Schindler, J., Schweizer, M., Delpire, E., Khiroug, L., Friauf, E., & Nothwang, H. G. (2006). Oligomerization of KCC2 correlates with development of inhibitory neurotransmission. *J Neurosci*, 26(41), 10407-10419. <https://doi.org/10.1523/JNEUROSCI.3257-06.2006>
- Bledsoe, S. C., Jr., Snead, C. R., Helfert, R. H., Prasad, V., Wenthold, R. J., & Altschuler, R. A. (1990). Immunocytochemical and lesion studies support the hypothesis that the projection from the medial nucleus of the trapezoid body to the lateral superior olive is glycinergic. *Brain Res*, 517(1-2), 189-194. [https://doi.org/10.1016/0006-8993\(90\)91025-c](https://doi.org/10.1016/0006-8993(90)91025-c)
- Boudreau, J. C., & Tsuchitani, C. (1968). Binaural interaction in the cat superior olive S segment. *J Neurophysiol*, 31(3), 442-454. <https://doi.org/10.1152/jn.1968.31.3.442>
- Bray, D. (1973). Branching patterns of individual sympathetic neurons in culture. *J Cell Biol*, 56(3), 702-712. <https://doi.org/10.1083/jcb.56.3.702>
- Brill, S. E., Janz, K., Singh, A., & Friauf, E. (2019). Considerable differences between auditory medulla, auditory midbrain, and hippocampal synapses during sustained high-frequency stimulation: Exceptional vesicle replenishment restricted to sound localization circuit. *Hear Res*, 381, 107771. <https://doi.org/10.1016/j.heares.2019.07.008>

## References

- Burdina, N., Liebsch, F., Macha, A., Gil, J. L. O., Frommelt, P., Rais, I., Basler, F., Popsel, S., & Schwarz, G. (2025). Phosphoinositide- and Collybistin-Dependent Synaptic Clustering of Gephyrin. *J Neurochem*, 169(8), e70169. <https://doi.org/10.1111/jnc.70169>
- Cant, N. B., & Casseday, J. H. (1986). Projections from the anteroventral cochlear nucleus to the lateral and medial superior olivary nuclei. *J Comp Neurol*, 247(4), 457-476. <https://doi.org/10.1002/cne.902470406>
- Case, D. T., & Gillespie, D. C. (2011). Pre- and postsynaptic properties of glutamatergic transmission in the immature inhibitory MNTB-LSO pathway. *J Neurophysiol*, 106(5), 2570-2579. <https://doi.org/10.1152/jn.00644.2010>
- Chamma, I., Chevy, Q., Poncer, J. C., & Levi, S. (2012). Role of the neuronal K-Cl co-transporter KCC2 in inhibitory and excitatory neurotransmission. *Front Cell Neurosci*, 6, 5. <https://doi.org/10.3389/fncel.2012.00005>
- Cherubini, E., Gaiarsa, J. L., & Ben-Ari, Y. (1991). GABA: an excitatory transmitter in early postnatal life. *Trends Neurosci*, 14(12), 515-519. [https://doi.org/10.1016/0166-2236\(91\)90003-d](https://doi.org/10.1016/0166-2236(91)90003-d)
- Ciuman, R. R. (2010). The efferent system or olivocochlear function bundle - fine regulator and protector of hearing perception. *Int J Biomed Sci*, 6(4), 276-288. <https://www.ncbi.nlm.nih.gov/pubmed/23675203>
- Clause, A., Kim, G., Sonntag, M., Weisz, C. J., Vetter, D. E., Rubsamen, R., & Kandler, K. (2014). The precise temporal pattern of prehearing spontaneous activity is necessary for tonotopic map refinement. *Neuron*, 82(4), 822-835. <https://doi.org/10.1016/j.neuron.2014.04.001>
- Clayton, G. H., Owens, G. C., Wolff, J. S., & Smith, R. L. (1998). Ontogeny of cation-Cl<sup>-</sup> cotransporter expression in rat neocortex. *Brain Res Dev Brain Res.*, 109(2), 281-292. [https://doi.org/10.1016/s0165-3806\(98\)00078-9](https://doi.org/10.1016/s0165-3806(98)00078-9).
- Cooper, A. P., & Gillespie, D. C. (2011). Synaptotagmins I and II in the developing rat auditory brainstem: Synaptotagmin I is transiently expressed in glutamate-releasing immature inhibitory terminals. *J Comp Neurol*, 519(12), 2417-2433. <https://doi.org/10.1002/cne.22634>
- Coull, J. A., Boudreau, D., Bachand, K., Prescott, S. A., Nault, F., Sik, A., De Koninck, P., & De Koninck, Y. (2003). Trans-synaptic shift in anion gradient in spinal lamina I neurons as a

## References

mechanism of neuropathic pain. *Nature*, 424(6951), 938-942.

<https://doi.org/10.1038/nature01868>

Darrow, K. N., Simons, E. J., Dodds, L., & Liberman, M. C. (2006). Dopaminergic innervation of the mouse inner ear: evidence for a separate cytochemical group of cochlear efferent fibers. *J Comp Neurol*, 498(3), 403-414. <https://doi.org/10.1002/cne.21050>

De Koninck, Y. (2007). Altered chloride homeostasis in neurological disorders: a new target. *Curr Opin Pharmacol*, 7(1), 93-99. <https://doi.org/10.1016/j.coph.2006.11.005>

Dent, E. W., Tang, F., & Kalil, K. (2003). Axon guidance by growth cones and branches: common cytoskeletal and signaling mechanisms. *Neuroscientist*, 9(5), 343-353. <https://doi.org/10.1177/1073858403252683>

Doleviczenyi, Z., Vizi, E. S., Gacsalyi, I., Pallagi, K., Volk, B., Harsing, L. G., Jr., Halmos, G., Lendvai, B., & Zelles, T. (2008). 5-HT<sub>6/7</sub> receptor antagonists facilitate dopamine release in the cochlea via a GABAergic disinhibitory mechanism. *Neurochem Res*, 33(11), 2364-2372. <https://doi.org/10.1007/s11064-008-9796-4>

Ehrlich, I., Lohrke, S., & Friauf, E. (1999). Shift from depolarizing to hyperpolarizing glycine action in rat auditory neurones is due to age-dependent Cl<sup>-</sup> regulation. *J Physiol*, 520 Pt 1(Pt 1), 121-137. <https://doi.org/10.1111/j.1469-7793.1999.00121.x>

Elgoyhen, A. B., Vetter, D. E., Katz, E., Rothlin, C. V., Heinemann, S. F., & Boulter, J. (2001).  $\alpha 10$ : a determinant of nicotinic cholinergic receptor function in mammalian vestibular and cochlear mechanosensory hair cells. *Proc Natl Acad Sci U S A*, 98(6), 3501-3506. <https://doi.org/10.1073/pnas.051622798>

Eybalin, M. (1993). Neurotransmitters and neuromodulators of the mammalian cochlea. *Physiol Rev*, 73(2), 309-373. <https://doi.org/10.1152/physrev.1993.73.2.309>

Flores, C. E., Nikonenko, I., Mendez, P., Fritschy, J. M., Tyagarajan, S. K., & Muller, D. (2015). Activity-dependent inhibitory synapse remodeling through gephyrin phosphorylation. *Proc Natl Acad Sci U S A*, 112(1), E65-72. <https://doi.org/10.1073/pnas.1411170112>

Franken, T. P., Bondy, B. J., Haimes, D. B., Goldwyn, J. H., Golding, N. L., Smith, P. H., & Joris, P. X. (2021). Glycinergic axonal inhibition subserves acute spatial sensitivity to sudden increases in sound intensity. *Elife*, 10. <https://doi.org/10.7554/eLife.62183>

#### References

- Fraser, S. D., Klaassen, R. V., Villmann, C., Smit, A. B., & Harvey, R. J. (2025). Milestone Review: Unlocking the Proteomics of Glycine Receptor Complexes. *J Neurochem*, 169(4), e70061. <https://doi.org/10.1111/jnc.70061>
- Friauf, E. (1993). Transient appearance of calbindin-D28k-positive neurons in the superior olivary complex of developing rats. *J Comp Neurol*, 334(1), 59-74. <https://doi.org/10.1002/cne.903340105>
- Friauf, E. (1994). Distribution of calcium-binding protein calbindin-D28k in the auditory system of adult and developing rats. *J Comp Neurol*, 349(2), 193-211. <https://doi.org/10.1002/cne.903490204>
- Friauf, E., Krächan, E. G., & Müller, N. I. C. (2019). Lateral Superior Olive: Organization, Development, and Plasticity In *The Oxford Handbook of the Auditory Brainstem* (pp. 329-394). <https://doi.org/10.1093/oxfordhb/9780190849061.013.10>
- Friauf, E., & Lohmann, C. (1999 ). Development of auditory brainstem circuitry. Activity-dependent and activity-independent processes. . *Cell Tissue Res.* , 297(2), 187-195. <https://doi.org/10.1007/s004410051346>.
- Friauf, E., Rust, M. B., Schulenburg, T., & Hirtz, J. J. (2011). Chloride cotransporters, chloride homeostasis, and synaptic inhibition in the developing auditory system. *Hear Res*, 279(1-2), 96-110. <https://doi.org/10.1016/j.heares.2011.05.012>
- Fuchs, P. A., & Lauer, A. M. (2019). Efferent Inhibition of the Cochlea. *Cold Spring Harb Perspect Med*, 9(5). <https://doi.org/10.1101/cshperspect.a033530>
- Fujino, K., Koyano, K., & Ohmori, H. (1997). Lateral and medial olivocochlear neurons have distinct electrophysiological properties in the rat brain slice. *J Neurophysiol*, 77(5), 2788-2804. <https://doi.org/10.1152/jn.1997.77.5.2788>
- Ganguly, K., Schinder, A. F., Wong, S. T., & Poo, M. (2001). GABA itself promotes the developmental switch of neuronal GABAergic responses from excitation to inhibition. *Cell*, 105(4), 521-532. [https://doi.org/10.1016/s0092-8674\(01\)00341-5](https://doi.org/10.1016/s0092-8674(01)00341-5)
- Gillespie, D. C., Kim, G., & Kandler, K. (2005). Inhibitory synapses in the developing auditory system are glutamatergic. *Nat Neurosci*, 8(3), 332-338. <https://doi.org/10.1038/nn1397>

## References

- Gjoni, E., Aguet, C., Sahlender, D. A., Knott, G., & Schneggenburger, R. (2018). Ultrastructural basis of strong unitary inhibition in a binaural neuron. *J Physiol*, 596(20), 4969-4982. <https://doi.org/10.1113/JP276015>
- Glendenning, K. K., Baker, B. N., Hutson, K. A., & Masterton, R. B. (1992). Acoustic chiasm V: inhibition and excitation in the ipsilateral and contralateral projections of LSO. *J Comp Neurol*, 319(1), 100-122. <https://doi.org/10.1002/cne.903190110>
- Glendenning, K. K., Brunso-Bechtold, J. K., Thompson, G. C., & Masterton, R. B. (1981). Ascending auditory afferents to the nuclei of the lateral lemniscus. *J Comp Neurol*, 197(4), 673-703. <https://doi.org/10.1002/cne.901970409>
- Goggi, J., Pullar, I. A., Carney, S. L., & Bradford, H. F. (2003). The control of [125I]BDNF release from striatal rat brain slices. *Brain Res*, 967(1-2), 201-209. [https://doi.org/10.1016/s0006-8993\(03\)02225-x](https://doi.org/10.1016/s0006-8993(03)02225-x)
- Goodman, C. S., & Shatz, C. J. (1993). Developmental mechanisms that generate precise patterns of neuronal connectivity. *Cell*, 72 Suppl, 77-98. [https://doi.org/10.1016/s0092-8674\(05\)80030-3](https://doi.org/10.1016/s0092-8674(05)80030-3)
- Goutman, J. D., Fuchs, P. A., & Glowatzki, E. (2005). Facilitating efferent inhibition of inner hair cells in the cochlea of the neonatal rat. *J Physiol*, 566(Pt 1), 49-59. <https://doi.org/10.1113/jphysiol.2005.087460>
- Grothe, B., Pecka, M., & McAlpine, D. (2010). Mechanisms of sound localization in mammals. *Physiol Rev*, 90(3), 983-1012. <https://doi.org/10.1152/physrev.00026.2009>
- Guinan, J. J., Jr. (2018). Olivocochlear efferents: Their action, effects, measurement and uses, and the impact of the new conception of cochlear mechanical responses. *Hear Res*, 362, 38-47. <https://doi.org/10.1016/j.heares.2017.12.012>
- Haragopal, H., Voytek, M. J., & Winters, B. D. (2025). Synaptic Drive onto Inhibitory and Excitatory Principal Neurons of the Mouse Lateral Superior Olive. *eNeuro*, 12(5). <https://doi.org/10.1523/ENEURO.0106-25.2025>
- Hartmann, A. M., Blaesse, P., Kranz, T., Wenz, M., Schindler, J., Kaila, K., Friauf, E., & Nothwang, H. G. (2009). Opposite effect of membrane raft perturbation on transport activity of KCC2

## References

and NKCC1. *J Neurochem*, 111(2), 321-331. <https://doi.org/10.1111/j.1471-4159.2009.06343.x>

Hatten, M. E. (1999). Central nervous system neuronal migration. *Annu Rev Neurosci*, 22, 511-539. <https://doi.org/10.1146/annurev.neuro.22.1.511>

Hirtz, J. J., Braun, N., Griesemer, D., Hannes, C., Janz, K., Lohrke, S., Muller, B., & Friauf, E. (2012). Synaptic refinement of an inhibitory topographic map in the auditory brainstem requires functional Cav1.3 calcium channels. *J Neurosci*, 32(42), 14602-14616. <https://doi.org/10.1523/JNEUROSCI.0765-12.2012>

Hong, H., Zeppenfeld, D., & Trussell, L. O. (2022). Electrical signaling in cochlear efferents is driven by an intrinsic neuronal oscillator. *Proc Natl Acad Sci U S A*, 119(44), e2209565119. <https://doi.org/10.1073/pnas.2209565119>

Huang, Z. J., Kirkwood, A., Pizzorusso, T., Porciatti, V., Morales, B., Bear, M. F., Maffei, L., & Tonegawa, S. (1999). BDNF regulates the maturation of inhibition and the critical period of plasticity in mouse visual cortex. *Cell*, 98(6), 739-755. [https://doi.org/10.1016/s0092-8674\(00\)81509-3](https://doi.org/10.1016/s0092-8674(00)81509-3)

Ji, J. L., Choi, C., Bope, C. E., Dengler, J. S., Moss, S. J., & Smalley, J. L. (2025). KCC2 inhibition and neuronal hyperexcitability promote extrinsic apoptosis dependent upon C1q. *Frontiers in Molecular Neuroscience*, 18. <https://doi.org/ARTN> 1645428

10.3389/fnmol.2025.1645428

Jiang, H. H., Xu, R., Nie, X., Su, Z., Xu, X., Pang, R., Zhou, Y., & Luo, F. (2024). Neurexins control the strength and precise timing of glycinergic inhibition in the auditory brainstem. *Elife*, 13. <https://doi.org/10.7554/eLife.94315>

Joris, P. X., & Yin, T. C. (1995). Envelope coding in the lateral superior olive. I. Sensitivity to interaural time differences. *J Neurophysiol*, 73(3), 1043-1062. <https://doi.org/10.1152/jn.1995.73.3.1043>

Kahle, K. T., Staley, K. J., Nahed, B. V., Gamba, G., Hebert, S. C., Lifton, R. P., & Mount, D. B. (2008). Roles of the cation-chloride cotransporters in neurological disease. *Nat Clin Pract Neurol*, 4(9), 490-503. <https://doi.org/10.1038/ncpneuro0883>

## References

- Kaila, K., Price, T. J., Payne, J. A., Puskarjov, M., & Voipio, J. (2014). Cation-chloride cotransporters in neuronal development, plasticity and disease. *Nat Rev Neurosci*, *15*(10), 637-654. <https://doi.org/10.1038/nrn3819>
- Kakazu, Y., Akaike, N., Komiyama, S., & Nabekura, J. (1999). Regulation of intracellular chloride by cotransporters in developing lateral superior olive neurons. *J Neurosci.*, *19*(8), 2843-2851. <https://doi.org/doi:10.1523/JNEUROSCI.19-08-02843.1999>.
- Kakazu, Y., Uchida, S., Nakagawa, T., Akaike, N., & Nabekura, J. (2000). Reversibility and cation selectivity of the K(+)-Cl(-) cotransport in rat central neurons. *J Neurophysiol*, *84*(1), 281-288. <https://doi.org/10.1152/jn.2000.84.1.281>
- Kandler, K., Clause, A., & Noh, J. (2009). Tonotopic reorganization of developing auditory brainstem circuits. *Nat Neurosci*, *12*(6), 711-717. <https://doi.org/10.1038/nn.2332>
- Kandler, K., & Friauf, E. (1993). Pre- and postnatal development of efferent connections of the cochlear nucleus in the rat. *J Comp Neurol*, *328*(2), 161-184. <https://doi.org/10.1002/cne.903280202>
- Kandler, K., & Friauf, E. (1995). Development of glycinergic and glutamatergic synaptic transmission in the auditory brainstem of perinatal rats. *J Neurosci*, *15*(9), 6890-6904. <https://doi.org/10.1523/15-10-06890.1995>.
- Kandler, K., & Gillespie, D. C. (2005). Developmental refinement of inhibitory sound-localization circuits. *Trends Neurosci*, *28*(6), 290-296. <https://doi.org/10.1016/j.tins.2005.04.007>
- Kanjhan, R., & Bellingham, M. C. (2013). Neurobiotin Electroporation for Combined Structural and Functional Analysis of Neurons in Developing Mouse Brain Slices. In *Stimulation and Inhibition of Neurons* (pp. 151-165). [https://doi.org/10.1007/978-1-62703-233-9\\_9](https://doi.org/10.1007/978-1-62703-233-9_9)
- Kapfer, C., Seidl, A. H., Schweizer, H., & Grothe, B. (2002). Experience-dependent refinement of inhibitory inputs to auditory coincidence-detector neurons. *Nat Neurosci*, *5*(3), 247-253. <https://doi.org/10.1038/nn810>
- Katz, E., Elgoyhen, A. B., Gomez-Casati, M. E., Knipper, M., Vetter, D. E., Fuchs, P. A., & Glowatzki, E. (2004). Developmental regulation of nicotinic synapses on cochlear inner hair cells. *J Neurosci*, *24*(36), 7814-7820. <https://doi.org/10.1523/JNEUROSCI.2102-04.2004>

## References

- Kelley, M. R., Cardarelli, R. A., Smalley, J. L., Ollerhead, T. A., Andrew, P. M., Brandon, N. J., Deeb, T. Z., & Moss, S. J. (2018). Locally Reducing KCC2 Activity in the Hippocampus is Sufficient to Induce Temporal Lobe Epilepsy. *EBioMedicine*, 32, 62-71.  
<https://doi.org/10.1016/j.ebiom.2018.05.029>
- Khazipov, R., Leinekugel, X., Khalilov, I., Gaiarsa, J. L., & Ben-Ari, Y. (1997). Synchronization of GABAergic interneuronal network in CA3 subfield of neonatal rat hippocampal slices. *J Physiol*, 498 ( Pt 3)(Pt 3), 763-772. <https://doi.org/10.1113/jphysiol.1997.sp021900>
- Kim, G., & Kandler, K. (2003). Elimination and strengthening of glycinergic/GABAergic connections during tonotopic map formation. *Nature Neuroscience*, 6(3), 282-290.  
<https://doi.org/10.1038/nn1015>
- Kim, G., & Kandler, K. (2010). Synaptic changes underlying the strengthening of GABA/glycinergic connections in the developing lateral superior olive. *Neuroscience*, 171(3), 924-933.  
<https://doi.org/10.1016/j.neuroscience.2010.09.054>
- Kontou, G., Josephine Ng, S. F., Cardarelli, R. A., Howden, J. H., Choi, C., Ren, Q., Rodriguez Santos, M. A., Bope, C. E., Dengler, J. S., Kelley, M. R., Davies, P. A., Kittler, J. T., Brandon, N. J., Moss, S. J., & Smalley, J. L. (2021). KCC2 is required for the survival of mature neurons but not for their development. *J Biol Chem*, 296, 100364.  
<https://doi.org/10.1016/j.jbc.2021.100364>
- Kotak, V. C., Korada, S., Schwartz, I. R., & Sanes, D. H. (1998). A developmental shift from GABAergic to glycinergic transmission in the central auditory system. *J Neurosci*, 18(12), 4646-4655. <https://doi.org/10.1523/JNEUROSCI.18-12-04646.1998>
- Koyama, S., Matsumoto, N., Murakami, N., Kubo, C., Nabekura, J., & Akaike, N. (2002). Role of presynaptic 5-HT<sub>1A</sub> and 5-HT<sub>3</sub> receptors in modulation of synaptic GABA transmission in dissociated rat basolateral amygdala neurons. *Life Sci*, 72(4-5), 375-387.  
[https://doi.org/10.1016/s0024-3205\(02\)02280-4](https://doi.org/10.1016/s0024-3205(02)02280-4)
- Kramer, F., Griesemer, D., Bakker, D., Brill, S., Franke, J., Frotscher, E., & Friauf, E. (2014). Inhibitory glycinergic neurotransmission in the mammalian auditory brainstem upon prolonged stimulation: short-term plasticity and synaptic reliability. *Front Neural Circuits*, 8, 14. <https://doi.org/10.3389/fncir.2014.00014>

#### References

- Kriegstein, A. R., & Noctor, S. C. (2004). Patterns of neuronal migration in the embryonic cortex. *Trends Neurosci*, 27(7), 392-399. <https://doi.org/10.1016/j.tins.2004.05.001>
- Kullmann, P. H., Ene, F. A., & Kandler, K. (2002). Glycinergic and GABAergic calcium responses in the developing lateral superior olive. *Eur J Neurosci*, 15(7), 1093-1104. <https://doi.org/10.1046/j.1460-9568.2002.01946.x>
- Kullmann, P. H., & Kandler, K. (2001). Glycinergic/GABAergic synapses in the lateral superior olive are excitatory in neonatal C57Bl/6J mice. *Brain Res Dev Brain Res*, 131(1-2), 143-147. [https://doi.org/10.1016/s0165-3806\(01\)00271-1](https://doi.org/10.1016/s0165-3806(01)00271-1)
- Le Prell, C. G., Dolan, D. F., Hughes, L. F., Altschuler, R. A., Shore, S. E., & Bledsoe, S. C., Jr. (2014). Disruption of lateral olivocochlear neurons with a dopaminergic neurotoxin depresses spontaneous auditory nerve activity. *Neurosci Lett*, 582, 54-58. <https://doi.org/10.1016/j.neulet.2014.08.040>
- Lee, K. G., & Rajakumar, N. (2022). Partial ablation of frontal cortical subplate leads to developmental abnormalities in KCC2 in the prefrontal cortex. *Mol Cell Neurosci*, 120, 103733. <https://doi.org/10.1016/j.mcn.2022.103733>
- Leinekugel, X., Medina, I., Khalilov, I., Ben-Ari, Y., & Khazipov, R. (1997). Ca<sup>2+</sup> oscillations mediated by the synergistic excitatory actions of GABA(A) and NMDA receptors in the neonatal hippocampus. *Neuron*, 18(2), 243-255. [https://doi.org/10.1016/s0896-6273\(00\)80265-2](https://doi.org/10.1016/s0896-6273(00)80265-2)
- Liberman, M. C. (1980). Efferent synapses in the inner hair cell area of the cat cochlea: an electron microscopic study of serial sections. *Hear Res*, 3(3), 189-204. [https://doi.org/10.1016/0378-5955\(80\)90046-5](https://doi.org/10.1016/0378-5955(80)90046-5)
- Liberman, M. C., Liberman, L. D., & Maison, S. F. (2014). Efferent Feedback Slows Cochlear Aging. *Journal of Neuroscience*, 34(13), 4599-4607. <https://doi.org/10.1523/Jneurosci.4923-13.2014>
- Lohmann, C., & Friauf, E. (1996). Distribution of the calcium-binding proteins parvalbumin and calretinin in the auditory brainstem of adult and developing rats. *J Comp Neurol*, 367(1), 90-109. [https://doi.org/10.1002/\(SICI\)1096-9861\(19960325\)367:1<90::AID-CNE7>3.0.CO;2-E](https://doi.org/10.1002/(SICI)1096-9861(19960325)367:1<90::AID-CNE7>3.0.CO;2-E)

## References

- Löhrke, S., Srinivasan, G., Oberhofer, M., Doncheva, E., & Friauf, E. (2005). Shift from depolarizing to hyperpolarizing glycine action occurs at different perinatal ages in superior olivary complex nuclei. *European Journal of Neuroscience*, 22(11), 2708-2722. <https://doi.org/10.1111/j.1460-9568.2005.04465.x>
- Macha, A., Liebsch, F., Bruckisch, E. H. W., Burdina, N., von Stulpnagel, I., Benting, K., Gunkel, M., Behrmann, E., & Schwarz, G. (2025). Gephyrin filaments represent the molecular basis of inhibitory postsynaptic densities. *Nat Commun*, 16(1), 8293. <https://doi.org/10.1038/s41467-025-63748-w>
- Maison, S. F., Usubuchi, H., & Liberman, M. C. (2013). Efferent feedback minimizes cochlear neuropathy from moderate noise exposure. *J Neurosci*, 33(13), 5542-5552. <https://doi.org/10.1523/JNEUROSCI.5027-12.2013>
- Maraslioglu-Sperber, A., Pizzi, E., Fisch, J., Kattler, K., Ritter, T., & Friauf, E. (2024). Molecular and functional profiling of cell diversity and identity in the lateral superior olive, an auditory brainstem center with ascending and descending projections. *Front Cell Neurosci*. <https://doi.org/10.3389/fncel.2024.1354520Maraslioglu-Sperber>
- Mayer, M. L., Westbrook, G. L., & Guthrie, P. B. (1984). Voltage-dependent block by Mg<sup>2+</sup> of NMDA responses in spinal cord neurones. *Nature*, 309(5965), 261-263. <https://doi.org/10.1038/309261a0>
- McMoneagle, E., Zhou, J., Zhang, S., Huang, W., Josiah, S. S., Ding, K., Wang, Y., & Zhang, J. (2024). Neuronal K(+)-Cl(-) cotransporter KCC2 as a promising drug target for epilepsy treatment. *Acta Pharmacol Sin*, 45(1), 1-22. <https://doi.org/10.1038/s41401-023-01149-9>
- Milenkovic, I., & Rubsamen, R. (2011). Development of the chloride homeostasis in the auditory brainstem. *Physiol Res*, 60(Suppl 1), S15-27. <https://doi.org/10.33549/physiolres.932178>
- Moore, M. J., & Caspary, D. M. (1983). Strychnine blocks binaural inhibition in lateral superior olivary neurons. *J Neurosci*, 3(1), 237-242. <https://doi.org/10.1523/JNEUROSCI.03-01-00237.1983>
- Mou, L., Dias, B. G., Gosnell, H., & Ressler, K. J. (2013). Gephyrin plays a key role in BDNF-dependent regulation of amygdala surface GABAARs. *Neuroscience*, 255, 33-44. <https://doi.org/10.1016/j.neuroscience.2013.09.051>

## References

- Mukherjee, J., Kretschmannova, K., Gouzer, G., Maric, H. M., Ramsden, S., Tretter, V., Harvey, K., Davies, P. A., Triller, A., Schindelin, H., & Moss, S. J. (2011). The residence time of GABA(A)Rs at inhibitory synapses is determined by direct binding of the receptor alpha1 subunit to gephyrin. *J Neurosci*, *31*(41), 14677-14687. <https://doi.org/10.1523/JNEUROSCI.2001-11.2011>
- Muniak, M. A., Mayko, Z. M., Ryugo, D. K., & Portfors, C. V. (2012). Preparation of an awake mouse for recording neural responses and injecting tracers. *J Vis Exp*(64). <https://doi.org/10.3791/3755>
- Nabekura, J., Katsurabayashi, S., Kakazu, Y., Shibata, S., Matsubara, A., Jinno, S., Mizoguchi, Y., Sasaki, A., & Ishibashi, H. (2004). Developmental switch from GABA to glycine release in single central synaptic terminals. *Nat Neurosci*, *7*(1), 17-23. <https://doi.org/10.1038/nn1170>
- Navawongse, R., & Voigt, H. F. (2009). Single neuron recordings in dorsal cochlear nucleus (DCN) of awake gerbil. *Hear Res*, *255*(1-2), 44-57. <https://doi.org/10.1016/j.heares.2009.05.004>
- Noh, J., Seal, R. P., Garver, J. A., Edwards, R. H., & Kandler, K. (2010). Glutamate co-release at GABA/glycinergic synapses is crucial for the refinement of an inhibitory map. *Nat Neurosci*, *13*(2), 232-238. <https://doi.org/10.1038/nn.2478>
- Nouvian, R., Eybalin, M., & Puel, J. L. (2015). Cochlear efferents in developing adult and pathological conditions. *Cell Tissue Res*, *361*(1), 301-309. <https://doi.org/10.1007/s00441-015-2158-z>
- Nowak, L., Bregestovski, P., Ascher, P., Herbet, A., & Prochiantz, A. (1984). Magnesium gates glutamate-activated channels in mouse central neurones. *Nature*, *307*(5950), 462-465. <https://doi.org/10.1038/307462a0>
- Owens, D. F., Boyce, L. H., Davis, M. B., & Kriegstein, A. R. (1996). Excitatory GABA responses in embryonic and neonatal cortical slices demonstrated by gramicidin perforated-patch recordings and calcium imaging. *J Neurosci*, *16*(20), 6414-6423. <https://doi.org/10.1523/JNEUROSCI.16-20-06414.1996>
- Owens, D. F., & Kriegstein, A. R. (2002). Is there more to GABA than synaptic inhibition? *Nat Rev Neurosci*, *3*(9), 715-727. <https://doi.org/10.1038/nrn919>

## References

- Park, H., & Poo, M. M. (2013). Neurotrophin regulation of neural circuit development and function. *Nat Rev Neurosci*, 14(1), 7-23. <https://doi.org/10.1038/nrn3379>
- Payne, J. A., Rivera, C., Voipio, J., & Kaila, K. (2003). Cation-chloride co-transporters in neuronal communication, development and trauma. *Trends Neurosci*, 26(4), 199-206. [https://doi.org/10.1016/S0166-2236\(03\)00068-7](https://doi.org/10.1016/S0166-2236(03)00068-7)
- Pozzi, D., Lignani, G., Ferrea, E., Contestabile, A., Paonessa, F., D'Alessandro, R., Lippiello, P., Boido, D., Fassio, A., Meldolesi, J., Valtorta, F., Benfenati, F., & Baldelli, P. (2013). REST/NRSF-mediated intrinsic homeostasis protects neuronal networks from hyperexcitability. *EMBO J*, 32(22), 2994-3007. <https://doi.org/10.1038/emboj.2013.231>
- Price, G. D., & Trussell, L. O. (2006). Estimate of the chloride concentration in a central glutamatergic terminal: a gramicidin perforated-patch study on the calyx of Held. *J Neurosci*, 26(44), 11432-11436. <https://doi.org/10.1523/JNEUROSCI.1660-06.2006>
- Radulovic, T., Rajaram, E., Ebbers, L., Pagella, S., Winklhofer, M., Kopp-Scheinflug, C., Nothwang, H. G., Milenkovic, I., & Hartmann, A. M. (2023). Serine 937 phosphorylation enhances KCC2 activity and strengthens synaptic inhibition. *Sci Rep*, 13(1), 21660. <https://doi.org/10.1038/s41598-023-48884-x>
- Rakic, P. (1972). Mode of cell migration to the superficial layers of fetal monkey neocortex. *J Comp Neurol*, 145(1), 61-83. <https://doi.org/10.1002/cne.901450105>
- Rico, B., Xu, B., & Reichardt, L. F. (2002). TrkB receptor signaling is required for establishment of GABAergic synapses in the cerebellum. *Nat Neurosci*, 5(3), 225-233. <https://doi.org/10.1038/nn808>
- Rietzel, H.-J., & Friauf, E. (1998). Neuron types in the rat lateral superior olive and developmental changes in the complexity of their dendritic arbors. *THE JOURNAL OF COMPARATIVE NEUROLOGY*, 390(1), 20-40. [https://doi.org/10.1002/\(sici\)1096-9861\(19980105\)390:1<20::Aid-cne3>3.0.Co;2-s](https://doi.org/10.1002/(sici)1096-9861(19980105)390:1<20::Aid-cne3>3.0.Co;2-s)
- Rivera, C., Voipio, J., Payne, J. A., Ruusuvuori, E., Lahtinen, H., Lamsa, K., Pirvola, U., Saarna, M., & Kaila, K. (1999). The K<sup>+</sup>/Cl<sup>-</sup> co-transporter KCC2 renders GABA hyperpolarizing during neuronal maturation. *Nature*, 397(6716), 251-255. <https://doi.org/10.1038/16697>

### References

- Rivera, C., Voipio, J., Thomas-Crusells, J., Li, H., Emri, Z., Sipila, S., Payne, J. A., Minichiello, L., Saarma, M., & Kaila, K. (2004). Mechanism of activity-dependent downregulation of the neuron-specific K-Cl cotransporter KCC2. *J Neurosci*, *24*(19), 4683-4691. <https://doi.org/10.1523/JNEUROSCI.5265-03.2004>
- Ruel, J., Nouvian, R., Gervais d'Aldin, C., Pujol, R., Eybalin, M., & Puel, J. L. (2001). Dopamine inhibition of auditory nerve activity in the adult mammalian cochlea. *Eur J Neurosci*, *14*(6), 977-986. <https://doi.org/10.1046/j.0953-816x.2001.01721.x>
- Sanes, D. H. (1990). An in vitro analysis of sound localization mechanisms in the gerbil lateral superior olive. *J Neurosci*, *10*(11), 3494-3506. <https://doi.org/10.1523/JNEUROSCI.10-11-03494.1990>
- Sanes, D. H., & Hafidi, A. (1996). Glycinergic transmission regulates dendrite size in organotypic culture. *Journal of Neurobiology*, *31*(4), 503-511. [https://doi.org/10.1002/\(sici\)1097-4695\(199612\)31:4<503::Aid-neu9>3.0.Co;2-d](https://doi.org/10.1002/(sici)1097-4695(199612)31:4<503::Aid-neu9>3.0.Co;2-d)
- Sanes, D. H., & Siverls, V. (1991). Development and specificity of inhibitory terminal arborizations in the central nervous system. *J Neurobiol*, *22*(8), 837-854. <https://doi.org/10.1002/neu.480220805>
- Sanes, D. H., Song, J., & Tyson, J. (1992). Refinement of dendritic arbors along the tonotopic axis of the gerbil lateral superior olive. *Brain Res Dev Brain Res.*, *67*(1), 47-55. [https://doi.org/10.1016/0165-3806\(92\)90024-q](https://doi.org/10.1016/0165-3806(92)90024-q)
- Sanes, D. H., & Takacs, C. (1993). Activity-dependent refinement of inhibitory connections. *Eur J Neurosci*, *5*(6), 570-574. <https://doi.org/10.1111/j.1460-9568.1993.tb00522.x>
- Sanes, J. R., & Yamagata, M. (2009). Many paths to synaptic specificity. *Annu Rev Cell Dev Biol*, *25*, 161-195. <https://doi.org/10.1146/annurev.cellbio.24.110707.175402>
- Sernagor, E., Chabrol, F., Bony, G., & Cancedda, L. (2010). GABAergic control of neurite outgrowth and remodeling during development and adult neurogenesis: general rules and differences in diverse systems. *Front Cell Neurosci*, *4*, 11. <https://doi.org/10.3389/fncel.2010.00011>

#### References

- Shibata, S., Kakazu, Y., Okabe, A., Fukuda, A., & Nabekura, J. (2004). Experience-dependent changes in intracellular Cl<sup>-</sup> regulation in developing auditory neurons. *Neurosci Res*, 48(2), 211-220. <https://doi.org/10.1016/j.neures.2003.10.011>
- Simmons, D. D. (2002). Development of the inner ear efferent system across vertebrate species. *J Neurobiol*, 53(2), 228-250. <https://doi.org/10.1002/neu.10130>
- Smith, P. H., Joris, P. X., & Yin, T. C. (1993). Projections of physiologically characterized spherical bushy cell axons from the cochlear nucleus of the cat: evidence for delay lines to the medial superior olive. *J Comp Neurol*, 331(2), 245-260. <https://doi.org/10.1002/cne.903310208>
- Sommer, I., Lingenhohl, K., & Friauf, E. (1993). Principal cells of the rat medial nucleus of the trapezoid body: an intracellular in vivo study of their physiology and morphology. *Exp Brain Res*, 95(2), 223-239. <https://doi.org/10.1007/BF00229781>
- Stein, V., Hermans-Borgmeyer, I., Jentsch, T. J., & Hubner, C. A. (2004). Expression of the KCl cotransporter KCC2 parallels neuronal maturation and the emergence of low intracellular chloride. *J Comp Neurol*, 468(1), 57-64. <https://doi.org/10.1002/cne.10983>
- Sterenborg, J. C., Pilati, N., Sheridan, C. J., Uchitel, O. D., Forsythe, I. D., & Barnes-Davies, M. (2010). Lateral olivocochlear (LOC) neurons of the mouse LSO receive excitatory and inhibitory synaptic inputs with slower kinetics than LSO principal neurons. *Hear Res*, 270(1-2), 119-126. <https://doi.org/10.1016/j.heares.2010.08.013>
- Tollin, D. J. (2003). The lateral superior olive: a functional role in sound source localization. *Neuroscientist*, 9(2), 127-143. <https://doi.org/10.1177/1073858403252228>
- Tollin, D. J., Koka, K., & Tsai, J. J. (2008). Interaural level difference discrimination thresholds for single neurons in the lateral superior olive. *J Neurosci*, 28(19), 4848-4860. <https://doi.org/10.1523/JNEUROSCI.5421-07.2008>
- Turrigiano, G. (2011). Too many cooks? Intrinsic and synaptic homeostatic mechanisms in cortical circuit refinement. *Annu Rev Neurosci*, 34, 89-103. <https://doi.org/10.1146/annurev-neuro-060909-153238>
- Turrigiano, G. (2012). Homeostatic synaptic plasticity: local and global mechanisms for stabilizing neuronal function. *Cold Spring Harb Perspect Biol*, 4(1), a005736. <https://doi.org/10.1101/cshperspect.a005736>

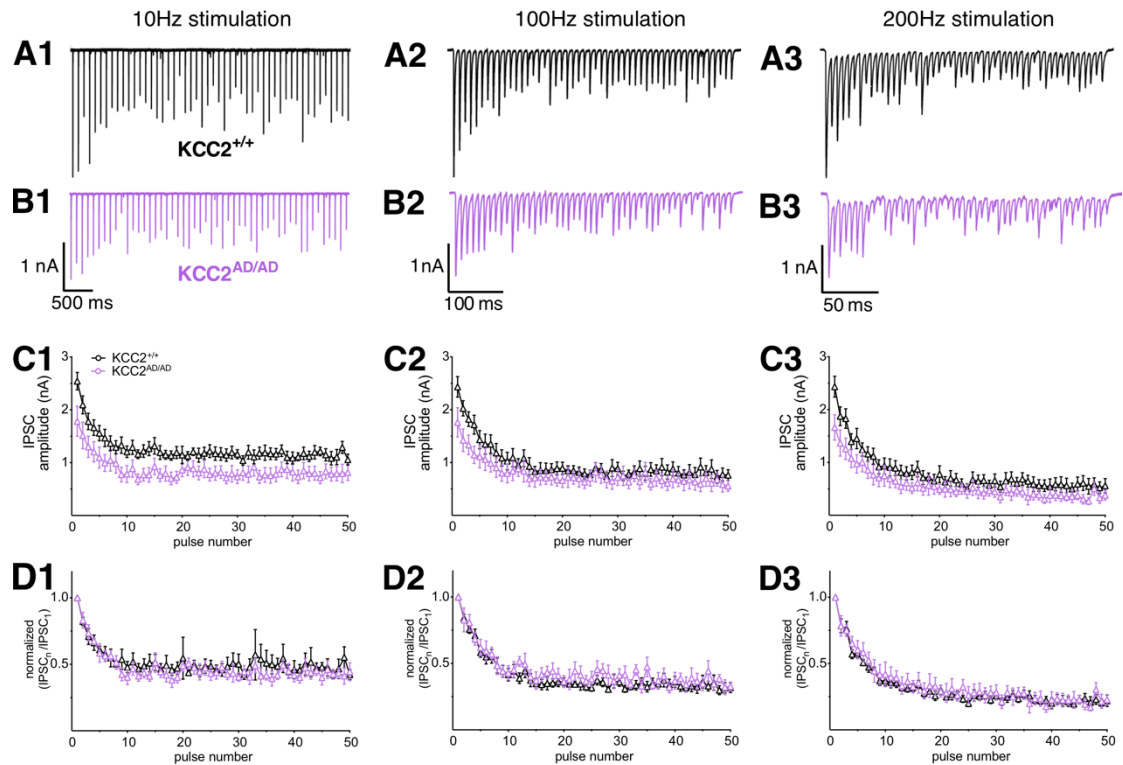
## References

- Tyagarajan, S. K., & Fritschy, J. M. (2014). Gephyrin: a master regulator of neuronal function? *Nat Rev Neurosci*, *15*(3), 141-156. <https://doi.org/10.1038/nrn3670>
- Tyzio, R., Nardou, R., Ferrari, D. C., Tsintsadze, T., Shahrokhi, A., Eftekhari, S., Khalilov, I., Tsintsadze, V., Brouchoud, C., Chazal, G., Lemonnier, E., Lozovaya, N., Burnashev, N., & Ben-Ari, Y. (2014). Oxytocin-mediated GABA inhibition during delivery attenuates autism pathogenesis in rodent offspring. *Science*, *343*(6171), 675-679. <https://doi.org/10.1126/science.1247190>
- Tyzio, R., Represa, A., Jorquera, I., Ben-Ari, Y., Gozlan, H., & Aniksztejn, L. (1999). The establishment of GABAergic and glutamatergic synapses on CA1 pyramidal neurons is sequential and correlates with the development of the apical dendrite. *J Neurosci*, *19*(23), 10372-10382. <https://doi.org/10.1523/JNEUROSCI.19-23-10372.1999>
- Vale, C., Caminos, E., Martinez-Galan, J. R., & Juiz, J. M. (2005). Expression and developmental regulation of the K<sup>+</sup>-Cl<sup>-</sup> cotransporter KCC2 in the cochlear nucleus. *Hear Res*, *206*(1-2), 107-115. <https://doi.org/10.1016/j.heares.2005.03.012>
- Vetter, D. E., & Mugnaini, E. (1992). Distribution and dendritic features of three groups of rat olivocochlear neurons. A study with two retrograde cholera toxin tracers. *Anat Embryol (Berl)*, *185*(1), 1-16. <https://doi.org/10.1007/BF00213596>
- Waites, C. L., Craig, A. M., & Garner, C. C. (2005). Mechanisms of vertebrate synaptogenesis. *Annu Rev Neurosci*, *28*, 251-274. <https://doi.org/10.1146/annurev.neuro.27.070203.144336>
- Walcher, J., Hassfurth, B., Grothe, B., & Koch, U. (2011). Comparative posthearing development of inhibitory inputs to the lateral superior olive in gerbils and mice. *J Neurophysiol*, *106*(3), 1443-1453. <https://doi.org/10.1152/jn.01087.2010>
- Warr, W. B., & Guinan, J. J. J. (1979). Efferent innervation of the organ of corti: two separate systems. *Brain Res*, *173*(1), 152-155. [https://doi.org/10.1016/0006-8993\(79\)91104-1](https://doi.org/10.1016/0006-8993(79)91104-1)
- Weingarten, D. J., Sebastian, E., Winkelhoff, J., Patschull-Keiner, N., Fischer, A. U., Wadle, S. L., Friauf, E., & Hirtz, J. J. (2023). An inhibitory glycinergic projection from the cochlear nucleus to the lateral superior olive. *Front Neural Circuits*, *17*, 1307283. <https://doi.org/10.3389/fncir.2023.1307283>

#### References

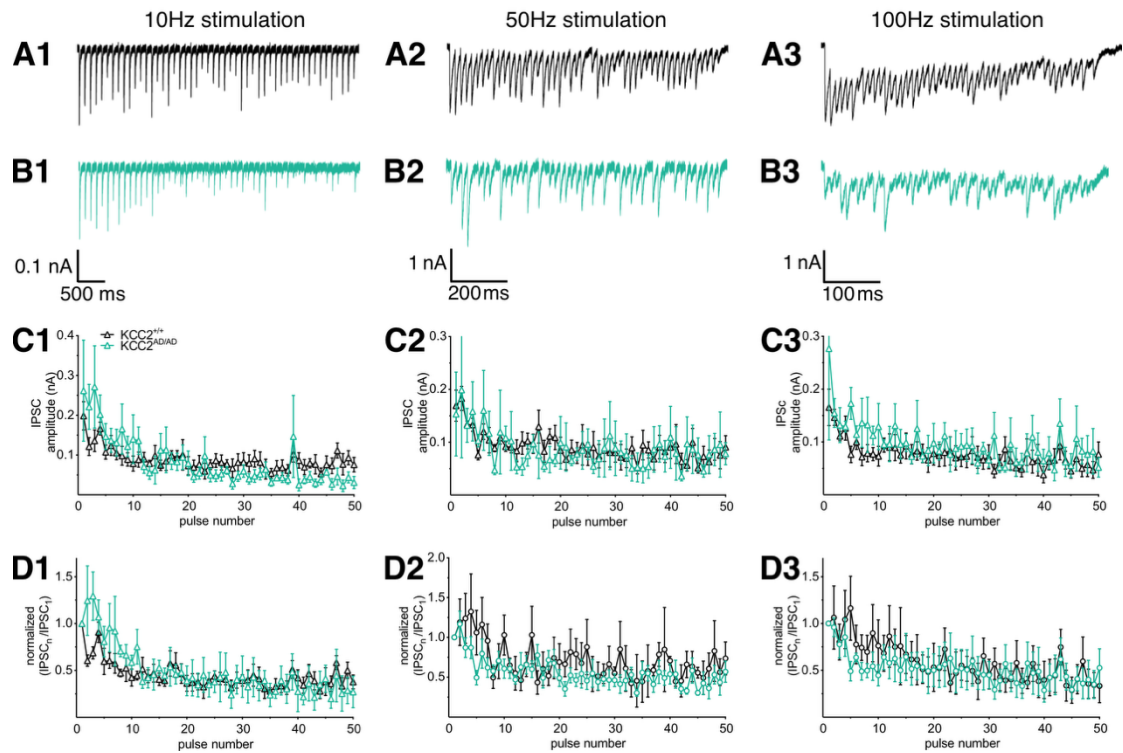
- Werthat, F., Alexandrova, O., Grothe, B., & Koch, U. (2008). Experience-dependent refinement of the inhibitory axons projecting to the medial superior olive. *Dev Neurobiol*, 68(13), 1454-1462. <https://doi.org/10.1002/dneu.20660>
- Wiessler, A. L., Zheng, F., Werner, C., Habib, M., Tuzun, E., Alzheimer, C., Sommer, C., & Villmann, C. (2025). Impaired Presynaptic Function Contributes Significantly to the Pathology of Glycine Receptor Autoantibodies. *Neurol Neuroimmunol Neuroinflamm*, 12(2), e200364. <https://doi.org/10.1212/NXI.0000000000200364>
- Williams, I. R., Filimontseva, A., Connelly, C. J., & Ryugo, D. K. (2022). The lateral superior olive in the mouse: Two systems of projecting neurons. *Front Neural Circuits*, 16, 1038500. <https://doi.org/10.3389/fncir.2022.1038500>
- Wu, J. S., Yi, E., Manca, M., Javaid, H., Lauer, A. M., & Glowatzki, E. (2020). Sound exposure dynamically induces dopamine synthesis in cholinergic LOC efferents for feedback to auditory nerve fibers. *Elife*, 9. <https://doi.org/10.7554/eLife.52419>
- Yamada, J., Okabe, A., Toyoda, H., Kilb, W., Luhmann, H. J., & Fukuda, A. (2004). Cl<sup>-</sup> uptake promoting depolarizing GABA actions in immature rat neocortical neurones is mediated by NKCC1. *J Physiol*, 557(Pt 3), 829-841. <https://doi.org/10.1113/jphysiol.2004.062471>

## 7 Supplementary information

Figure S.1 Normal short-term plasticity in LSO neurons of  $KCC2^{AD/AD}$  mice at P20.

**(A, B)** Representative eIPSC trains from  $KCC2^{+/+}$  (**A**, black) and  $KCC2^{AD/AD}$  (**B**, purple) neurons in response to 50 stimuli delivered at 10 Hz (left), 100Hz (middle) and 200Hz (right). **(C)** Quantification of eIPSC peak amplitudes plotted against pulse number for 10 Hz (**C1**), 100 Hz (**C2**), and 200 Hz (**C3**) stimulation. The current amplitude is lower in  $KCC2^{AD/AD}$  group across tested frequencies. **(D)** Normalized synaptic depression profile ( $IPSC_n/IPSC_1$ ) for the frequencies shown in **C**. The degree of depression and steady-state levels are indistinguishable between genotypes at 10 Hz (**D1**), 100 Hz (**D2**), and 200 Hz (**D3**). Error bar in **C** and **D** show SEM.

**Figure S.2 Normal short-term plasticity in LOC neurons of  $KCC2^{AD/AD}$  mice at P20.**



(A, B) Representative eIPSC from LOC neurons in  $KCC2^{+/+}$  (A, black) and  $KCC2^{AD/AD}$  (B, green) mice in response to stimuli delivered at 10 Hz (left), 50Hz (middle) and 100Hz (right). Both genotypes exhibited characteristic short-term depression. (C) eIPSC amplitudes recorded at P20 and plotted against pulse number for different stimulus frequencies. (D) Normalized synaptic depression profile (IPSC<sub>n</sub>/IPSC<sub>1</sub>). Depression and steady-state levels are similar between genotypes and across stimulus frequencies. The error bar in C and D shows SEM.

**Table S.1 Intrinsic membrane properties of LSO neurons.**

	LSO	Age	Mean $\pm$ SEM		P values	post-hoc comparison	
			$KCC2^{+/+}$	$KCC2^{AD/AD}$			
Figure 3.3	AP properties	P14	99.48 $\pm$ 14.69	126.56 $\pm$ 19.95	$p = 0.42$	$p = 0.57$	P14 vs P20: $KCC2^{+/+}$ $p = 0.66$ $KCC2^{AD/AD}$ $p = 0.60$
		P20	122.9 $\pm$ 13.5	103.42 $\pm$ 9.52		$p = 0.74$	
	Latency stim onset-AP peak (ms)	P14	3.98 $\pm$ 0.78	5.63 $\pm$ 1.6	$p = 0.46$	$p = 0.90$	P14 vs P20: $KCC2^{+/+}$ $p = 0.92$ $KCC2^{AD/AD}$ $p = 0.51$
		P20	5.01 $\pm$ 1.57	2.78 $\pm$ 0.33		$p = 0.52$	
		P14	3.18 $\pm$ 0.79	3.31 $\pm$ 1.38	$p = 0.95$	$p = 0.95$	P14 vs P20:

Supplementary information

	tau (ms)	P20	3.7 ± 0.67	2.43 ± 0.61	0.76	p = 0.52	KCC2 <sup>+/+</sup> p = 0.76 KCC2 <sup>AD/AD</sup> p = 0.75
	rheobase (pA)	P14	318.06 ± 39.11	245.48 ± 50.32	p = 0.08	p = 0.73	P14 vs P20: KCC2 <sup>+/+</sup> p = 0.07 KCC2 <sup>AD/AD</sup> p = 0.93
P20		186.11 ± 28.49	281.25 ± 32.34	p = 0.27			
Figure 3.4	AP threshold (mV)	P14	-53.78 ± 1.85	-53.24 ± 2.16	p = 0.18	p = 0.93	P14 vs P20: KCC2 <sup>+/+</sup> p = 0.31 KCC2 <sup>AD/AD</sup> p = 0.81
		P20	-58.22 ± 1.76	-55.83 ± 2.3		p = 0.66	
	AP amplitude threshold-peak (mV)	P14	54.15 ± 4.5	58.77 ± 3.94	p = 0.41	p = 0.97	P14 vs P20: KCC2 <sup>+/+</sup> p = 0.75 KCC2 <sup>AD/AD</sup> p = 0.50
		P20	49.39 ± 2.7	49.69 ± 2.98		p > 0.99	
	AP amplitude baseline-peak (mV)	P14	77.79 ± 4.2	80.89 ± 4.5	p = 0.04	p = 0.95	P14 vs P20: KCC2 <sup>+/+</sup> p = 0.13 KCC2 <sup>AD/AD</sup> p = 0.21
		P20	68.43 ± 2.9	70.36 ± 1.86		p > 0.99	
	half width (ms)	P14	0.3 ± 0.01	0.31 ± 0.02	p = 0.61	p > 0.99	P14 vs P20: KCC2 <sup>+/+</sup> p = 0.76 KCC2 <sup>AD/AD</sup> p = 0.82
		P20	0.28 ± 0.02	0.28 ± 0.01		p > 0.99	
	sag (mV)	P14	9.72 ± 1.04	12.82 ± 2.08	p = 0.01	p = 0.26	P14 vs P20: KCC2 <sup>+/+</sup> p = 0.68 KCC2 <sup>AD/AD</sup> p = 0.009
		P20	7.74 ± 1.53	5.27 ± 1.24		p = 0.81	
	max AP rising slope (mV/ms)	P14	371.76 ± 41.35	383.58 ± 36.34	p = 0.52	p > 0.99	P14 vs P20: KCC2 <sup>+/+</sup> p = 0.76 KCC2 <sup>AD/AD</sup> p = 0.67
		P20	329.12 ± 26.31	325.58 ± 26.8		p = 0.98	
max AP decaying slope (mV/ms)	P14	-231.64 ± 27.29	-240.94 ± 25.52	p > 0.99	p > 0.99	P14 vs P20: KCC2 <sup>+/+</sup> p > 0.99 KCC2 <sup>AD/AD</sup> p > 0.99	
	P20	-228.88 ± 22.97	-234.79 ± 22.15		p > 0.99		
AHP amplitude (mV)	P14	-14.31 ± 1.33	-16.51 ± 2.23	p = 0.82	p = 0.85	P14 vs P20: KCC2 <sup>+/+</sup> p > 0.99 KCC2 <sup>AD/AD</sup> p = 0.83	
	P20	-14.25 ± 1.4	-14.31 ± 1.75		p > 0.99		

Data are presented as mean ± SEM. P-values were calculated using 2-way ANOVA with Tukey's multiple comparison post-hoc tests. Significant P-values are marked in yellow. P14: KCC2<sup>+/+</sup> n = 12, KCC2<sup>AD/AD</sup> n = 7; P20: KCC2<sup>+/+</sup> n = 12, KCC2<sup>AD/AD</sup> n = 8.

**Table S.2 mIPSC parameters of LSO neurons.**

	LSO mIPSC	Age	Mean $\pm$ SEM		P values	post-hoc comparison	
			KCC2 <sup>+/+</sup>	KCC2 <sup>AD/AD</sup>			
Figure 3.5, 3.6, 3.7	amplitude (pA)	P14	92.54 $\pm$ 7.16	74.33 $\pm$ 6.54	p < 0.001	p = 0.21	P14 vs P20: KCC2 <sup>+/+</sup> p = 0.02 KCC2 <sup>AD/AD</sup> p = 0.87
		P20	125.2 $\pm$ 5.82	83.41 $\pm$ 7.49		p < 0.001	
	tau rise (ms)	P14	0.23 $\pm$ 0.02	0.26 $\pm$ 0.02	p = 0.04	p = 0.45	P14 vs P20: KCC2 <sup>+/+</sup> p = 0.50 KCC2 <sup>AD/AD</sup> p = 0.22
		P20	0.2 $\pm$ 0	0.23 $\pm$ 0.02		p = 0.68	
	tau decay (ms)	P14	1.6 $\pm$ 0.18	2.11 $\pm$ 0.22	p = 0.4	p = 0.45	P14 vs P20: KCC2 <sup>+/+</sup> p > 0.99 KCC2 <sup>AD/AD</sup> p = 0.59
		P20	1.7 $\pm$ 0.1	1.81 $\pm$ 0.23		p > 0.99	
	frequency (Hz)	P14	6.83 $\pm$ 0.93	4.5 $\pm$ 0.66	p = 0.13	p = 0.24	P14 vs P20: KCC2 <sup>+/+</sup> p = 0.83 KCC2 <sup>AD/AD</sup> p = 0.99
		P20	5.83 $\pm$ 0.64	4.3 $\pm$ 0.59		p = 0.49	

Data are presented as mean  $\pm$  SEM. P-values were calculated using 2-way ANOVA with Tukey's multiple comparison post-hoc tests. Significant P-values are marked in yellow. P14: KCC2<sup>+/+</sup> n = 10, KCC2<sup>AD/AD</sup> n = 13; P20: KCC2<sup>+/+</sup> n = 11, KCC2<sup>AD/AD</sup> n = 12.

**Table S.3 eIPSC parameters of LSO neurons**

	LSO eIPSC	Age	Mean $\pm$ SEM		P Values	post-hoc comparison	
			KCC2 <sup>+/+</sup>	KCC2 <sup>AD/AD</sup>			
Figure 3.8	amplitude (nA)	P14	2.16 $\pm$ 0.27	1 $\pm$ 0.13	p < 0.001	p = 0.003	P14 vs P20: KCC2 <sup>+/+</sup> p = 0.38 KCC2 <sup>AD/AD</sup> p = 0.10
		P20	2.7 $\pm$ 0.18	1.73 $\pm$ 0.21		p = 0.03	
	tau rise (ms)	P14	0.35 $\pm$ 0.02	0.34 $\pm$ 0.02	p = 0.04	p > 0.99	P14 vs P20: KCC2 <sup>+/+</sup> p = 0.13 KCC2 <sup>AD/AD</sup> p = 0.24
		P20	0.28 $\pm$ 0.01	0.28 $\pm$ 0.02		p > 0.99	
	tau decay (ms)	P14	3.76 $\pm$ 0.2	3.41 $\pm$ 0.35	p < 0.001	p = 0.68	P14 vs P20: KCC2 <sup>+/+</sup> p = 0.002
		P20	2.28 $\pm$ 0.21	2.3 $\pm$ 0.25		p > 0.99	

Supplementary information

							KCC2 <sup>AD/AD</sup> p = 0.08
--	--	--	--	--	--	--	--------------------------------

Data are presented as mean  $\pm$  SEM. P-values were calculated using 2-way ANOVA with Tukey's multiple comparison post-hoc tests. Significant P-values are marked in yellow. P14: KCC2<sup>+/+</sup> n = 12, KCC2<sup>AD/AD</sup> n = 14; P20: KCC2<sup>+/+</sup> n = 14, KCC2<sup>AD/AD</sup> n = 11.

**Table S.4 eIPSC amplitude of LSO neurons (P14) at 10Hz, 100Hz and 200Hz stimulating frequencies.**

	Pulse	LSO eIPSCs amplitude Mean $\pm$ SEM (nA)					
		P14 (10Hz)		P14 (100Hz)		P14 (200Hz)	
		KCC2 <sup>+/+</sup>	KCC2 <sup>AD/AD</sup>	KCC2 <sup>+/+</sup>	KCC2 <sup>AD/AD</sup>	KCC2 <sup>+/+</sup>	KCC2 <sup>AD/AD</sup>
Figure 3.9 KCC2 <sup>+/+</sup> n = 8, KCC2 <sup>AD/AD</sup> n = 11	1	2.01 $\pm$ 0.24	1.06 $\pm$ 0.14	1.89 $\pm$ 0.23	0.98 $\pm$ 0.15	1.72 $\pm$ 0.21	0.94 $\pm$ 0.16
	2	1.76 $\pm$ 0.21	0.85 $\pm$ 0.1	1.78 $\pm$ 0.19	0.87 $\pm$ 0.13	1.37 $\pm$ 0.15	0.73 $\pm$ 0.15
	3	1.52 $\pm$ 0.22	0.75 $\pm$ 0.09	1.5 $\pm$ 0.17	0.84 $\pm$ 0.11	1.19 $\pm$ 0.16	0.75 $\pm$ 0.15
	4	1.4 $\pm$ 0.17	0.71 $\pm$ 0.1	1.46 $\pm$ 0.16	0.72 $\pm$ 0.11	1.1 $\pm$ 0.15	0.66 $\pm$ 0.14
	5	1.35 $\pm$ 0.16	0.69 $\pm$ 0.08	1.3 $\pm$ 0.17	0.63 $\pm$ 0.09	1.02 $\pm$ 0.16	0.57 $\pm$ 0.13
	6	1.34 $\pm$ 0.14	0.65 $\pm$ 0.08	1.24 $\pm$ 0.16	0.64 $\pm$ 0.1	0.71 $\pm$ 0.19	0.58 $\pm$ 0.12
	7	1.25 $\pm$ 0.15	0.55 $\pm$ 0.07	1.19 $\pm$ 0.15	0.58 $\pm$ 0.1	0.97 $\pm$ 0.13	0.54 $\pm$ 0.11
	8	1.11 $\pm$ 0.15	0.57 $\pm$ 0.07	1.17 $\pm$ 0.2	0.61 $\pm$ 0.1	0.92 $\pm$ 0.14	0.47 $\pm$ 0.11
	9	1.18 $\pm$ 0.16	0.56 $\pm$ 0.09	1.09 $\pm$ 0.13	0.61 $\pm$ 0.12	0.82 $\pm$ 0.22	0.44 $\pm$ 0.11
	10	1.05 $\pm$ 0.14	0.52 $\pm$ 0.07	1.08 $\pm$ 0.14	0.55 $\pm$ 0.09	0.81 $\pm$ 0.11	0.47 $\pm$ 0.09
	11	1.15 $\pm$ 0.13	0.57 $\pm$ 0.07	1.07 $\pm$ 0.15	0.53 $\pm$ 0.08	0.65 $\pm$ 0.1	0.36 $\pm$ 0.08
	12	1.14 $\pm$ 0.14	0.54 $\pm$ 0.07	0.93 $\pm$ 0.12	0.47 $\pm$ 0.08	0.61 $\pm$ 0.18	0.41 $\pm$ 0.1
	13	1.13 $\pm$ 0.12	0.51 $\pm$ 0.08	1 $\pm$ 0.15	0.45 $\pm$ 0.07	0.77 $\pm$ 0.11	0.39 $\pm$ 0.08
	14	1.1 $\pm$ 0.12	0.48 $\pm$ 0.07	0.97 $\pm$ 0.13	0.55 $\pm$ 0.09	0.57 $\pm$ 0.11	0.45 $\pm$ 0.11
	15	1.09 $\pm$ 0.15	0.48 $\pm$ 0.05	1 $\pm$ 0.1	0.44 $\pm$ 0.07	0.71 $\pm$ 0.11	0.44 $\pm$ 0.11
	16	0.97 $\pm$ 0.12	0.53 $\pm$ 0.06	0.84 $\pm$ 0.14	0.48 $\pm$ 0.08	0.43 $\pm$ 0.09	0.32 $\pm$ 0.07
	17	1.1 $\pm$ 0.14	0.42 $\pm$ 0.04	0.84 $\pm$ 0.13	0.52 $\pm$ 0.1	0.68 $\pm$ 0.11	0.37 $\pm$ 0.08
	18	1.14 $\pm$ 0.14	0.53 $\pm$ 0.09	0.88 $\pm$ 0.11	0.51 $\pm$ 0.08	0.53 $\pm$ 0.13	0.29 $\pm$ 0.07
	19	1.03 $\pm$ 0.13	0.5 $\pm$ 0.06	0.79 $\pm$ 0.09	0.47 $\pm$ 0.08	0.54 $\pm$ 0.11	0.35 $\pm$ 0.08

Supplementary information

20	1.1 ± 0.14	0.54 ± 0.1	0.93 ± 0.14	0.43 ± 0.09	0.46 ± 0.11	0.3 ± 0.07
21	1.05 ± 0.12	0.47 ± 0.07	0.88 ± 0.11	0.44 ± 0.06	0.56 ± 0.08	0.32 ± 0.08
22	0.92 ± 0.12	0.52 ± 0.06	0.85 ± 0.09	0.46 ± 0.08	0.47 ± 0.13	0.23 ± 0.06
23	1.08 ± 0.14	0.51 ± 0.06	0.79 ± 0.11	0.44 ± 0.06	0.52 ± 0.1	0.3 ± 0.07
24	0.93 ± 0.13	0.51 ± 0.09	0.89 ± 0.13	0.5 ± 0.08	0.37 ± 0.11	0.24 ± 0.06
25	0.98 ± 0.11	0.52 ± 0.06	0.86 ± 0.13	0.46 ± 0.08	0.57 ± 0.1	0.37 ± 0.09
26	1.06 ± 0.12	0.48 ± 0.05	0.96 ± 0.12	0.46 ± 0.08	0.38 ± 0.11	0.34 ± 0.08
27	1.02 ± 0.14	0.43 ± 0.07	0.78 ± 0.12	0.47 ± 0.08	0.52 ± 0.08	0.27 ± 0.06
28	1.06 ± 0.14	0.51 ± 0.07	0.84 ± 0.13	0.41 ± 0.06	0.44 ± 0.14	0.31 ± 0.08
29	1 ± 0.13	0.48 ± 0.07	0.84 ± 0.12	0.44 ± 0.08	0.5 ± 0.08	0.27 ± 0.06
30	1.04 ± 0.13	0.48 ± 0.07	0.83 ± 0.11	0.44 ± 0.08	0.4 ± 0.09	0.32 ± 0.08
31	0.97 ± 0.11	0.47 ± 0.06	0.66 ± 0.11	0.43 ± 0.07	0.48 ± 0.07	0.21 ± 0.05
32	1.04 ± 0.15	0.54 ± 0.09	0.86 ± 0.13	0.46 ± 0.08	0.42 ± 0.11	0.29 ± 0.07
33	1 ± 0.12	0.52 ± 0.08	0.88 ± 0.12	0.46 ± 0.1	0.47 ± 0.08	0.25 ± 0.06
34	0.92 ± 0.11	0.47 ± 0.06	0.75 ± 0.14	0.45 ± 0.07	0.41 ± 0.09	0.22 ± 0.04
35	1.01 ± 0.12	0.45 ± 0.07	0.84 ± 0.11	0.41 ± 0.07	0.5 ± 0.08	0.27 ± 0.06
36	1.03 ± 0.12	0.44 ± 0.05	0.77 ± 0.11	0.48 ± 0.09	0.38 ± 0.1	0.28 ± 0.06
37	0.99 ± 0.14	0.47 ± 0.05	0.85 ± 0.11	0.43 ± 0.08	0.51 ± 0.11	0.23 ± 0.06
38	0.99 ± 0.14	0.51 ± 0.08	0.77 ± 0.1	0.42 ± 0.07	0.34 ± 0.06	0.27 ± 0.06
39	0.95 ± 0.12	0.42 ± 0.05	0.81 ± 0.14	0.4 ± 0.06	0.38 ± 0.08	0.25 ± 0.07
40	0.95 ± 0.12	0.44 ± 0.06	0.73 ± 0.09	0.42 ± 0.08	0.47 ± 0.07	0.27 ± 0.09
41	0.89 ± 0.09	0.44 ± 0.07	0.75 ± 0.13	0.48 ± 0.09	0.42 ± 0.09	0.25 ± 0.05
42	0.97 ± 0.15	0.47 ± 0.07	0.71 ± 0.12	0.42 ± 0.09	0.42 ± 0.08	0.29 ± 0.06
43	1 ± 0.11	0.46 ± 0.07	0.72 ± 0.1	0.45 ± 0.08	0.38 ± 0.08	0.22 ± 0.06
44	1.02 ± 0.14	0.4 ± 0.04	0.78 ± 0.08	0.43 ± 0.07	0.42 ± 0.07	0.32 ± 0.08
45	0.91 ± 0.12	0.47 ± 0.07	0.74 ± 0.11	0.42 ± 0.07	0.47 ± 0.12	0.24 ± 0.06
46	1.03 ± 0.13	0.45 ± 0.06	0.66 ± 0.12	0.37 ± 0.07	0.42 ± 0.1	0.25 ± 0.06
47	0.95 ± 0.13	0.45 ± 0.06	0.7 ± 0.09	0.39 ± 0.08	0.35 ± 0.07	0.28 ± 0.09
48	0.91 ± 0.09	0.45 ± 0.06	0.67 ± 0.13	0.42 ± 0.08	0.4 ± 0.08	0.21 ± 0.04
49	0.88 ± 0.12	0.43 ± 0.07	0.7 ± 0.12	0.42 ± 0.09	0.37 ± 0.13	0.25 ± 0.05
50	0.95 ± 0.14	0.46 ± 0.07	0.75 ± 0.1	0.38 ± 0.1	0.42 ± 0.1	0.24 ± 0.06

Data are presented as mean ± SEM.

**Table S.5 eIPSC amplitude of LSO neurons (P20) at 10Hz, 100Hz and 200Hz stimulating frequencies.**

	Pulse	LSO eIPSCs amplitude Mean $\pm$ SEM (nA)					
		P20 (10Hz)		P20 (100Hz)		P20 (200Hz)	
		KCC2 <sup>+/+</sup>	KCC2 <sup>AD/AD</sup>	KCC2 <sup>+/+</sup>	KCC2 <sup>AD/AD</sup>	KCC2 <sup>+/+</sup>	KCC2 <sup>AD/AD</sup>
Figure S.1 KCC2 <sup>+/+</sup> n = 9, KCC2 <sup>AD/AD</sup> n = 9	1	2.54 $\pm$ 0.16	1.78 $\pm$ 0.28	2.43 $\pm$ 0.19	1.76 $\pm$ 0.28	2.43 $\pm$ 0.2	1.66 $\pm$ 0.26
	2	2.09 $\pm$ 0.17	0.85 $\pm$ 0.25	2.03 $\pm$ 0.14	1.42 $\pm$ 0.21	1.87 $\pm$ 0.18	1.37 $\pm$ 0.26
	3	1.78 $\pm$ 0.15	0.73 $\pm$ 0.2	1.82 $\pm$ 0.14	1.34 $\pm$ 0.19	1.83 $\pm$ 0.19	1.26 $\pm$ 0.21
	4	1.66 $\pm$ 0.15	0.68 $\pm$ 0.19	1.72 $\pm$ 0.18	1.15 $\pm$ 0.16	1.4 $\pm$ 0.15	1.08 $\pm$ 0.19
	5	1.56 $\pm$ 0.14	0.61 $\pm$ 0.2	1.43 $\pm$ 0.17	1.11 $\pm$ 0.21	1.45 $\pm$ 0.19	0.97 $\pm$ 0.18
	6	1.47 $\pm$ 0.16	0.56 $\pm$ 0.16	1.35 $\pm$ 0.19	1.06 $\pm$ 0.21	1.24 $\pm$ 0.13	1.01 $\pm$ 0.2
	7	1.37 $\pm$ 0.14	1.05 $\pm$ 0.2	1.35 $\pm$ 0.18	0.99 $\pm$ 0.17	1.16 $\pm$ 0.14	0.86 $\pm$ 0.17
	8	1.29 $\pm$ 0.13	0.55 $\pm$ 0.19	1.18 $\pm$ 0.18	0.9 $\pm$ 0.18	1.12 $\pm$ 0.15	0.76 $\pm$ 0.2
	9	1.33 $\pm$ 0.15	0.43 $\pm$ 0.14	1.09 $\pm$ 0.16	0.8 $\pm$ 0.16	0.92 $\pm$ 0.13	0.71 $\pm$ 0.18
	10	1.21 $\pm$ 0.11	0.44 $\pm$ 0.16	1.03 $\pm$ 0.17	0.79 $\pm$ 0.18	0.93 $\pm$ 0.15	0.75 $\pm$ 0.21
	11	1.29 $\pm$ 0.13	0.5 $\pm$ 0.16	1.09 $\pm$ 0.17	0.84 $\pm$ 0.18	0.91 $\pm$ 0.16	0.69 $\pm$ 0.18
	12	1.16 $\pm$ 0.08	0.38 $\pm$ 0.1	0.95 $\pm$ 0.12	0.88 $\pm$ 0.14	0.89 $\pm$ 0.14	0.65 $\pm$ 0.13
	13	1.22 $\pm$ 0.12	0.43 $\pm$ 0.12	1.08 $\pm$ 0.16	0.84 $\pm$ 0.21	0.81 $\pm$ 0.14	0.55 $\pm$ 0.15
	14	1.27 $\pm$ 0.13	0.43 $\pm$ 0.14	0.93 $\pm$ 0.16	0.69 $\pm$ 0.15	0.79 $\pm$ 0.13	0.61 $\pm$ 0.15
	15	1.32 $\pm$ 0.16	0.52 $\pm$ 0.16	0.83 $\pm$ 0.1	0.71 $\pm$ 0.18	0.81 $\pm$ 0.14	0.52 $\pm$ 0.11
	16	1.19 $\pm$ 0.13	0.43 $\pm$ 0.12	0.85 $\pm$ 0.15	0.72 $\pm$ 0.15	0.87 $\pm$ 0.15	0.62 $\pm$ 0.16
	17	1.15 $\pm$ 0.08	0.44 $\pm$ 0.14	0.85 $\pm$ 0.14	0.71 $\pm$ 0.12	0.71 $\pm$ 0.13	0.51 $\pm$ 0.14
	18	1.13 $\pm$ 0.09	0.39 $\pm$ 0.12	0.87 $\pm$ 0.11	0.72 $\pm$ 0.15	0.72 $\pm$ 0.08	0.57 $\pm$ 0.2
	19	1.19 $\pm$ 0.11	0.41 $\pm$ 0.11	0.89 $\pm$ 0.12	0.67 $\pm$ 0.12	0.65 $\pm$ 0.13	0.54 $\pm$ 0.15
	20	1.14 $\pm$ 0.17	0.48 $\pm$ 0.13	0.89 $\pm$ 0.12	0.66 $\pm$ 0.13	0.78 $\pm$ 0.16	0.49 $\pm$ 0.1
	21	1.13 $\pm$ 0.08	0.51 $\pm$ 0.15	0.84 $\pm$ 0.09	0.72 $\pm$ 0.19	0.63 $\pm$ 0.1	0.5 $\pm$ 0.16
	22	1.21 $\pm$ 0.07	0.5 $\pm$ 0.15	0.85 $\pm$ 0.09	0.72 $\pm$ 0.13	0.7 $\pm$ 0.15	0.49 $\pm$ 0.15
	23	1.14 $\pm$ 0.13	0.45 $\pm$ 0.13	0.81 $\pm$ 0.1	0.7 $\pm$ 0.16	0.67 $\pm$ 0.12	0.45 $\pm$ 0.1
	24	1.18 $\pm$ 0.12	0.49 $\pm$ 0.16	0.78 $\pm$ 0.09	0.63 $\pm$ 0.12	0.59 $\pm$ 0.1	0.51 $\pm$ 0.12

Supplementary information

25	1.22 ± 0.12	0.43 ± 0.12	0.77 ± 0.09	0.7 ± 0.15	0.5 ± 0.09	0.45 ± 0.14
26	1.17 ± 0.13	0.45 ± 0.13	0.9 ± 0.1	0.82 ± 0.19	0.68 ± 0.15	0.52 ± 0.16
27	1.16 ± 0.12	0.46 ± 0.12	0.87 ± 0.11	0.77 ± 0.16	0.65 ± 0.12	0.45 ± 0.14
28	1.14 ± 0.12	0.4 ± 0.11	0.74 ± 0.08	0.68 ± 0.16	0.66 ± 0.11	0.42 ± 0.12
29	1.19 ± 0.12	0.44 ± 0.16	0.9 ± 0.16	0.65 ± 0.16	0.57 ± 0.09	0.47 ± 0.11
30	1.16 ± 0.09	0.41 ± 0.13	0.89 ± 0.12	0.72 ± 0.15	0.66 ± 0.13	0.45 ± 0.11
31	1.04 ± 0.09	0.45 ± 0.15	0.75 ± 0.09	0.75 ± 0.18	0.54 ± 0.1	0.35 ± 0.12
32	1.2 ± 0.13	0.44 ± 0.16	0.78 ± 0.08	0.63 ± 0.13	0.65 ± 0.16	0.48 ± 0.11
33	1.11 ± 0.13	0.52 ± 0.17	0.82 ± 0.12	0.76 ± 0.11	0.69 ± 0.14	0.42 ± 0.15
34	1.18 ± 0.11	0.41 ± 0.12	0.89 ± 0.14	0.64 ± 0.14	0.6 ± 0.11	0.46 ± 0.11
35	1.19 ± 0.14	0.43 ± 0.14	0.8 ± 0.13	0.82 ± 0.19	0.69 ± 0.12	0.44 ± 0.1
36	1.17 ± 0.11	0.42 ± 0.14	0.87 ± 0.13	0.59 ± 0.11	0.65 ± 0.11	0.35 ± 0.16
37	1.16 ± 0.11	0.44 ± 0.14	0.84 ± 0.12	0.71 ± 0.16	0.59 ± 0.14	0.4 ± 0.11
38	1.23 ± 0.11	0.49 ± 0.14	0.91 ± 0.16	0.66 ± 0.14	0.57 ± 0.11	0.39 ± 0.1
39	1.1 ± 0.12	0.49 ± 0.17	0.82 ± 0.13	0.61 ± 0.14	0.56 ± 0.11	0.31 ± 0.09
40	1.09 ± 0.11	0.46 ± 0.17	0.88 ± 0.13	0.69 ± 0.17	0.54 ± 0.15	0.38 ± 0.14
41	1.11 ± 0.07	0.41 ± 0.13	0.8 ± 0.12	0.67 ± 0.13	0.59 ± 0.13	0.38 ± 0.11
42	1.18 ± 0.12	0.48 ± 0.15	0.77 ± 0.1	0.65 ± 0.18	0.58 ± 0.15	0.37 ± 0.11
43	1.12 ± 0.1	0.45 ± 0.14	0.82 ± 0.15	0.68 ± 0.18	0.56 ± 0.14	0.35 ± 0.08
44	1.2 ± 0.13	0.45 ± 0.13	0.77 ± 0.13	0.63 ± 0.16	0.5 ± 0.11	0.36 ± 0.13
45	1.21 ± 0.08	0.4 ± 0.11	0.92 ± 0.17	0.6 ± 0.15	0.59 ± 0.13	0.38 ± 0.08
46	1.15 ± 0.12	0.47 ± 0.14	0.81 ± 0.13	0.7 ± 0.15	0.61 ± 0.14	0.31 ± 0.1
47	1.08 ± 0.13	0.44 ± 0.13	0.88 ± 0.18	0.61 ± 0.16	0.55 ± 0.15	0.27 ± 0.07
48	1.11 ± 0.14	0.44 ± 0.14	0.73 ± 0.12	0.68 ± 0.12	0.59 ± 0.12	0.5 ± 0.13
49	1.29 ± 0.11	0.45 ± 0.17	0.77 ± 0.12	0.59 ± 0.15	0.52 ± 0.11	0.33 ± 0.11
50	1.06 ± 0.1	0.46 ± 0.15	0.76 ± 0.1	0.56 ± 0.1	0.56 ± 0.13	0.38 ± 0.1

Data are presented as mean ± SEM.

**Table S.6 Reversal potential of LSO neurons.**

	LSO	Age	Mean $\pm$ SEM		P Values	post-hoc comparison	
	eIPSC		KCC2 <sup>+/+</sup>	KCC2 <sup>AD/AD</sup>			
Figure 3.10	E <sub>Cl</sub> <sup>-</sup>	P14	-36.53 $\pm$ 1.68	-42.69 $\pm$ 1.6	p = 0.001	p = 0.15	P14 vs P20: KCC2 <sup>+/+</sup> p = 0.29 KCC2 <sup>AD/AD</sup> <b>p = 0.04</b>
		P20	-30.55 $\pm$ 1.6	-34.62 $\pm$ 2.93		p = 0.75	

Data are presented as mean  $\pm$  SEM. P-values were calculated using 2-way ANOVA with Tukey's multiple comparison post-hoc tests. Significant P-values are marked in yellow. P14: KCC2<sup>+/+</sup> n = 11, KCC2<sup>AD/AD</sup> n = 14; P20: KCC2<sup>+/+</sup> n = 16, KCC2<sup>AD/AD</sup> n = 10.

**Table S.7 I<sub>glycine</sub> percentage of LSO neurons.**

	LSO	Age	Mean $\pm$ SEM		P Values	post-hoc comparison	
	eIPSC		KCC2 <sup>+/+</sup>	KCC2 <sup>AD/AD</sup>			
Figure 3.11	I <sub>glycine</sub> percent age (%)	P14	97.1 $\pm$ 0.95	97.66 $\pm$ 1.19	p = 0.62	p = 0.98	P14 vs P20: KCC2 <sup>+/+</sup> p = 0.98 KCC2 <sup>AD/AD</sup> p = 0.65
		P20	97.68 $\pm$ 1.21	95.82 $\pm$ 1.47		p = 0.65	

Data are presented as mean  $\pm$  SEM. P-values were calculated using 2-way ANOVA with Tukey's multiple comparison post-hoc tests. P14: KCC2<sup>+/+</sup> n = 6, KCC2<sup>AD/AD</sup> n = 6; P20: KCC2<sup>+/+</sup> n = 6, KCC2<sup>AD/AD</sup> n = 6.

**Table S.8 I<sub>glycine</sub> amplitude of LSO neurons.**

	LSO	Age	Mean $\pm$ SEM		P Values	post-hoc comparison	
	I <sub>glycine</sub>		KCC2 <sup>+/+</sup>	KCC2 <sup>AD/AD</sup>			
Figure 3.11	amplitude (nA)	P14	8.78 $\pm$ 0.82	5.23 $\pm$ 0.36	p < 0.001	<b>p &lt; 0.001</b>	P14 vs P20: KCC2 <sup>+/+</sup> p = 0.06 KCC2 <sup>AD/AD</sup> <b>p = 0.007</b>
		P20	10.81 $\pm$ 0.38	7.95 $\pm$ 0.5		0.001	

Data are presented as mean  $\pm$  SEM. P-values were calculated using 2-way ANOVA with Tukey's multiple comparison post-hoc tests. Significant P-values are marked in yellow. P14: KCC2<sup>+/+</sup> n = 17, KCC2<sup>AD/AD</sup> n = 17; P20: KCC2<sup>+/+</sup> n = 12, KCC2<sup>AD/AD</sup> n = 16.

**Table S.9 Normalized gephyrin puncta of LSO neurons.**

	LSO IHC	Age	Mean $\pm$ SEM		P Values	post-hoc comparison	
			KCC2 <sup>+/+</sup>	KCC2 <sup>AD/AD</sup>			
Figure 3.12	gephyrin puncta (puncta per $\mu\text{m}^2$ )	P14	0.24 $\pm$ 0.01	0.19 $\pm$ 0.01	p < 0.001	p < 0.001	P14 vs P20: KCC2 <sup>+/+</sup> p = 0.42 KCC2 <sup>AD/AD</sup> p = 0.69
		P20	0.23 $\pm$ 0.01	0.21 $\pm$ 0.01		p = 0.19	

Data are presented as mean  $\pm$  SEM. P-values were calculated using 2-way ANOVA with Tukey's multiple comparison post-hoc tests. Significant P-values are marked in yellow. P14: KCC2<sup>+/+</sup> n = 19, KCC2<sup>AD/AD</sup> n = 25; P20: KCC2<sup>+/+</sup> n = 37, KCC2<sup>AD/AD</sup> n = 40.

**Table S.10 The intrinsic membrane properties of LOC neurons.**

	LOC AP properties	Age	Mean $\pm$ SEM		P values	post-hoc comparison		
			KCC2 <sup>+/+</sup>	KCC2 <sup>AD/AD</sup>				
Figure 3.13	R <sub>in</sub> (M $\Omega$ )	P14	629.08 $\pm$ 23.87	492.63 $\pm$ 18.91	p = 0.04	p = 0.14	P14 vs P20: KCC2 <sup>+/+</sup> p = 0.99 KCC2 <sup>AD/AD</sup> p = 0.03	
		P20	651.6 $\pm$ 68.65	677.73 $\pm$ 60.71		p = 0.93		
	latency stim onset-AP peak (ms)	P14	155.21 $\pm$ 8.24	147.49 $\pm$ 10.78	p = 0.67	p = 0.64	P14 vs P20: KCC2 <sup>+/+</sup> p = 0.96 KCC2 <sup>AD/AD</sup> p = 0.98	
		P20	156.75 $\pm$ 11.63	151.03 $\pm$ 7.78		p = 0.99		
	tau (ms)	P14	8.04 $\pm$ 0.82	5.83 $\pm$ 0.7	p = 0.2	p = 0.38	P14 vs P20: KCC2 <sup>+/+</sup> p = 0.93 KCC2 <sup>AD/AD</sup> p = 0.17	
		P20	7.27 $\pm$ 0.78	8.71 $\pm$ 0.98		p = 0.68		
	rheobase (pA)	P14	33.72 $\pm$ 1.54	47.69 $\pm$ 9.04	p = 0.03	p = 0.32	P14 vs P20: KCC2 <sup>+/+</sup> p = 0.96 KCC2 <sup>AD/AD</sup> p = 0.02	
		P20	29.17 $\pm$ 4.51	22.67 $\pm$ 2.79		p = 0.81		
	Figure 3.14	AP threshold (mV)	P14	-44.71 $\pm$ 1.6	-48.22 $\pm$ 1.64	p = 0.48	p = 0.54	P14 vs P20: KCC2 <sup>+/+</sup> p = 0.52 KCC2 <sup>AD/AD</sup> p = 0.91
			P20	-48.31 $\pm$ 1.61	-46.93 $\pm$ 1.55		p = 0.89	
		AP amplitude	P14	72.7 $\pm$ 3.68	77.75 $\pm$ 4.63	p = 0.54	p > 0.99	P14 vs P20: KCC2 <sup>+/+</sup> p = 0.88 KCC2 <sup>AD/AD</sup> p = 0.63
			P20	73.61 $\pm$ 2.89	71.36 $\pm$ 2.9		p = 0.97	

Supplementary information

threshold-peak (mV)							
AP amplitude baseline-peak (mV)	P14	104.98 ± 3.78	108.57 ± 4.35	p = 0.23	p = 0.99	P14 vs P20: KCC2 <sup>+/+</sup> p = 0.75 KCC2 <sup>AD/AD</sup> p = 0.40	
	P20	104.99 ± 3.44	100.03 ± 3.95				
half width (ms)	P14	0.84 ± 0.05	0.88 ± 0.03	p = 0.03	p = 0.08	P14 vs P20: KCC2 <sup>+/+</sup> p = 0.07 KCC2 <sup>AD/AD</sup> p > 0.99	
	P20	0.88 ± 0.03	0.89 ± 0.03				
max AP rising slope (mV/ms)	P14	323.69 ± 31.09	375.82 ± 43.06	p = 0.04	p > 0.99	P14 vs P20: KCC2 <sup>+/+</sup> p = 0.50 KCC2 <sup>AD/AD</sup> p = 0.07	
	P20	299.19 ± 22.64	253.6 ± 23.17				
max AP decaying slope (mV/ms)	P14	-92.91 ± 7.23	-89.11 ± 5.63	p = 0.05	p = 0.23	P14 vs P20: KCC2 <sup>+/+</sup> p = 0.08 KCC2 <sup>AD/AD</sup> p = 0.96	
	P20	-84.71 ± 3.66	-85.19 ± 4.78				
AHP amplitude (mV)	P14	-15.46 ± 1.1	-15.82 ± 1.13	p = 0.56	p > 0.99	P14 vs P20: KCC2 <sup>+/+</sup> p = 0.69 KCC2 <sup>AD/AD</sup> p = 0.81	
	P20	-14.23 ± 1.43	-13.76 ± 1.15				

Data are presented as mean ± SEM. P-values were calculated using 2-way ANOVA with Tukey's multiple comparison post-hoc tests. P14: KCC2<sup>+/+</sup> n = 13, KCC2<sup>AD/AD</sup> n = 9; P20: KCC2<sup>+/+</sup> n = 9, KCC2<sup>AD/AD</sup> n = 10.

**Table S.11 mIPSC parameters of LOC neurons.**

	LOC mIPSC	Age	Mean ± SEM		P values	post-hoc comparison	
			KCC2 <sup>+/+</sup>	KCC2 <sup>AD/AD</sup>			
Figure 3.15, 3.16, 3.17	amplitude (pA)	P14	45.13 ± 2.77	46.81 ± 5.27	p = 0.05	p > 0.99	P14 vs P20: KCC2 <sup>+/+</sup> p = 0.18 KCC2 <sup>AD/AD</sup> p = 0.15
		P20	58.71 ± 3.32	60.7 ± 7.23		p = 0.99	
	tau rise (ms)	P14	0.71 ± 0.03	0.55 ± 0.02	p < 0.001	p = 0.004	P14 vs P20: KCC2 <sup>+/+</sup> p < 0.001 KCC2 <sup>AD/AD</sup> p = 0.003
		P20	0.39 ± 0.03	0.35 ± 0.03		p = 0.83	

Supplementary information

	tau decay (ms)	P14	5.89 ± 0.39	5.05 ± 0.26	p <	p = 0.06	P14 vs P20: KCC2 <sup>+/+</sup> p < 0.001 KCC2 <sup>AD/AD</sup> p = 0.22
		P20	3.81 ± 0.17	3.96 ± 0.15	0.001	p > 0.99	
	frequency (Hz)	P14	2.05 ± 0.27	0.72 ± 0.05	p < 0.001	p < 0.001	P14 vs P20: KCC2 <sup>+/+</sup> p = 0.07 KCC2 <sup>AD/AD</sup> p = 0.98
		P20	1.51 ± 0.11	0.7 ± 0.1		p = 0.03	

Data are presented as mean ± SEM. P-values were calculated using 2-way ANOVA with Tukey's multiple comparison post-hoc tests. Significant P-values are marked in yellow. P14: KCC2<sup>+/+</sup> n = 11, KCC2<sup>AD/AD</sup> n = 6; P20: KCC2<sup>+/+</sup> n = 9, KCC2<sup>AD/AD</sup> n = 7.

**Table S.12 eIPSC parameters of LOC neurons.**

	LOC eIPSC	Age	Mean ± SEM		P Values	post-hoc comparison	
			KCC2 <sup>+/+</sup>	KCC2 <sup>AD/AD</sup>			
Figure 3.18	amplitude (nA)	P14	0.28 ± 0.05	0.32 ± 0.05	p = 0.46	p = 0.83	P14 vs P20: KCC2 <sup>+/+</sup> p > 0.99 KCC2 <sup>AD/AD</sup> p = 0.39
		P20	0.21 ± 0.03	0.23 ± 0.04		p = 0.96	
	tau rise (ms)	P14	0.76 ± 0.1	0.48 ± 0.05	p = 0.002	p = 0.03	P14 vs P20: KCC2 <sup>+/+</sup> p = 0.04 KCC2 <sup>AD/AD</sup> p = 0.81
		P20	0.5 ± 0.03	0.39 ± 0.03		p = 0.92	
	tau decay (ms)	P14	9.35 ± 0.87	8.46 ± 0.67	p = 0.01	p = 0.82	P14 vs P20: KCC2 <sup>+/+</sup> p = 0.22 KCC2 <sup>AD/AD</sup> p = 0.09
		P20	7.15 ± 0.52	5.94 ± 0.44		p = 0.77	

Data are presented as mean ± SEM. P-values were calculated using 2-way ANOVA with Tukey's multiple comparison post-hoc tests. Significant P-values are marked in yellow. P14: KCC2<sup>+/+</sup> n = 11, KCC2<sup>AD/AD</sup> n = 10; P20: KCC2<sup>+/+</sup> n = 7, KCC2<sup>AD/AD</sup> n = 11.

**Table S.13 eIPSC amplitude of LOC neurons (P14) at 10Hz, 50Hz and 100Hz stimulating frequencies.**

	Pulse	LOC eIPSCs amplitude Mean ± SEM (nA)		
		P14 (10Hz)	P14 (50Hz)	P14 (100Hz)

Supplementary information

		KCC2 <sup>+/+</sup>	KCC2 <sup>AD/AD</sup>	KCC2 <sup>+/+</sup>	KCC2 <sup>AD/AD</sup>	KCC2 <sup>+/+</sup>	KCC2 <sup>AD/AD</sup>
Figure 3.19 KCC2 <sup>+/+</sup> n = 6, KCC2 <sup>AD/AD</sup> n = 7	1	0.26 ± 0.07	0.38 ± 0.05	0.25 ± 0.08	0.37 ± 0.06	0.31 ± 0.09	0.35 ± 0.06
	2	0.18 ± 0.05	0.36 ± 0.04	0.23 ± 0.06	0.29 ± 0.03	0.21 ± 0.05	0.26 ± 0.03
	3	0.19 ± 0.05	0.25 ± 0.03	0.16 ± 0.02	0.22 ± 0.03	0.21 ± 0.06	0.22 ± 0.04
	4	0.18 ± 0.05	0.23 ± 0.04	0.19 ± 0.05	0.23 ± 0.03	0.16 ± 0.04	0.23 ± 0.03
	5	0.21 ± 0.05	0.24 ± 0.03	0.17 ± 0.04	0.23 ± 0.05	0.07 ± 0.01	0.21 ± 0.04
	6	0.16 ± 0.04	0.23 ± 0.03	0.15 ± 0.03	0.22 ± 0.03	0.15 ± 0.05	0.19 ± 0.03
	7	0.13 ± 0.04	0.19 ± 0.02	0.17 ± 0.04	0.22 ± 0.04	0.1 ± 0.02	0.19 ± 0.05
	8	0.16 ± 0.05	0.19 ± 0.03	0.13 ± 0.04	0.19 ± 0.04	0.09 ± 0.02	0.18 ± 0.03
	9	0.14 ± 0.05	0.17 ± 0.04	0.07 ± 0.03	0.2 ± 0.03	0.09 ± 0.02	0.16 ± 0.03
	10	0.14 ± 0.02	0.17 ± 0.03	0.15 ± 0.05	0.2 ± 0.04	0.1 ± 0.05	0.15 ± 0.03
	11	0.12 ± 0.02	0.16 ± 0.03	0.13 ± 0.02	0.17 ± 0.03	0.16 ± 0.05	0.11 ± 0.02
	12	0.11 ± 0.03	0.19 ± 0.03	0.11 ± 0.02	0.18 ± 0.04	0.08 ± 0.02	0.15 ± 0.03
	13	0.13 ± 0.04	0.19 ± 0.03	0.09 ± 0.02	0.15 ± 0.03	0.08 ± 0.02	0.11 ± 0.02
	14	0.15 ± 0.04	0.15 ± 0.03	0.12 ± 0.03	0.12 ± 0.03	0.13 ± 0.04	0.13 ± 0.01
	15	0.15 ± 0.03	0.19 ± 0.03	0.1 ± 0.02	0.18 ± 0.02	0.06 ± 0.02	0.16 ± 0.03
	16	0.13 ± 0.03	0.21 ± 0.04	0.16 ± 0.05	0.16 ± 0.04	0.06 ± 0.01	0.12 ± 0.02
	17	0.13 ± 0.04	0.16 ± 0.02	0.07 ± 0.02	0.16 ± 0.03	0.07 ± 0.02	0.12 ± 0.03
	18	0.12 ± 0.03	0.17 ± 0.03	0.09 ± 0.02	0.15 ± 0.04	0.11 ± 0.03	0.12 ± 0.03
	19	0.16 ± 0.04	0.18 ± 0.03	0.09 ± 0.03	0.12 ± 0.02	0.07 ± 0.01	0.12 ± 0.03
	20	0.12 ± 0.02	0.15 ± 0.03	0.11 ± 0.03	0.12 ± 0.02	0.07 ± 0.01	0.11 ± 0.03
	21	0.15 ± 0.02	0.14 ± 0.02	0.09 ± 0.02	0.12 ± 0.03	0.09 ± 0.04	0.11 ± 0.03
	22	0.13 ± 0.03	0.15 ± 0.03	0.09 ± 0.02	0.12 ± 0.04	0.07 ± 0.01	0.14 ± 0.02
	23	0.13 ± 0.05	0.16 ± 0.02	0.06 ± 0.01	0.12 ± 0.02	0.1 ± 0.02	0.11 ± 0.03
	24	0.13 ± 0.03	0.13 ± 0.02	0.17 ± 0.08	0.11 ± 0.03	0.06 ± 0.01	0.11 ± 0.02
	25	0.12 ± 0.03	0.17 ± 0.02	0.05 ± 0.01	0.14 ± 0.03	0.07 ± 0.01	0.11 ± 0.03
	26	0.12 ± 0.02	0.18 ± 0.04	0.12 ± 0.03	0.14 ± 0.04	0.13 ± 0.07	0.1 ± 0.03
	27	0.08 ± 0.03	0.16 ± 0.03	0.08 ± 0.02	0.13 ± 0.03	0.03 ± 0.01	0.1 ± 0.02
	28	0.12 ± 0.04	0.17 ± 0.04	0.09 ± 0.02	0.1 ± 0.03	0.08 ± 0.02	0.1 ± 0.03
	29	0.13 ± 0.03	0.13 ± 0.03	0.06 ± 0.01	0.11 ± 0.03	0.06 ± 0.01	0.11 ± 0.04
	30	0.14 ± 0.04	0.16 ± 0.02	0.11 ± 0.02	0.14 ± 0.04	0.05 ± 0.01	0.09 ± 0.03
	31	0.09 ± 0.02	0.14 ± 0.03	0.1 ± 0.03	0.14 ± 0.05	0.05 ± 0.01	0.08 ± 0.04

Supplementary information

32	0.1 ± 0.02	0.19 ± 0.03	0.09 ± 0.03	0.13 ± 0.04	0.04 ± 0.01	0.11 ± 0.04
33	0.11 ± 0.03	0.15 ± 0.03	0.13 ± 0.04	0.13 ± 0.03	0.04 ± 0.02	0.12 ± 0.03
34	0.13 ± 0.04	0.15 ± 0.04	0.07 ± 0.02	0.12 ± 0.03	0.04 ± 0.01	0.09 ± 0.03
35	0.12 ± 0.03	0.15 ± 0.03	0.09 ± 0.03	0.1 ± 0.03	0.08 ± 0.03	0.09 ± 0.03
36	0.14 ± 0.03	0.16 ± 0.03	0.09 ± 0.02	0.11 ± 0.04	0.07 ± 0.02	0.11 ± 0.05
37	0.15 ± 0.05	0.17 ± 0.04	0.09 ± 0.02	0.12 ± 0.04	0.08 ± 0.02	0.1 ± 0.04
38	0.09 ± 0.01	0.15 ± 0.05	0.09 ± 0.03	0.1 ± 0.04	0.03 ± 0.01	0.09 ± 0.03
39	0.12 ± 0.02	0.18 ± 0.04	0.09 ± 0.01	0.1 ± 0.04	0.08 ± 0.03	0.09 ± 0.03
40	0.11 ± 0.03	0.12 ± 0.03	0.09 ± 0.01	0.11 ± 0.04	0.05 ± 0.01	0.08 ± 0.02
41	0.13 ± 0.04	0.14 ± 0.04	0.07 ± 0.01	0.11 ± 0.03	0.05 ± 0.01	0.1 ± 0.03
42	0.12 ± 0.03	0.13 ± 0.02	0.06 ± 0.02	0.08 ± 0.03	0.04 ± 0.01	0.08 ± 0.03
43	0.11 ± 0.03	0.19 ± 0.03	0.08 ± 0.01	0.12 ± 0.04	0.06 ± 0.02	0.1 ± 0.02
44	0.1 ± 0.03	0.14 ± 0.02	0.07 ± 0.01	0.1 ± 0.03	0.05 ± 0.01	0.09 ± 0.03
45	0.08 ± 0.01	0.16 ± 0.03	0.06 ± 0.01	0.1 ± 0.03	0.04 ± 0.01	0.08 ± 0.03
46	0.09 ± 0.03	0.17 ± 0.04	0.12 ± 0.05	0.09 ± 0.03	0.03 ± 0.01	0.09 ± 0.04
47	0.07 ± 0.02	0.14 ± 0.04	0.09 ± 0.02	0.09 ± 0.03	0.07 ± 0.02	0.05 ± 0.02
48	0.14 ± 0.02	0.18 ± 0.04	0.07 ± 0.01	0.09 ± 0.03	0.08 ± 0.04	0.09 ± 0.03
49	0.11 ± 0.03	0.16 ± 0.03	0.11 ± 0.04	0.09 ± 0.03	0.1 ± 0.06	0.09 ± 0.03
50	0.12 ± 0.02	0.12 ± 0.02	0.07 ± 0.01	0.08 ± 0.03	0.04 ± 0.01	0.08 ± 0.03

Data are presented as mean ± SEM.

**Table S.14 eIPSC amplitude of LOC neurons (P20) at 10Hz, 50Hz and 100Hz stimulating frequencies.**

	Pulse	LOC eIPSCs amplitude Mean $\pm$ SEM (nA)					
		P20 (10Hz)		P20 (50Hz)		P20 (100Hz)	
		KCC2 <sup>+/+</sup>	KCC2 <sup>AD/AD</sup>	KCC2 <sup>+/+</sup>	KCC2 <sup>AD/AD</sup>	KCC2 <sup>+/+</sup>	KCC2 <sup>AD/AD</sup>
Figure S.2 KCC2 <sup>+/+</sup> n = 5, KCC2 <sup>AD/AD</sup> n = 5	1	0.2 $\pm$ 0.04	0.26 $\pm$ 0.13	0.17 $\pm$ 0.03	0.13 $\pm$ 0.06	0.17 $\pm$ 0.03	0.23 $\pm$ 0.14
	2	0.12 $\pm$ 0.02	0.22 $\pm$ 0.06	0.18 $\pm$ 0.02	0.2 $\pm$ 0.1	0.15 $\pm$ 0.02	0.14 $\pm$ 0.03
	3	0.14 $\pm$ 0.03	0.27 $\pm$ 0.1	0.13 $\pm$ 0.01	0.14 $\pm$ 0.03	0.11 $\pm$ 0.01	0.11 $\pm$ 0.04
	4	0.17 $\pm$ 0.02	0.2 $\pm$ 0.05	0.13 $\pm$ 0.01	0.14 $\pm$ 0.05	0.13 $\pm$ 0.02	0.12 $\pm$ 0.01
	5	0.11 $\pm$ 0.02	0.15 $\pm$ 0.03	0.08 $\pm$ 0.01	0.09 $\pm$ 0.02	0.08 $\pm$ 0.02	0.14 $\pm$ 0.04
	6	0.12 $\pm$ 0.03	0.14 $\pm$ 0.03	0.12 $\pm$ 0.01	0.14 $\pm$ 0.06	0.1 $\pm$ 0.01	0.1 $\pm$ 0.02
	7	0.11 $\pm$ 0.02	0.13 $\pm$ 0.03	0.1 $\pm$ 0.02	0.11 $\pm$ 0.03	0.07 $\pm$ 0.02	0.11 $\pm$ 0.05
	8	0.1 $\pm$ 0.02	0.17 $\pm$ 0.06	0.09 $\pm$ 0.01	0.05 $\pm$ 0.01	0.08 $\pm$ 0.02	0.11 $\pm$ 0.05
	9	0.09 $\pm$ 0.02	0.12 $\pm$ 0.03	0.11 $\pm$ 0.01	0.13 $\pm$ 0.06	0.08 $\pm$ 0.01	0.12 $\pm$ 0.02
	10	0.08 $\pm$ 0.02	0.14 $\pm$ 0.06	0.09 $\pm$ 0.01	0.1 $\pm$ 0.02	0.07 $\pm$ 0.02	0.11 $\pm$ 0.04
	11	0.09 $\pm$ 0.02	0.14 $\pm$ 0.03	0.09 $\pm$ 0.01	0.1 $\pm$ 0.04	0.09 $\pm$ 0.01	0.1 $\pm$ 0.01
	12	0.09 $\pm$ 0.02	0.07 $\pm$ 0.02	0.08 $\pm$ 0.02	0.05 $\pm$ 0.01	0.09 $\pm$ 0.03	0.09 $\pm$ 0.03
	13	0.08 $\pm$ 0.01	0.06 $\pm$ 0.02	0.1 $\pm$ 0.02	0.05 $\pm$ 0.01	0.09 $\pm$ 0.02	0.1 $\pm$ 0.04
	14	0.1 $\pm$ 0.03	0.06 $\pm$ 0.04	0.1 $\pm$ 0.01	0.07 $\pm$ 0.02	0.08 $\pm$ 0.02	0.1 $\pm$ 0.02
	15	0.07 $\pm$ 0.01	0.11 $\pm$ 0.04	0.1 $\pm$ 0.02	0.09 $\pm$ 0.02	0.09 $\pm$ 0.02	0.09 $\pm$ 0.01
	16	0.09 $\pm$ 0.02	0.11 $\pm$ 0.06	0.13 $\pm$ 0.03	0.09 $\pm$ 0.04	0.08 $\pm$ 0.02	0.08 $\pm$ 0.01
	17	0.1 $\pm$ 0.01	0.08 $\pm$ 0.02	0.08 $\pm$ 0.02	0.06 $\pm$ 0.01	0.08 $\pm$ 0.02	0.15 $\pm$ 0.05
	18	0.09 $\pm$ 0.02	0.08 $\pm$ 0.02	0.11 $\pm$ 0.01	0.07 $\pm$ 0.02	0.08 $\pm$ 0.02	0.08 $\pm$ 0.01
	19	0.1 $\pm$ 0.04	0.09 $\pm$ 0.03	0.11 $\pm$ 0.02	0.1 $\pm$ 0.04	0.07 $\pm$ 0.02	0.08 $\pm$ 0.02
	20	0.07 $\pm$ 0.02	0.08 $\pm$ 0.03	0.08 $\pm$ 0.02	0.09 $\pm$ 0.04	0.08 $\pm$ 0.02	0.1 $\pm$ 0.03
	21	0.07 $\pm$ 0.02	0.05 $\pm$ 0.01	0.07 $\pm$ 0.02	0.08 $\pm$ 0.04	0.07 $\pm$ 0.02	0.08 $\pm$ 0.01
	22	0.08 $\pm$ 0.02	0.06 $\pm$ 0.02	0.09 $\pm$ 0.02	0.07 $\pm$ 0.01	0.08 $\pm$ 0.03	0.1 $\pm$ 0.02
	23	0.06 $\pm$ 0.02	0.1 $\pm$ 0.05	0.08 $\pm$ 0.02	0.08 $\pm$ 0.01	0.08 $\pm$ 0.03	0.08 $\pm$ 0.03
	24	0.08 $\pm$ 0.01	0.05 $\pm$ 0.02	0.1 $\pm$ 0.04	0.08 $\pm$ 0.03	0.07 $\pm$ 0.02	0.09 $\pm$ 0.03
	25	0.09 $\pm$ 0.02	0.05 $\pm$ 0.01	0.08 $\pm$ 0.02	0.09 $\pm$ 0.02	0.07 $\pm$ 0.02	0.11 $\pm$ 0.02
	26	0.08 $\pm$ 0.02	0.05 $\pm$ 0.02	0.09 $\pm$ 0.03	0.06 $\pm$ 0.01	0.07 $\pm$ 0.02	0.15 $\pm$ 0.06

Supplementary information

27	0.08 ± 0.01	0.06 ± 0.01	0.07 ± 0.02	0.09 ± 0.04	0.08 ± 0.03	0.13 ± 0.04
28	0.07 ± 0.02	0.03 ± 0.01	0.08 ± 0.02	0.11 ± 0.05	0.07 ± 0.02	0.12 ± 0.06
29	0.08 ± 0.02	0.05 ± 0.01	0.08 ± 0.03	0.11 ± 0.05	0.07 ± 0.02	0.16 ± 0.07
30	0.08 ± 0.02	0.06 ± 0.02	0.08 ± 0.02	0.07 ± 0.04	0.07 ± 0.02	0.12 ± 0.05
31	0.08 ± 0.02	0.04 ± 0.01	0.07 ± 0.02	0.08 ± 0.02	0.05 ± 0.01	0.14 ± 0.04
32	0.09 ± 0.02	0.05 ± 0.02	0.07 ± 0.02	0.07 ± 0.03	0.06 ± 0.02	0.12 ± 0.06
33	0.08 ± 0.03	0.05 ± 0.01	0.09 ± 0.02	0.05 ± 0.02	0.09 ± 0.02	0.11 ± 0.06
34	0.06 ± 0.02	0.06 ± 0.02	0.05 ± 0.01	0.06 ± 0.02	0.06 ± 0.02	0.13 ± 0.05
35	0.05 ± 0.01	0.03 ± 0.01	0.09 ± 0.03	0.06 ± 0.02	0.05 ± 0.02	0.09 ± 0.04
36	0.07 ± 0.02	0.04 ± 0.01	0.09 ± 0.02	0.05 ± 0.02	0.05 ± 0.01	0.09 ± 0.03
37	0.07 ± 0.02	0.04 ± 0.01	0.07 ± 0.02	0.1 ± 0.04	0.08 ± 0.03	0.13 ± 0.06
38	0.06 ± 0.01	0.04 ± 0.01	0.09 ± 0.02	0.11 ± 0.03	0.06 ± 0.02	0.14 ± 0.04
39	0.1 ± 0.02	0.15 ± 0.1	0.08 ± 0.02	0.07 ± 0.02	0.07 ± 0.03	0.12 ± 0.05
40	0.09 ± 0.02	0.02 ± 0.02	0.09 ± 0.02	0.18 ± 0.09	0.04 ± 0.02	0.09 ± 0.03
41	0.07 ± 0.02	0.04 ± 0.01	0.1 ± 0.04	0.1 ± 0.04	0.06 ± 0.02	0.11 ± 0.04
42	0.08 ± 0.01	0.05 ± 0.01	0.06 ± 0.02	0.06 ± 0.03	0.07 ± 0.02	0.09 ± 0.04
43	0.08 ± 0.02	0.03 ± 0.01	0.06 ± 0.01	0.15 ± 0.07	0.09 ± 0.03	0.15 ± 0.04
44	0.05 ± 0.01	0.04 ± 0.01	0.1 ± 0.03	0.12 ± 0.05	0.07 ± 0.02	0.13 ± 0.07
45	0.08 ± 0.02	0.06 ± 0.01	0.05 ± 0.01	0.11 ± 0.04	0.05 ± 0.01	0.1 ± 0.05
46	0.07 ± 0.02	0.03 ± 0.01	0.07 ± 0.02	0.09 ± 0.05	0.07 ± 0.02	0.17 ± 0.08
47	0.11 ± 0.02	0.05 ± 0.02	0.06 ± 0.02	0.12 ± 0.05	0.05 ± 0.02	0.13 ± 0.05
48	0.08 ± 0.03	0.02 ± 0.01	0.09 ± 0.02	0.11 ± 0.03	0.06 ± 0.02	0.09 ± 0.03
49	0.09 ± 0.02	0.04 ± 0.01	0.08 ± 0.03	0.09 ± 0.05	0.05 ± 0.02	0.1 ± 0.04
50	0.08 ± 0.02	0.03 ± 0.02	0.09 ± 0.02	0.12 ± 0.05	0.08 ± 0.02	0.08 ± 0.03

Data are presented as mean ± SEM.

## 8 Index of figures and tables

Figure 1.1 Developmental shift in KCC2 and NKCC1 transport activities changes GABAergic/glycinergic signaling from depolarizing to hyperpolarizing. ....	5
Figure 1.2 Synaptic organization of LSO and LOC circuits.....	8
Figure 1.3 Shift from depolarizing to hyperpolarizing actions of GABA and glycine in the auditory brainstem of mammals.....	10
Figure 1.4 Enhanced KCC2 transport activity in $KCC2^{AD/AD}$ mice. ....	13
Figure 1.5 Curtailed depolarizing phase in $KCC2^{AD/AD}$ mice.....	14
Figure 3.1 Differentiation of LSO and LOC neurons according to morphology and intrinsic membrane properties.....	21
Figure 3.2 Differentiation LSO and LOC neurons based on IPSC kinetics.....	22
Figure 3.3 Curtailed depolarizing phase does not impact intrinsic membrane properties of LSO neurons. ....	25
Figure 3.4 Normal maturation of active neuronal properties despite the curtailed depolarizing phase. ....	27
Figure 3.5 Spontaneous release at the MNTB-LSO synapse is unaffected by curtailed depolarizing phase. ....	29
Figure 3.6 mIPSC in LSO neurons show no developmental increase in amplitude in $KCC2^{AD/AD}$ mice. ....	30
Figure 3.7 Curtailed depolarizing phase does not affect the kinetics of mIPSC in LSO neurons. ....	31
Figure 3.8 Curtailed depolarizing phase reduces the eIPSC amplitudes in LSO neurons.....	33
Figure 3.9 Normal short-term plasticity in LSO neurons of $KCC2^{AD/AD}$ mice at P14. ....	34
Figure 3.10 No major differences in $E_{IPSC}$ across genotypes. ....	35
Figure 3.11 GlyR-mediated currents are reduced in LSO neurons of $KCC2^{AD/AD}$ mice. ....	37
Figure 3.12 Postsynaptic gephyrin abundance is reduced in $KCC2^{AD/AD}$ mice of P14 LSO neurons. ....	38
Figure 3.13 Intrinsic membrane properties of LOC neurons develop normally in $KCC2^{AD/AD}$ mice..	40
Figure 3.14 AP properties unchanged in LOC neurons in $KCC2^{AD/AD}$ mice.....	41
Figure 3.15 Spontaneous synaptic release is reduced in $KCC2^{AD/AD}$ mice. ....	42
Figure 3.16 mIPSC amplitude is preserved in LOC neurons of $KCC2^{AD/AD}$ mice.....	43
Figure 3.17 mIPSC kinetics in LOC neurons exhibit transient acceleration in $KCC2^{AD/AD}$ mice at P14.....	44
Figure 3.18 eIPSC are transiently accelerated in LOC neurons of $KCC2^{AD/AD}$ mice.....	46
Figure 3.19 Normal short-term plasticity in LOC neurons from $KCC2^{AD/AD}$ mice at P14. ....	46
Figure S.1 Normal short-term plasticity in LSO neurons of $KCC2^{AD/AD}$ mice at P20. ....	78
Figure S.2 Normal short-term plasticity in LOC neurons of $KCC2^{AD/AD}$ mice at P20. ....	79
Table S.1 Intrinsic membrane properties of LSO neurons. ....	79

*Index of figures and tables*

Table S.2 mIPSC parameters of LSO neurons. ....	81
Table S.3 eIPSC parameters of LSO neurons ....	81
Table S.4 eIPSC amplitude of LSO neurons (P14) at 10Hz, 100Hz and 200Hz stimulating frequencies. ....	82
Table S.5 eIPSC amplitude of LSO neurons (P20) at 10Hz, 100Hz and 200Hz stimulating frequencies. ....	84
Table S.6 Reversal potential of LSO neurons. ....	86
Table S.7 $I_{\text{glycine}}$ percentage of LSO neurons. ....	86
Table S.8 $I_{\text{glycine}}$ amplitude of LSO neurons. ....	86
Table S.9 Normalized gephyrin puncta of LSO neurons. ....	87
Table S.10 The intrinsic membrane properties of LOC neurons. ....	87
Table S.11 mIPSC parameters of LOC neurons. ....	88
Table S.12 eIPSC parameters of LOC neurons. ....	89
Table S.13 eIPSC amplitude of LOC neurons (P14) at 10Hz, 50Hz and 100Hz stimulating frequencies. ....	89
Table S.14 eIPSC amplitude of LOC neurons (P20) at 10Hz, 50Hz and 100Hz stimulating frequencies. ....	92

## **9 Acknowledgements**

I would like to express my deepest gratitude to my supervisor, Prof. Dr. Ivan Milenkovic, for his continuous support, guidance throughout my doctoral research. When I began this journey, I was new to the field of auditory neuroscience. Through his patient mentorship, I gradually developed the confidence to engage with demanding experimental work. I am particularly grateful for his thoughtful feedback during data presentations and for his constructive suggestions whenever experimental challenges arose.

I would also like to sincerely thank Dr. Tamara Radulovic for her invaluable guidance during the early stage of this project, especially in helping me learn and refine patch-clamp techniques. Although the learning process was at times challenging, these experiences are very important for my development as a researcher.

My sincere thanks also go to Dr. Christian Keine for his generous support and insightful input throughout different stages of the experiments and during many scientific discussions. His guidance was especially important during Dr. Radulovic's parental leave and greatly contributed to the progress of this work.

I am very grateful to our technicians, Jasmin Schröder, Nicole Ahrens and Jenny Sonnert, for their excellent management of animal breeding, which ensured a reliable supply for my experiments. I also thank them for their dedicated maintenance of laboratory supplies and organization, which allowed the experimental work to proceed smoothly.

Finally, I would like to express my deepest gratitude to my family for their unwavering support. To my children in particular, thank you for your love and understanding during the long period when I could not be with you. Your quiet strength accompanied me throughout this journey.

## Erklärung

Hiermit erkläre ich, dass ich die vorliegende Arbeit selbstständig verfasst habe und keine als die angegebenen Quellen und Hilfsmittel verwendet habe. Ich versichere, dass diese Arbeit weder in ihrer Gesamtheit noch in Teilen einer anderen Hochschule zur Begutachtung in einem Promotionsverfahren vorliegt oder vorgelegen hat und dass ich die Leitlinien guter wissenschaftlicher Praxis der Carl von Ossietzky Universität Oldenburg befolgt habe. Weiterhin versichere ich, dass im Zusammenhang mit dem Promotionsvorhaben keine kommerziellen Vermittlungs- oder Beratungsdienste in Anspruch genommen worden sind.